Politecnico di Milano

SCUOLA DI INGEGNERIA INDUSTRIALE E DELL'INFORMAZIONE
Corso di Laurea Magistrale in Ingegneria Matematica

Numerical Modeling of Organic Thin Film Transistors

Candidato:
Pasquale Claudio Africa
Matricola 816884

Relatore:
Carlo de Falco

Correlatore:
Dario Andrea Nicola Natali

Anno Accademico 2014–2015

If people do not believe that mathematics is simple, it is only because they do not realize how complicated life is.

J. von Neumann

Alla mia famiglia...

Ringraziamenti

Non è mai facile realizzare di aver raggiunto un importante traguardo. Fino a poco tempo fa mi sembrava così lontano, eppure proprio oggi per me è arrivato quell'inevitabile momento in cui ci si ferma a riflettere e a tentare un bilancio delle proprie esperienze. Voltandomi indietro mi rendo conto di quante cose sono cambiate in questi cinque anni, ma ancor di più mi rendo conto che non sarei mai potuto arrivare fin qui senza l'imprescindibile appoggio di tutte quelle persone che mi sono state accanto durante questo percorso e alle quali, molto probabilmente, non sarò mai in grado di dimostrare abbastanza gratitudine.

Innanzitutto il mio *grazie* più sincero va al relatore della mia tesi Carlo de Falco e al correlatore Dario Natali, per non avermi mai abbandonato e per avermi sempre spinto a tirare fuori il meglio di me, guidandomi con immensa pazienza attraverso mille difficoltà: senza il loro supporto, questo lavoro non avrebbe mai potuto prendere forma. Ringrazio inoltre Davide Cagnoni per tutte le chiacchierate e le interminabili sessioni di debugging!

Un immenso *grazie* va innegabilmente alla mia famiglia, che non ha mai smesso di sostenermi e incoraggiarmi e per avermi fatto diventare quello che sono.

Infine *grazie* a tutti i compagni di viaggio e agli amici di una vita che hanno reso unica e speciale questa avventura, in particolare a Vittorio, Luca, Alessandra, Francesco, Clara, grazie ad Alice per i suoi preziosi consigli sulla stesura di questa tesi, a tutti i coinquilini, ai professori e ai ragazzi dell'AIM, con i quali ho condiviso esperienze indimenticabili dentro e fuori da quel posto magico chiamato Tender!
Grazie.

Milano, 30 Settembre 2015 P. A.

Abstract

The discovery of electrical conduction properties of a class of organic materials [HMS00] (Nobel Prize in Chemistry, 2000) represents a potential breakthrough opening the way to a plethora of highly innovative products benefiting from the peculiar properties of organic semiconductors, such as the ability of being produced ad a low cost and deposited on flexible substrates, and bio-compatibility. In particular in this thesis we focus on mathematical models and numerical methods for the simulation of Organic Thin Film Transistors (OTFTs), which are Field-Effect Transistors (FETs) made by depositing thin films of a semiconductor layer over a non-conducting substrate (such as glass) and are being adopted in the development of products such as flexible displays and integrated circuits, sensors, organic memories and e-paper.

Charge transport in organic semiconductors occurs via a sequence of thermally activated *hopping* events between strongly localized energetic sites. Although such a mechanism is inherently different with respect to principles of charge transport in inorganic materials, the mathematical models to describe the former are based on the same Drift-Diffusion (DD) equations used for the latter; the peculiar characteristics of conduction in organic semiconductors are represented via specific models for the equation coefficients and in particular for the mobility. The state of the art is the Extended Gaussian Disorder Model (EGDM), which allows to factor the mobility as a constant, representing the low-applied-field and low-charge-density mobility, times a set of enhancement factors expressing the effects of electric field and charge density on the mobility. The enhancement factors strongly depend on the parameter σ which represents the degree of energetic disorder of the system. Such parameter can not be directly measured but it is usually left as a *fitting parameter* when modeling current transport.

In [Mad+15] the authors presented a method to extract the value of σ from quasi-static capacitance-voltage ($C-V$) measurements. Here we present some significant modifications to this procedure consisting of an improved optimization algorithm for assessing σ from $C-V$ measurements and an unsteady simulation model which allows to capture the effects of the charge injection barrier at metallic contacts on capacitance measurements.

Keywords: organic semiconductors; density of states; capacitance-voltage measurements; current-voltage measurements; metal-insulator-semiconductor; organic thin film transistors; unsteady simulations.

Sommario

La scoperta di proprietà conduttive in una classe di materiali organici [HMS00] (Premio Nobel per la Chimica, 2000) rappresenta un importante passo verso lo sviluppo di prodotti altamente innovativi che godono delle particolari proprietà dei semiconduttori organici, come ad esempio la possibilità di produrli a basso costo e di depositarli su sottostrati flessibili e la bio-compatibilità. In particolare in questa tesi si farà riferimento ai modelli matematici e ai metodi numerici per la simulazione di Organic Thin Film Transistor (OTFT), cioè Field-Effect Transistor (FET) costruiti depositando pellicole sottili di uno strato semiconduttore su un sottostrato isolante (come il vetro), il cui impiego rientra nello sviluppo di prodotti come display e circuiti integrati flessibili, sensori, memorie organiche e carta elettronica.

Il trasporto di carica nei semiconduttori organici avviene mediante una sequenza di eventi di *hopping*, attivati all'aumentare della temperatura, tra siti energetici fortemente localizzati. Nonostante questo meccanismo sia intrinsecamente differente dai principi del trasporto di carica nei materiali inorganici, i modelli matematici che descrivono entrambi i sistemi sono basati sullo stesso sistema Drift-Diffusion (DD); le particolari caratteristiche della conduzione nei semiconduttori organici sono rappresentate attraverso una specifica modellazione dei coefficienti di queste equazioni e in particolare della mobilità. Lo stato dell'arte è il modello Extended Gaussian Disorder Model (EGDM), che prevede di fattorizzare la mobilità come una costante, che rappresenta la mobilità a bassi campi applicati e a basse densità di carica, moltiplicata per dei fattori di enhancement, espressione degli effetti esercitati dal campo elettrico e dalla densità di carica sulla mobilità. I fattori di enhancement dipendono fortemente dal parametro σ, che rappresenta il grado di disordine energetico del sistema. Questo parametro non può essere direttamente misurato ma, di solito, ricopre il ruolo di parametro di fitting nella modellazione del trasporto di corrente.

In [Mad+15] gli autori hanno presentato un metodo per estrarre il valore di σ a partire da misurazioni quasi-statiche di capacità-tensione ($C-V$). In questo lavoro presentiamo alcune rilevanti modifiche a questa procedura che consistono in una versione migliorata dell'algoritmo di ottimizzazione per valutare σ dalle curve $C-V$ e in un modello di simulazione in condizioni non stazionarie che consente di catturare

gli effetti della barriera di iniezione di carica ai contatti metallici sulle misure di capacità.

Parole chiave: semiconduttori organici; densità degli stati; misure di capacità-tensione; misure di corrente-tensione; metallo-isolante-semiconduttore; transistori organici a film sottile; simulazioni non stazionarie.

Contenuto

Il presente lavoro è diviso in quattro parti principali.

Parte I (Introduzione) Nel capitolo 1 verranno dettagliate le motivazioni alla base dello studio dei dispositivi basati su semiconduttori organici, presentandone le principali proprietà e descrivendo alcuni importanti e recenti esempi di applicazione nel campo delle nuove tecnologie. Il capitolo 2 è invece dedicato alla particolare classe di dispositivi che si vuole studiare, i transistori organici a film sottile (OTFT); verrà illustrato il principio del loro funzionamento, cercando di far emergere l'importanza che i transistori rivestono ancora oggi nel mercato dell'elettronica, anche nella loro più moderna variante basata sui semiconduttori organici.

Parte II (Modelli matematico-fisici) Il capitolo 3 riguarderà la descrizione dei fenomeni di trasporto di carica all'interno dei dispositivi a semiconduttore. Verranno messe in luce le differenze che intercorrono tra i dispositivi a base organica e quelli, ben più studiati, a base inorganica spiegando come la diversità dei meccanismi in gioco nei due casi abbia poi delle importanti ricadute nei modelli matematici che li descrivono. Questi modelli, di natura discreta o continua, saranno poi introdotti nel capitolo 4 a partire da naturali principi fisici di base (come leggi di conservazione, ad esempio). Ci si concentrerà in particolare sul modello DD, un sistema di equazioni alle derivate parziali avente come incognite il potenziale elettrico e le densità di portatori di carica. La principale differenza del sistema DD tra il caso organico e inorganico consiste nella diversa modellizzazione delle mobilità dei portatori, cioè di quei coefficienti che descrivono la risposta delle cariche sotto l'effetto di un campo elettrico. L'elevato livello di disordine molecolare nei materiali organici, a differenza della struttura perfettamente cristallina dei semiconduttori come ad esempio il silicio, si riflette nei coefficienti di mobilità mediante delle espressioni funzionali fortemente non-lineari e dipendenti da parametri che non possono essere misurati sperimentalmente, come la mobilità a bassi campi e a basse concentrazioni μ_0 e il parametro di disordine molecolare σ. Il modello più largamente utilizzato in letteratura è l'EGDM, oggetto di studio del capitolo 5. Nel capitolo 6 i modelli descritti saranno chiusi da delle opportune condizioni al contorno, espressione dei meccanismi fisici coinvolti in corrispondenza dei contatti elettrici. Infine, nel capitolo 7, si spiegherà come la natura degli effetti capacitivi del dispositivo in esame siano legati al parametro di disordine σ e come sarà possibile sfruttare questa informazione per estrarre σ a partire da misure sperimentali di capacità-tensione.

Parte III (Metodi numerici) Interesse di questa parte è lo studio dei metodi numerici utilizzati per la simulazione degli OTFT. Nel capitolo 8 si delineerà un generico algoritmo di fitting per estrarre il parametro di disordine σ a partire dal confronto delle curve capacità-tensione simulate (in condizioni stazionarie) con quelle sperimentali, mentre il capitolo 9 si occuperà dei metodi per ricavare la mobilità a bassi campi e a basse concentrazioni μ_0 fittando le caratteristiche corrente-tensione simulate (in condizioni stazionarie) con i dati sperimentali a disposizione. Il contributo più originale di questo lavoro risiede nel capitolo 10, dove si darà la descrizione di un algoritmo numerico per la simulazione di dispositivi a semiconduttore organico in condizioni non stazionarie sotto il controllo di un circuito esterno; in particolare verrà data una formulazione del problema in termini di un metodo di Newton e in termini di un metodo di punto-fisso alla Gummel, opportunamente generalizzati per tener conto della natura evolutiva del problema, dei modelli fisici coinvolti (come ad esempio le relazioni costitutive tra densità di cariche e potenziale elettrico) e delle forti non-linearità introdotte dal modello EGDM.

Parte IV (Risultati numerici) Nei capitoli 11, 12 e 13 verranno infine illustrati e commentati i risultati ottenuti, rispettivamente, dalle simulazioni numeriche eseguite mediante le tecniche descritte nella precedente parte.

Table of contents

List of figures

List of algorithms and tables

List of acronyms

FET Field-Effect Transistor

OTFT Organic Thin Film Transistor

MIS Metal-Insulator-Semiconductor

RFID Radio-Frequency Identification

OLED Organic Light-Emitting Diode

DNA Deoxyribonucleic Acid

OPV Organic Photovoltaics

HOMO Highest Occupied Molecular Orbital

LUMO Lowest Unoccupied Molecular Orbital

DD Drift-Diffusion

DOS Density of States

EGDM Extended Gaussian Disorder Model

ECDM Extended Correlated Disorder Model

MNA Modified Nodal Analysis

P(NDI2OD-T2) Poly{[N,N'-bis(2-octyldodecyl)-naphthalene-1,4,5,8-bis(dicarboximide)-2,6-diyl]-alt-5,5'-(2,2'-bithiophene)}

PMMA Poly(methyl methacrylate)

Introduction Part I

1 Organic-based semiconductor devices

Several factors have motivated a continuous research in organic semiconductor technologies, such as easy and low cost fabrication of large area circuits, mechanical flexibility, high transparency and bio-compatibility. The molecular nature of organic materials allows sub-micron structures to be created at a low cost using soft-lithography, self-assembly or printing techniques instead of expensive conventional optical lithography used for inorganic (usually silicon-based) ones [BS+14]. Moreover, organic sensors and transistors can be produced without the need of heavy hazardous metals or other harmful materials, thus guaranteeing bio-compatibility and the possibility to implant them within biological surfaces such as human tissues and skin. Ultimately, since they do not require high temperature processing, sensible substrates such as plastic or textiles can be exploited for the fabrication.

However, when drawing comparisons between plastic and silicon circuitry one must be aware that the two systems are deeply different and their behavior and performances do not necessarily match. A major drawback of organic devices is a lower charge carrier mobility, i.e. the ability of charged particles to move in response to an electric field, due to weak intermolecular interactions in the solid state (despite recent improvements, as shown in fig. 1.1). Therefore, organic materials should not be expected to replace silicon as the favored basis for electronic circuits, but to enable research for new and emerging applications.

An important trend is that key industry sectors are starting to implement a variety of products based on organic and printed electronics. In particular, a strong engagement and product introduction is seen in the automotive, consumer electronics, packaging and medical/pharmaceutical sectors.

New possibilities of this kind of technology can be grouped into five clusters [OEA]:

1. lighting (Organic Light-Emitting Diodes (OLEDs));
2. light-harvesting (photovoltaics);
3. flexible displays;

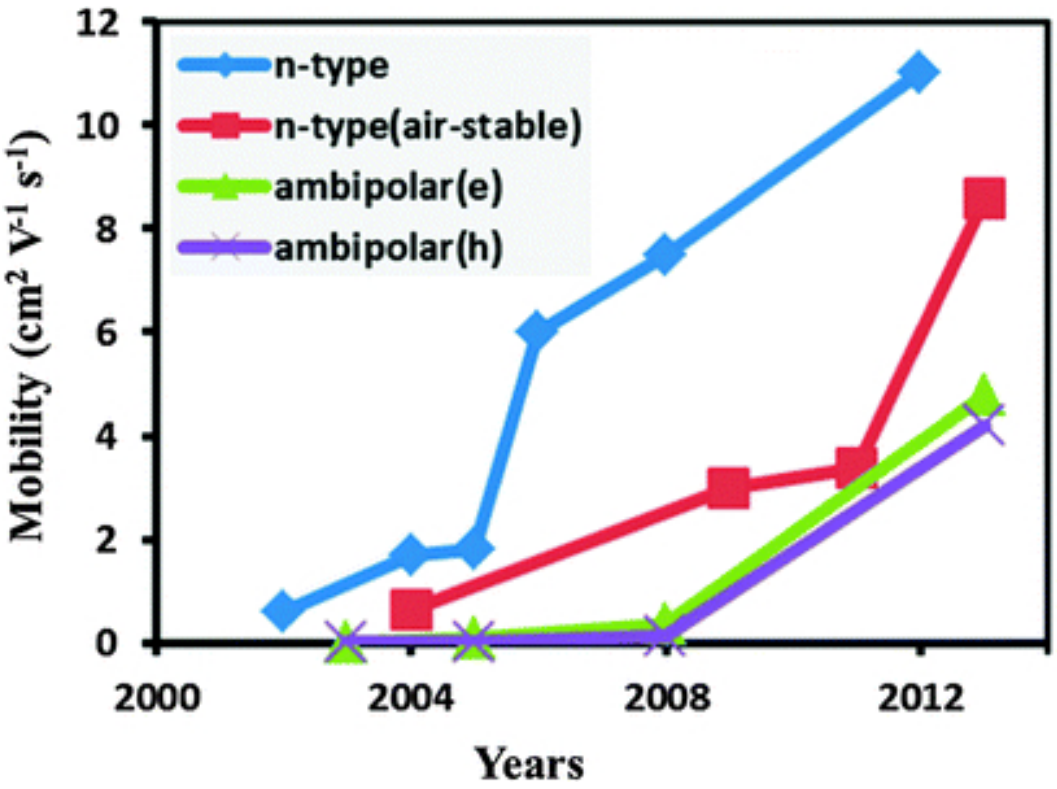

Figure 1.1: Mobility trend for a class of organic semiconductors. Source: [Zho+14].

4. electronics and components (memories, batteries, ...);

5. integrated smart systems (smart objects, sensors and smart textiles).

1.1 Lighting

OLED-based **lighting** is seen as the most promising approach for future lighting due to superior efficiency, flexibility, and high durability. Besides, devices like white emitting OLEDs for general lighting, monochrome OLED lamps for automotive or signage applications, are growing in importance. The market is expected to grow steadily, especially if some key challenges, such as continued lowering of production costs, are met.

1.2 Photovoltaics

Organic Photovoltaics (OPV) is an recent energy technology. OPV devices typically consist on a semi-transparent substrate and a photo-absorbing organic layer. They can be made on flexible substrates, thus enabling power sources to be suitable for

many emerging applications, such as wearables and mobile devices. The production of this kind of devices grants a much shorter payback time than inorganic technology, although their efficiency and lifetime are still under improvement.

1.3 Flexible displays

Flexible displays are an extension of flat panel displays that successfully replaced cathode-ray tubes for use in computers and televisions and made the existence of laptops, tablets, e-readers, smartphones possible. Flexible organic-based displays can dispense with some key issues of current flat ones, such as the presence of breakable and heavy glass and the inability to be bent or used with different form factors. The market is starting to demonstrate a variety of flexible displays, from mobile phone to watches, and it is growing to lead into wider availability of flexible consumer electronics.

1.4 Electronics and components

Electronics and components include, for example, printed memories and flexible batteries.
Printed memories are needed for applications where the user is required to store information (companies use printed memory labels for brand protection against counterfeiters), while **flexible batteries** are of central importance in solving the issue of power supply in gaming as well as in mobile and wellness devices, besides being employed in *smart packaging* applications.
Active (such as transistors, diodes, logic circuits and display elements) and **passive** (resistors, capacitors, inductors, tubes) **components** can also be printed.
An area that was recently interested by intense research activity is that of **transparent conductive films**, to be used in optical devices, photovoltaics, electromagnetic shielding and for touch sensors in mobile devices.

1.5 Integrated smart systems

Smart objects bring multiple functionalities to perform complex tasks without the need for external hardware; integrated smart systems are being used in the development of sensors and smart textiles.
Sensors allow to detect informations from the surroundings. Organic-based force sensors, for example, have found use as part of touch screen displays in consumer devices, but also in health care and automotive applications. More specifically, photodetectors

are gaining importance in the market of logistics, environmental monitoring, and medical imaging.

Smart textiles are able to alter their properties in response to external stimuli; these functionalities are being embedded, for example, into clothing. Organic and printed electronics opens new possibilities in health monitoring with enhanced comfort for the wearer; the ability to process and transmit data makes *wearable electronics* a reality.

2 OTFTs

Organic electronics is moving ahead on its journey towards reality: the continuous progress made in the field of organic semiconductors has achieved important goals such as relatively high charge carrier mobility, thus offering ample opportunities for organic-based printed integrated circuits [MN15].

Field-Effect Transistors (FETs) are nowadays the basis for all electronic circuits and processors. The ability to create transistors from organic materials raises exciting possibilities for low cost electronics. In particular OTFTs, which are FETs made by depositing thin films of a semiconductor layer over a non-conducting substrate (such as glass), are being adopted in the development of products such as backplanes of flexible displays and circuits for sensor applications.

Research on organic FETs over the past 25 years has contributed greatly to the scientific understanding of the fundamental charge transport physics of conjugated polymer and small-molecule organic semiconductors [Sir14]. These materials provide unique realizations of systems where transport is intermediate between conventional low-mobility transport in amorphous glasses and high-mobility transport in crystalline materials.

2.1 Mechanism of operation

A FET is a *three-terminal* component where the current flow between the *source* and the *drain* is controlled by the voltage applied to the *gate* terminal (see fig. 2.1) [BS+14]. It can be used as a single component to amplify a current or combined with other transistors into an integrated circuit.

The metallic gate, the insulator layer and the bulk semiconductor act in effect as a capacitor, with the gate forming one plate, the insulator acting as a dielectric spacer, and the semiconductor forming the other plate: this is called a Metal-Insulator-Semiconductor (MIS) capacitor. Therefore, when applying a bias across the plates, opposite and equal charges will accumulate at the insulator-semiconductor interface.

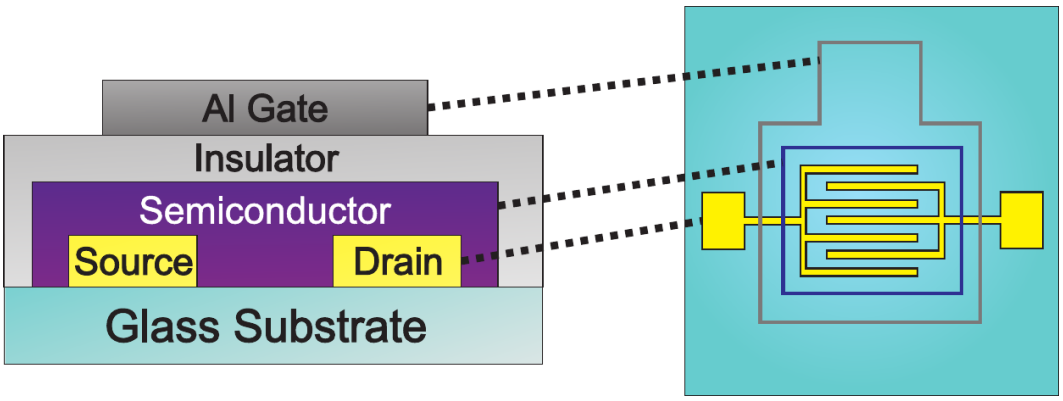

Figure 2.1: Schematic of a thin film transistor (side view and top view). Source: [Mad+15].

This capacitive effect determines the charge density in the channel (the region between the source and drain electrodes where the charge carriers flow); when applying a higher bias than a threshold gate voltage V_T the conductivity becomes substantial and the device turns on. Then the motion of charge carriers from source to drain through the semiconductor layer takes place on applying a suitable drain-to-source potential V_{DS} [KKN14].

2.2 Applications and perspectives

OTFTs are extremely useful in applications such as flexible integrated circuits, sensors, organic memories, e-paper and Radio-Frequency Identification (RFID) tags; moreover, they have turned out to be promising backplane drivers in OLED-based flexible displays (see figs. 2.2 and 2.3) [KKN14]. Recent advancements in organic material fabrication techniques direct the researchers to make use of flexible substrates, such as paper, plastic, glass and fiber, for low cost and light weight flexible applications.

OTFTs find also extensive applications in organic inverters and ring oscillators. Few recent examples of use are described in the following subsections [KKN14].

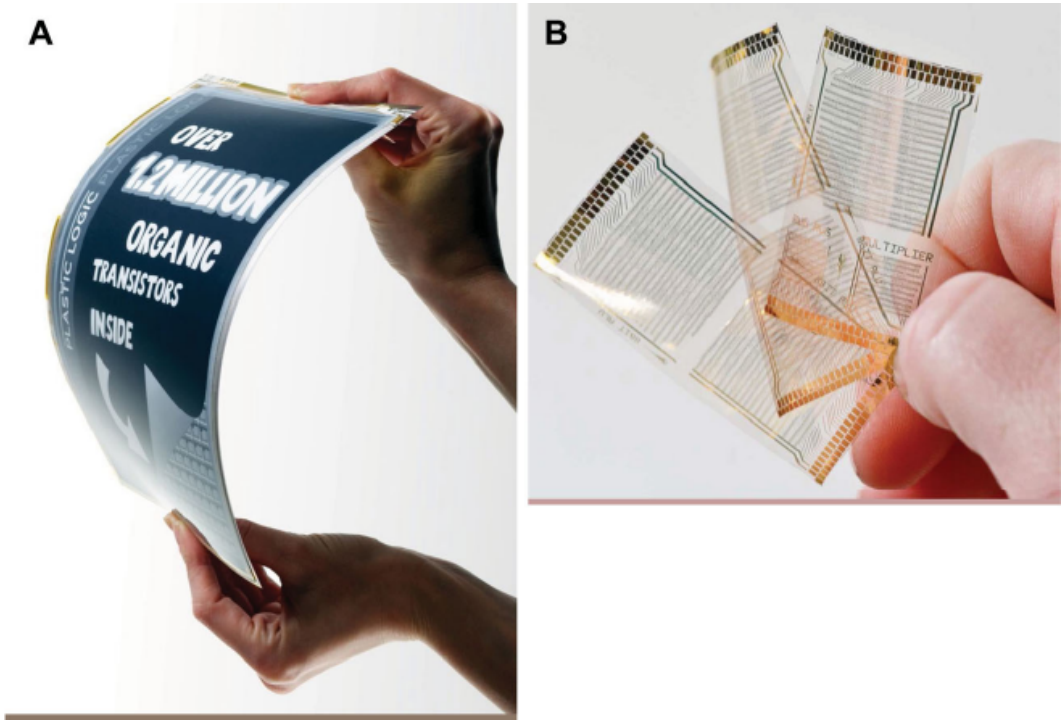

Figure 2.2: Photographs of A) flexible electrophoretic displays; B) plastic-printed microprocessors. Source: [Sir14].

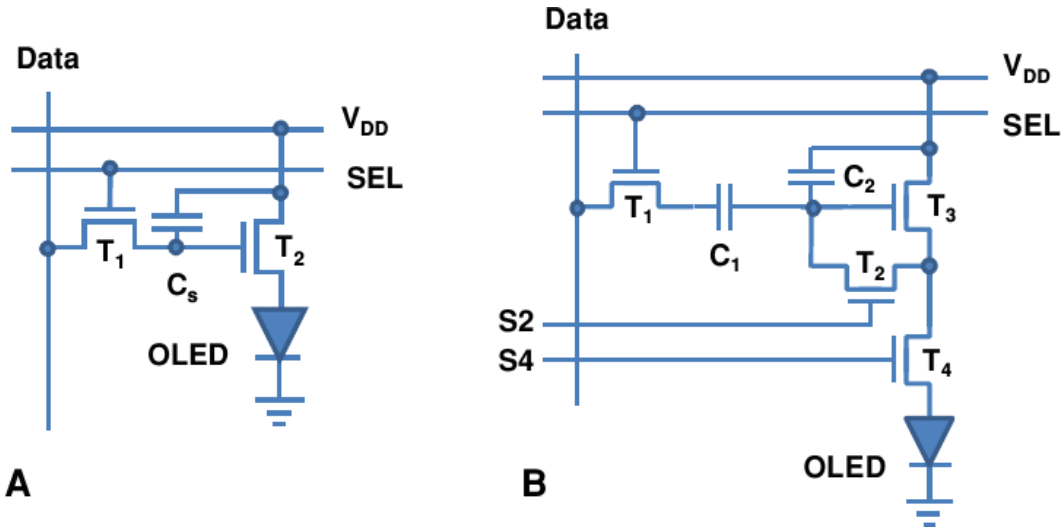

Figure 2.3: Pixel circuits for active matrix OLEDs. The letter *T* denotes OTFTs. Source: [Sir14].

RFID tags

A potentially emerging area for OTFTs is Radio-Frequency Identification of an object. Organic RFIDs are useful in different kind of applications, such as electronic product coding/labeling, supply chain management, medical science, toll bridges and identification of inventory in retail shops. Developments in low temperature fabrication techniques for organic materials encourage to make use of them in RFID tags instead of their silicon-based counterparts which are almost three orders more expensive.

Organic DNA sensors

OTFTs are promising for application in flexible Deoxyribonucleic Acid (DNA) sensors due to their quick response time. This can enable the deployment of DNA micro-array techniques for disposable diagnosis toolkits. These sensors are often used to detect and quantify the nucleic acids for forensic analysis and pharmacogenomic research, by transforming a chemical binding event into electrical signals that can be easily measured and analyzed.

Physical and mathematical models Part II

3 Charge transport in organic semiconductors

As anticipated in the introduction, while physical mechanisms governing charge transport in organic semiconductors are inherently different from those in well known crystalline inorganic materials such as, e.g., silicon, the mathematical models used to simulate such phenomena are strongly connected. For this reason, it is common practice to introduce the physical bases of charge transport in inorganic semiconductors (section 3.1) in order to mark the differences with respect to organic ones (section 3.2).

3.1 Inorganic semiconductors

Atoms in ordered inorganic semiconductors (such as silicon) are kept together by covalent bonds which originate a perfectly regular, crystalline solid. Typically inorganic semiconductors are built from elements in group IV of the periodic table (Si, Ge, ...), possibly compounded with elements belonging to group III or V (GeAs, InAs, InP, ...). In such systems electronic states are clearly defined and give rise to an *energy-band structure*: charge carriers are confined to a number of bands of energy (*valence band* and *conduction band*, separate by an *energy gap*) and forbidden from others (see fig. 3.1).

Therefore a *band transport* is allowed: charge carriers are said to be *delocalized* as they are spread across more than one atom and hence free to move in the whole crystal. Occasionally their motion is hampered by *scattering* phenomena due to imperfections in the crystalline structure such as dopants or *phonons* (due to a vibrational motion of the lattice). In a wave-only view, carriers are plane waves propagating in a periodic potential generated by atomic nuclei and charges occupying inner energetic levels in the periodic lattice.

Because of the band transport described above, a crystalline semiconductor can be approximated as a charged rarefied gas, where particles are free to move; hence

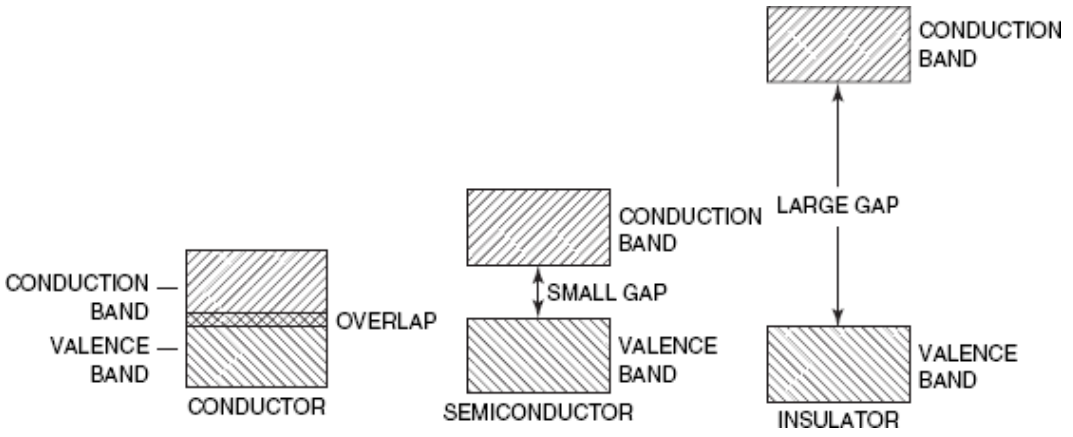

Figure 3.1: Valence and conduction bands in different materials. Source: [Hec11].

typical transport models can be deduced from the Boltzmann's transport equation:

$$\frac{\partial f}{\partial t} + \frac{\mathrm{d}\mathbf{x}}{\mathrm{d}t} \cdot \nabla_{\mathbf{x}} f + \frac{\mathrm{d}\mathbf{p}}{\mathrm{d}t} \cdot \nabla_{\mathbf{p}} f = 0,$$

where $f = f(\mathbf{x}, \mathbf{p}, t)$ denotes the distribution function of a generic charge carrier in the seven-dimensional space of spatial coordinates ($\mathbf{x}$), momentum ($\mathbf{p}$) and time (t). The classical Drift-Diffusion (DD) model is the zero-order moment in the hierarchical expansion of the Boltzmann's equation [Jer96; MR90].

Ultimately, in inorganic semiconductors charge carrier densities significantly vary by introducing dopant impurities (see section 3.3), i.e. atoms having one valence electron more or less than the host element, into the lattice.

3.2 Organic semiconductors: energetic disorder

Unlike inorganic materials, organic semiconductors are molecular solids, where molecules are kept together by *van der Waals' interactions* which act between permanent and induced dipoles and are relatively weak compared to covalent bonds. As a result, organic semiconductors have (up to 80%) lower relative dielectric permittivity, thus Coulomb interactions between charges are stronger.
Weak intermolecular interactions and common production techniques of organic semiconductor materials often lead to high levels of topological and energetic disorder [CB12]; these systems can be distinguished into the *amorphous* and *semi-crystalline* categories [Kax03]:

- in **amorphous solids** there is no long-range order of any type, even though the local arrangement of atoms has a certain degree of regularity;

- **quasi-crystals** show certain symmetries such as rotations, reflections or an underlying regular pattern, but they are not compatible with a three-dimensional periodicity; these crystalline regions attain dimensions of the order of [nm] ÷ [μm].

Each molecule is characterized by the Highest Occupied Molecular Orbital (HOMO) and Lowest Unoccupied Molecular Orbital (LUMO) (called the *frontier orbitals*): current conduction occurs when excited charges jump from a frontier orbital (which is the LUMO for electrons and HOMO for holes) to the same frontier orbital of an adjacent molecule.

In contrast to ordered crystalline semiconductors (with well-defined energy structures consisting of bands and gaps), the energy spectrum of a disordered material can be treated as quasi-continuum [Wei+06]. Instead of bands and gaps one can distinguish between extended and localized states[1] (see fig. 3.2), where, according to the definition given in [And78] by Anderson (Nobel Prize in Physics, 1977), a charge carrier wave function is respectively spread over the whole volume or localized to a restricted region. Localized sites can be interpreted as segments of a conjugated polymer chain and are responsible for the flow of charge, as charge carriers spend most of their time localized in a precise energetic state on a molecule.

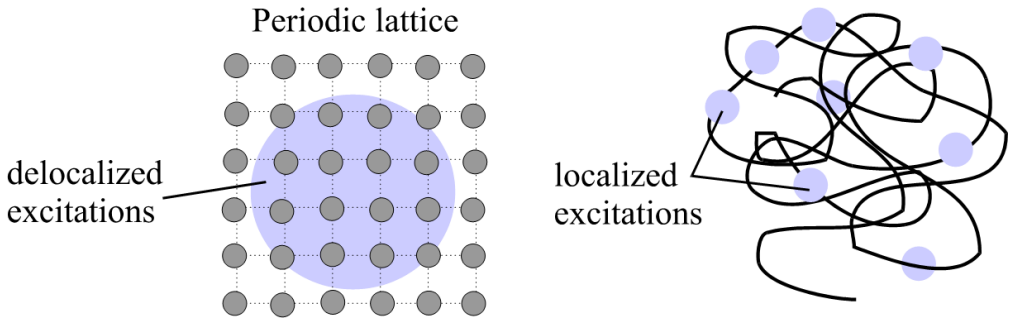

Figure 3.2: Localization and delocalization of energetic states. Source: photonicswiki.

Charge transport occurs by means of a *hopping mechanism* (see fig. 3.3), which is a phonon-assisted and thermally activated quantum tunneling effect (where a particle tunnels through an energetic barrier that could not be *classically* overcome) from one site to another neighboring site. This is why in organic materials hopping events are promoted by high temperatures (which allow for higher molecular vibration amplitude), while in inorganic semiconductors the mobility decreases with temperature.

[1] In the mathematical formulation, a "state" is a vector in an Hilbert space over a complex field; in an appropriate basis it is represented as a *wave function* [Gri05], which contains all the information about the quantum state of an entire system of particles.

Usually, the conductivity ς is found to be thermally activated as:

$$\varsigma(T) = \varsigma_0 \exp\left(-\frac{E_{act}}{k_B T}\right),$$

where ς_0 is the (theoretical) maximum conductivity $\left[\mho \mathrm{m}^{-1}\right]$, k_B the Boltzmann's constant $\left[\mathrm{J} \cdot \mathrm{K}^{-1}\right]$, T the temperature [K] and E_{act} the activation energy [J].

Many hopping models are based on the solution of a *Master equation* [Wei+06], which consists of a discrete balance of hopping probabilities from each site to neighboring ones and will be described in more details in section 4.1.

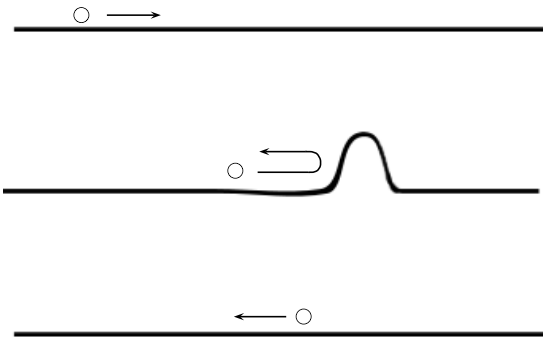

(a) Band transport. In a crystal (the straight line) charge carriers are delocalized. Lattice vibrations disrupt the symmetry, thus limiting the carriers mobility.

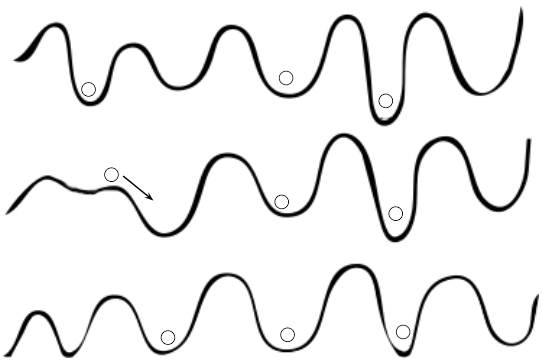

(b) Hopping transport. Carriers are localized due to defects or disorder, so the lattice vibrations are essential for a carrier to move from one site to another.

Figure 3.3: Charge transport in inorganic and organic semiconductors. Source: [PS99].

3.3 Doping

Doping, i.e. introducing charged impurities into a pure (intrinsic) lattice, led to the breakthrough of conventional semiconductor technologies; it granted the possibility to control the charge carriers flow, giving rise to the design of $p-n$ junctions, the *building blocks* of most electronic devices. Furthermore, doping enhances performances by adjusting the conductivity and the position of the Fermi level.

Organic semiconductors can be doped by adding electron acceptors or donors, although doping techniques are still under study. Because of the weak van der Waals' interactions between molecules, organic materials are less sensitive to impurities and structural defects than crystalline semiconductors but, because of stronger Coulomb interactions between charges, dopant concentrations have to be considerably higher for organic materials, thus affecting the molecular assembly, the morphology, and the electronic properties of the film (mobility, energy levels distribution, ...).

Doping can be described as a two-step process:

1. the dopant is ionized, transferring an electron (hole) to the host material and leaving a hole (electron) on the dopant; the ionization energy corresponds to the difference between the HOMO level and the vacuum energy level;

2. the electron (hole) has to dissociate against the Coulomb attraction of the hole (electron) left on the dopant.

The second step is harder to achieve in the case of organic semiconductors because of their lower relative permittivity.

Two major drawbacks of doping organic semiconductors are the instability of the dopant concentration, which is usually not constant in time, and the difficulty to control the doping level inside the device, because of a lower doping efficiency (defined as the ratio of the density of free charge carriers to the density of dopants) due to the molecular disorder. This is why these materials are often used as intrinsic and charges are preferred to be injected through metal electric contacts.

4 Mathematical models

The aim of this chapter is to deal with the mathematical models describing the physical properties of organic semiconductors. Following the qualitative description of phenomena on which charge transport in those systems is based, the *Master equation*, a discrete model whose solution allows to determine the charge-carrier mobility, and the continuum *Drift-Diffusion* system, describing the spatial-temporal evolution of the relevant physical quantities, will be introduced in sections 4.1 and 4.2 respectively. Finally, constitutive relations will be exploited in sections 4.3 and 4.4 to bring closure to the model.

4.1 Discrete models: the "Master equation"

By considering the semiconductor as a system of localized quantum states (that may or may not be occupied by charged particles), the general transport equation describing the balance of hopping events between a state i and a state j at equilibrium is the so-called *Master equation* [Mei+06]:

$$W_{ij}p_i(1-p_j) - W_{ji}p_j(1-p_i) = 0 \qquad \forall i,j, \tag{4.1}$$

where:

p_i the time-averaged probability of occupation of the state i by a charge;
W_{ij} the transition rate for hopping from site i to site j.

The penalty terms $1-p_i$ and $1-p_j$ account for the Pauli exclusion principle by prescribing that only one charge carrier can occupy a site. By assuming that hopping of carriers from site to site occur by means of a thermally assisted tunneling process, the coefficients W_{ij} can be expressed by the so-called *Miller-Abrahams model* [MA60]:

$$W_{ij} = \begin{cases} \nu_0 \exp\left[-2\varpi R_{ij} - \frac{\mathscr{E}_j - \mathscr{E}_i}{k_B T}\right], & \mathscr{E}_j \geq \mathscr{E}_i, \\ \nu_0 \exp\left[-2\varpi R_{ij}\right], & \mathscr{E}_j < \mathscr{E}_i, \end{cases} \tag{4.2}$$

where:

- k_B the Boltzmann's constant $\left[\mathrm{J}\cdot\mathrm{K}^{-1}\right]$;
- T the temperature [K];
- ν_0 an intrinsic rate (*attempt-to-escape frequency*);
- R_{ij} $=\left|\mathbf{R}_j-\mathbf{R}_i\right|$, the distance between site i and site j [m];
- ϖ the inverse localization length of the states considered $\left[\mathrm{m}^{-1}\right]$;
- $\mathscr{E}_i$ the energy of site i [J].

Equation (4.1) can be solved by drawing the on-site energies $\mathscr{E}_i$ randomly from a given distribution representing the Density of States (further details about the choice of this function will be given in section 4.4). The equilibrium distribution of charges according to eq. (4.1) is usually computed by means of a Monte Carlo method by simulating the evolution of an initial population until equilibrium is reached [SBS81; Bäs93; Bou+09a]. Once the solution has been computed, the mobility coefficient μ $\left[\mathrm{m}^2\mathrm{V}^{-1}\mathrm{s}^{-1}\right]$ related to a generic charge carrier is given by (see [Bou+09a]):

$$\mu=\frac{\frac{1}{N}\sum_{i,j}W_{ij}p_i(1-p_j)R_{ij,\mathbf{E}}}{|\mathbf{E}|}, \tag{4.3}$$

where:

- N is the total number of charge carriers: $N=nV$, V being the total volume and n denoting the mean (over V) of the occupation probabilities p_i;
- $\mathbf{E}$ is an applied electric field $\left[\mathrm{V}\cdot\mathrm{m}^{-1}\right]$;
- $R_{ij,\mathbf{E}}$ is the distance between site i and site j along the direction of $\mathbf{E}$ [m].

The numerator of eq. (4.3) can be interpreted as the velocity of the particles. Taking the limit of the master equation as the dimension of the space of energetic states becomes continuum leads to the DD model.

4.2 Continuum models: the "Drift-Diffusion" model

A continuum model can be derived by assuming the distribution of charges in the material to be a function of a continuum spatial variable. The electromagnetic fields inside the device can be modeled through the Maxwell's equations:

$$\begin{cases} \nabla\cdot\mathbf{D}=\rho, & \text{(4.4a)}\\ \nabla\times\mathbf{E}+\dfrac{\partial\mathbf{B}}{\partial t}=\mathbf{0}, & \text{(4.4b)}\\ \nabla\cdot\mathbf{B}=0, & \text{(4.4c)}\\ \nabla\times\mathbf{H}-\dfrac{\partial\mathbf{D}}{\partial t}=\mathbf{J}, & \text{(4.4d)} \end{cases}$$

where:

- $\mathbf{E}$ the electric field $\left[\mathrm{V}\cdot\mathrm{m}^{-1}\right]$;
- $\mathbf{D}$ the electric displacement field $\left[\mathrm{C}\cdot\mathrm{m}^{-2}\right]$;
- ρ the spatial charge density (per unit volume) $\left[\mathrm{C}\cdot\mathrm{m}^{-3}\right]$;
- $\mathbf{B}$ the magnetic induction field $\left[\mathrm{N}\cdot\mathrm{A}^{-1}\mathrm{m}^{-1}\right]$;
- $\mathbf{H}$ the auxiliary magnetic field $\left[\mathrm{A}\cdot\mathrm{m}^{-1}\right]$;
- $\mathbf{J}$ the electric current density (per unit area) $\left[\mathrm{A}\cdot\mathrm{m}^{-2}\right]$.

In a linear, isotropic, homogeneous medium the constitutive relation $\mathbf{D} = \varepsilon\mathbf{E}$, $\varepsilon = \varepsilon_0\varepsilon_r$ holds, ε_0 being the vacuum permittivity $\left[\mathrm{C}\cdot\mathrm{V}^{-1}\mathrm{m}^{-1}\right]$ and ε_r the material relative permittivity.

4.2.1 Poisson's equation

From (4.4c) it is possible to introduce a *vector potential*, i.e. a vector field $\mathbf{A}$ such that:

$$\nabla\times\mathbf{A} = \mathbf{B}.$$

The *gauge freedom* allows to write a vector potential in the form $\mathbf{A}+\nabla\phi$ [Jac99], where ϕ is an arbitrary function, as $\nabla\times\nabla\phi = 0\ \forall\phi$.
We assume basic regularity hypotheses for the functions considered and the domain (so that derivatives can be exchanged); hence, by inserting last equation into (4.4b):

$$\nabla\times\left(\mathbf{E}+\frac{\partial\mathbf{A}}{\partial t}\right) = \mathbf{0} \Rightarrow \mathbf{E}+\frac{\partial\mathbf{A}}{\partial t} = -\nabla\varphi$$

for an appropriate function φ called the *electrostatic potential*.
After a multiplication by ε the equation becomes:

$$\mathbf{D}+\varepsilon\frac{\partial\mathbf{A}}{\partial t} = -\varepsilon\nabla\varphi.$$

Applying the operator divergence and exchanging time and space derivatives:

$$\nabla\cdot\mathbf{D}+\varepsilon\frac{\partial}{\partial t}(\nabla\cdot\mathbf{A}) = -\nabla\cdot\left(\varepsilon\nabla\varphi\right)$$

which, inserting (4.4a), gives:

$$\varepsilon\frac{\partial}{\partial t}(\nabla\cdot\mathbf{A})+\nabla\cdot\left(\varepsilon\nabla\varphi\right) = -\rho.$$

We choose the arbitrary function ϕ so that the *Lorenz gauge condition* is satisfied:

$$\varepsilon\frac{\partial}{\partial t}(\nabla\cdot\mathbf{A}) = -\frac{1}{c^2}\frac{\partial\varphi}{\partial t},$$

c being the vacuum velocity of electromagnetic waves.
The electrostatic potential φ is then the solution to the *wave equation*:

$$\frac{1}{c^2}\frac{\partial^2\varphi}{\partial t^2} - \nabla\cdot\left(\varepsilon\nabla\varphi\right) = \rho.$$

c is usually much greater than the characteristic propagation velocities in the device considered (for example the mean velocity of a charge carrier); in other words, we are assuming that the length of the highest frequency electromagnetic wave is much greater than a characteristic length of the device (there is no substantial propagation). Therefore, the first term can be then neglected compared to the others and a *Poisson's equation* for the electrostatic potential φ is obtained [Mar86]:

$$-\nabla\cdot\left(\varepsilon\nabla\varphi\right) = \rho.$$

In the following we will assume that the device domain Ω is made of a semiconductor region Ω_{sc} and an insulator region Ω_{ins} (see segment AA in fig. 6.1) such that $\Omega_{sc}\cup\Omega_{ins} = \Omega$. Hence the following expressions hold:

$$\varepsilon = \begin{cases} \varepsilon_{sc}, & \text{in } \Omega_{sc}, \\ \varepsilon_{ins}, & \text{in } \Omega_{ins}, \end{cases}$$

and

$$\rho = \begin{cases} -q\left(n - p + N_D\right), & \text{in } \Omega_{sc}, \\ 0, & \text{in } \Omega_{ins}. \end{cases}$$

Here n and p $\left[\mathrm{m}^{-3}\right]$ are the charge carrier (electron and hole respectively) densities (per unit volume) and N_D $\left[\mathrm{m}^{-3}\right]$ is the net dopant concentration ($N_D < 0$ denotes an n-type doping and $N_D > 0$ a p-type one).
Finally, the Poisson's equation becomes:

$$\boxed{-\nabla\cdot\left(\varepsilon\nabla\varphi\right) = -q(n - p + N_D).} \tag{4.5}$$

4.2.2 Model assumptions

Hereinafter, we will assume the following hypotheses [Mad+15]:

- the semiconductor is intrinsic, i.e. the dopant concentration N_D is zero, as it is very often in organic semiconductors; hence the total charge density becomes:

$$\rho = \begin{cases} -q\left(n - p\right), & \text{in } \Omega_{sc}, \\ 0, & \text{in } \Omega_{ins}; \end{cases}$$

- thermal generation effects are negligible (energy gaps are sufficiently large);
- leakage currents are negligible in the insulator region Ω_{ins};
- the semiconductor is unipolar, i.e. the device operation is based predominantly on the use of majority charge carriers; we will consider n-type devices, i.e. $p \approx 0$ (p-type devices can be treated analogously), and will neglect generation/recombination phenomena. From these assumptions we get the simplified expression:

$$\rho = -qn. \tag{4.6}$$

Since techniques for establishing stable doping in organic semiconductors are still under study, bipolar devices have found less attention in the literature; moreover, the device architecture of FETs is simple and requires only one type of charge carrier [KB15].

Finally, since the electric potential φ is defined up to an additive constant, we choose a reference level in such a way that:

$$\varphi = -\frac{\mathscr{E}_{LUMO}}{q} \tag{4.7}$$

inside the device, where $\mathscr{E}_{LUMO}$ is the energy level associated with the molecular orbital LUMO.

4.2.3 Continuity equations

Equation (4.5) has two unknowns: φ and n. One more equation can be deduced by a basic conservation principle in order to bring closure to the system.

The conservation of the total number of particles, when generation/recombination phenomena do not occur, is expressed by the following equation:

$$\frac{\partial n}{\partial t} + \nabla \cdot \mathbf{f}_n = 0,$$

where $\mathbf{f}_n$ is the electron flux density $\left[\mathrm{m}^{-2}\mathrm{s}^{-1}\right]$. We define the total electron current density $\left[\mathrm{A}\cdot\mathrm{m}^{-2}\right]$ as:

$$\mathbf{J}_n = -q\mathbf{f}_n.$$

By linearizing the electron distribution functions around equilibrium, the following constitutive relation for the current density can be derived (see [Sel12]):

$$\mathbf{J}_n = -q\mu_n n \nabla \varphi_n, \tag{4.8}$$

where μ_n denotes the electron mobility respectively $\left[\mathrm{m^2V^{-1}s^{-1}}\right]$ and φ_n is the *electrochemical potential* [V], accounting for both electrical and chemical interactions between charges. At equilibrium the electrochemical potential is spatially constant, while in the non-equilibrium case it is a function of position.

The total number of charge carriers at a given energy can be estimated by means of statistical mechanics models. Let $\mathscr{E}_{LUMO}$ and $\mathscr{E}_{HOMO}$ be the energy levels corresponding to the molecular orbitals LUMO and HOMO respectively, and let $g(\mathscr{E})$ the Density of States (DOS) function; the quantity $g(\mathscr{E})\mathrm{d}\mathscr{E}$ represents the density of available quantum states (per unit volume) that may have energy within an infinitesimal range $\mathrm{d}\mathscr{E}$ of energies centered at $\mathscr{E}$. The total amount of charge carriers per unit volume is thus expressed as the sum over all the admissible energies of the DOS function weighted on the probability of occupation for that state:

$$n = \int_{-\infty}^{+\infty} g\left(\mathscr{E} - \mathscr{E}_{LUMO}\right) \cdot f_D\left(\mathscr{E} - \mathscr{E}_F\right) \mathrm{d}\mathscr{E}, \tag{4.9}$$

where the function $f_D(\mathscr{E})$ denotes the occupation probability of the state having energy $\mathscr{E}$ and $\mathscr{E}_F$ denotes the Fermi level, a quantity related to the electrochemical potential. For a population of fermions, i.e. a system of many particles obeying the Pauli exclusion principle[1], the occupation probability is given by the Fermi-Dirac statistics, which is the statistical distribution identified through the density function:

$$f_D(\mathscr{E}) = \frac{1}{1 + \exp\left(\frac{\mathscr{E}}{k_B T}\right)}.$$

The Fermi-Dirac statistics represents, according to the Pauli exclusion principle ($f_D(\mathscr{E}) < 1 \ \forall \mathscr{E}$), the average number of electrons occupying the state having energy $\mathscr{E}$.

We define the **Fermi level** $\mathscr{E}_F$ [J] as the thermodynamic work required to add one electron to a fermion system [Kit08]. An understanding of how it relates to the electronic structure is essential to describe the physics of a solid-state system. The Fermi level does not necessarily correspond to an actual energy level (for example, in an insulator the Fermi level lies in the band gap).

Remark 4.1. By definition, the Fermi level is such that:

$$f_D\left(\mathscr{E}_F\right) = \frac{1}{2},$$

which means that an electron or a hole has a 50% probability to occupy the energy level $\mathscr{E}_F$.

[1] The Pauli exclusion principle states that the same quantum state cannot be occupied simultaneously by two identical fermions.

Equation (4.9) rigorously applies to a system at thermal equilibrium, where $\mathscr{E}_F$ is a constant. In a system out of equilibrium we can assume a generalized version of eq. (4.9) to hold, by allowing the Fermi level $\mathscr{E}_F$ to depend on spatial coordinates; it turns out that the resultant force acting on a particle is proportional to the gradient of such *quasi-Fermi* energy. Therefore it is related to the electrochemical potential by an affine relation and we can choose, without loss of generality:

$$\mathscr{E}_F = -q\varphi_n.$$

This expression, together with eq. (4.7), gives the constitutive relation:

$$n = n(\varphi, \varphi_n) = \int_{-\infty}^{+\infty} g\left(\mathscr{E} + q\varphi\right) \cdot f_D\left(\mathscr{E} + q\varphi_n\right) \mathrm{d}\mathscr{E}. \tag{4.10}$$

Remark 4.2. At high energies, i.e. when $\mathscr{E} \gg k_B T + \mathscr{E}_F$, then the Fermi-Dirac distribution can be approximated as:

$$f_D(\mathscr{E}) \approx \exp\left(-\frac{\mathscr{E} - \mathscr{E}_F}{k_B T}\right), \tag{4.11}$$

which is called the *Maxwell-Boltzmann statistics*. Carrier densities usually involved in typical organic semiconductor devices are such that the Fermi level lies inside a region where the DOS function is not negligible; therefore the Maxwell-Boltzmann approximation can not be used except for a narrow range of energy values.

Definition 4.1. The quantity $V_{th} = \frac{k_B T}{q}$ is defined *thermal voltage*. At the room temperature $T = 300K$, its value is $V_{th} \approx 26mV$.

4.3 Generalized Einstein relation

Definition 4.2. We now define a *chemical potential* ϕ as:

$$\phi = \varphi - \varphi_n. \tag{4.12}$$

Remark 4.3. The definition above is compatible with [Mad95], while other authors [AM88] use swapped definitions for chemical and electrochemical potentials.

From eq. (4.10), after a change of variables, the electron density can be represented as a function of the chemical potential, i.e. $n = n(\phi)$. Therefore its spatial gradient is computed as:

$$\nabla n = \frac{\partial n}{\partial \phi}\left(\nabla\varphi - \nabla\varphi_n\right).$$

By substituting this expression into eq. (4.8) we get:

$$\mathbf{J}_n = -q\mu_n n\nabla\varphi + qD_n\nabla n, \tag{4.13}$$

which corresponds to the familiar **drift-diffusion** constitutive relation for the electron current density; here we have introduced the electron diffusion coefficient $\left[\mathrm{m}^2\mathrm{s}^{-1}\right]$:

$$D_n = \mu_n \frac{n}{\frac{\partial n}{\partial \phi}}. \tag{4.14}$$

Equation (4.14) provides an generalization of the relation discovered by Einstein and Smoluchowski in their analysis on the Brownian motion [ES99], valid for a general DOS shape.

It can be easily shown that the classical Einstein relation can be deduced as a particular case of eq. (4.14) through an appropriate choice for the function $g(\mathscr{E})$. For example, let us consider the typical DOS function for an inorganic semiconductor:

$$g(\mathscr{E}-\mathscr{E}_c) \propto \sqrt{\mathscr{E}-\mathscr{E}_c}\cdot \mathbb{1}_{\{\mathscr{E}>\mathscr{E}_c\}},$$

where the proportionality is intended up to a multiplicative constant, $\mathbb{1}$ denotes the indicator function and $\mathscr{E}_c$ is the energy of the bottom of the conduction band (analogous to the $\mathscr{E}_{LUMO}$ in an organic semiconductor), and the *zero-disorder* limit for an organic semiconductor:

$$g(\mathscr{E}-\mathscr{E}_{LUMO}) \propto \delta(\mathscr{E}-\mathscr{E}_{LUMO}),$$

where $\delta(\mathscr{E}-\mathscr{E}_{LUMO})$ denotes the Dirac delta centered at $\mathscr{E}_{LUMO}$. Under the Maxwell-Boltzmann approximation (4.11) in both cases we get:

$$n(\phi) \propto \exp\left(\frac{\phi}{V_{th}}\right) \quad\Longrightarrow\quad \frac{\partial n}{\partial \phi} = \frac{1}{V_{th}} n \quad\Longrightarrow\quad D_n = \mu_n V_{th}.$$

In the following we will make use of a function $\alpha(n)$ representing the *deviation* of the diffusion coefficient from the classical Einstein relation:

$$\alpha(n(\phi)) = \frac{1}{V_{th}} \frac{n}{\frac{\partial n}{\partial \phi}}. \tag{4.15}$$

Therefore we write:

$$\boxed{D_n = \mu_n V_{th}\cdot \alpha(n(\phi)).} \tag{4.16}$$

4.4 Constitutive relations for the Density of States

In the literature there is no definitive consensus as to the best choice for the shape of the DOS function $g(\cdot)$ in eq. (4.10) for organic materials [Mad+15]. We assume it to belong to a family of given functions parametrized by a single parameter (*DOS width*, later denoted by σ) corresponding to the **degree of disorder** of the system. Several models have been proposed, including:

1. a single symmetric gaussian [FT09; Poe+13; Mar+09];
2. a linear combination of symmetric gaussians [Kwo+12];
3. an exponential [VW11; Riv+11; RE11];
4. an asymmetric gaussian [TM11];
5. a combination of a gaussian and an exponential [Vri+13; Cho+14];
6. others [VW09; Hul+04].

From now on we will focus on the first two cases.

4.4.1 Single gaussian

The ansatz based on a single gaussian is motivated by the physical plausibility in the case of organic materials [Wei+06]. The DOS function is the following:

$$g_\sigma(\mathscr{E}) = \frac{N_0}{\sqrt{2\pi}\sigma} \exp\left(-\frac{\mathscr{E}^2}{2\sigma^2}\right),$$

where:

N_0 the total number of available states (per unit volume) $\left[\mathrm{m}^{-3}\right]$;

σ the disorder parameter [J], corresponding to the standard deviation of the gaussian.

Thus eq. (4.10) becomes:

$$n = \frac{N_0}{\sqrt{2\pi}\sigma} \int_{-\infty}^{+\infty} \exp\left(-\frac{(\mathscr{E}-\mathscr{E}_{LUMO})^2}{2\sigma^2}\right) \frac{1}{1+\exp\left(\frac{\mathscr{E}-\mathscr{E}_F}{k_B T}\right)} \mathrm{d}\mathscr{E}, \tag{4.17}$$

where $\mathscr{E}_{LUMO} = -q\varphi$ according to eq. (4.7).

We aim to rewrite eq. (4.17) in order to exploit a gaussian quadrature formula for efficiently computing the integrals in numerical simulations.

By substituting:

$$\eta = \frac{\mathscr{E}-\mathscr{E}_{LUMO}}{\sqrt{2}\sigma} \tag{4.18}$$

into eq. (4.17) we obtain:

$$n(\phi) = \frac{N_0}{\sqrt{\pi}} \int_{-\infty}^{+\infty} e^{-\eta^2} \left(1 + \exp\left(\frac{\sqrt{2}\sigma\eta - q\phi}{k_B T}\right)\right)^{-1} \mathrm{d}\eta, \tag{4.19}$$

where ϕ is the chemical potential introduced in section 4.3.
Now we compute the derivatives of eq. (4.17) with respect to the electric potential φ and the chemical potential ϕ (of order 1 and 2), playing an important role in the application of a Newton's method (which will be described in chapter 8).
From eq. (4.17) we compute:

$$\frac{\partial n}{\partial \varphi}(\varphi) = \frac{N_0}{\sqrt{2\pi}\sigma} \int_{-\infty}^{+\infty} \exp\left(-\frac{(\mathscr{E} + q\varphi)^2}{2\sigma^2}\right) \frac{1}{1 + \exp\left(\frac{\mathscr{E} - \mathscr{E}_F}{k_B T}\right)} \cdot \frac{-2(\mathscr{E} + q\varphi)q}{2\sigma^2} \mathrm{d}\mathscr{E},$$

which becomes, through eq. (4.18):

$$\frac{\partial n}{\partial \varphi}(\varphi) = -\frac{N_0 q}{\sigma} \sqrt{\frac{2}{\pi}} \int_{-\infty}^{+\infty} \eta e^{-\eta^2} \left(1 + \exp\left(\frac{\sqrt{2}\sigma\eta - q\phi(\varphi)}{k_B T}\right)\right)^{-1} \mathrm{d}\eta. \tag{4.20}$$

Similarly, from eq. (4.19):

$$\frac{\partial n}{\partial \phi}(\phi) = \frac{N_0}{V_{th}\sqrt{\pi}} \int_{-\infty}^{+\infty} e^{-\eta^2} \frac{\exp\left(\frac{\sqrt{2}\sigma\eta - q\phi}{k_B T}\right)}{\left(1 + \exp\left(\frac{\sqrt{2}\sigma\eta - q\phi}{k_B T}\right)\right)^2} \mathrm{d}\eta \tag{4.21}$$

and:

$$\frac{\partial^2 n}{\partial \phi^2}(\phi) = \frac{N_0}{V_{th}^2\sqrt{\pi}} \int_{-\infty}^{+\infty} e^{-\eta^2} \frac{\exp\left(\frac{\sqrt{2}\sigma\eta - q\phi}{k_B T}\right)}{\left(1 + \exp\left(\frac{\sqrt{2}\sigma\eta - q\phi}{k_B T}\right)\right)^2} \left(\frac{2\exp\left(\frac{\sqrt{2}\sigma\eta - q\phi}{k_B T}\right)}{1 + \exp\left(\frac{\sqrt{2}\sigma\eta - q\phi}{k_B T}\right)} - 1\right) \mathrm{d}\eta.$$

(4.22)

4.4.2 Multiple gaussians

The i-th gaussian is characterized by three parameters:

- $N_{0,i}$: the total number of available states (per unit volume) $\left[\mathrm{m}^{-3}\right]$;
- σ_i: the disorder parameter [J] (standard deviation);
- $\phi_{s,i}$: the (spatially constant) shift of the chemical potential with respect to the first gaussian (by definition, $\phi_{s,1} = 0$).

Let k be the total number of gaussians considered; eq. (4.19) can be generalized as follows:

$$n(\varphi) = \sum_{i=1}^{k} \left(\frac{N_{0,i}}{\sqrt{\pi}} \int_{-\infty}^{+\infty} e^{-\eta^2} \left(1 + \exp\left(\frac{\sqrt{2}\sigma_i \eta - q\left(\phi + \phi_{s,i}\right)}{k_B T} \right) \right)^{-1} \mathrm{d}\eta \right).$$

By linearity, eq. (4.20) becomes:

$$\frac{\partial n}{\partial \varphi}(\varphi) = \sum_{i=1}^{k} \left(-\frac{N_{0,i} q}{\sigma_i} \sqrt{\frac{2}{\pi}} \int_{-\infty}^{+\infty} \eta e^{-\eta^2} \left(1 + \exp\left(\frac{\sqrt{2}\sigma_i \eta - q\left(\phi(\varphi) + \phi_{s,i}\right)}{k_B T} \right) \right)^{-1} \mathrm{d}\eta \right)$$

and similarly eqs. (4.21) and (4.22) can be generalized.

5 EGDM mobility model

In [Coe+05; VMC08] is presented the Extended Gaussian Disorder Model (EGDM), which is valid for a single gaussian DOS (see section 4.4.1) and proceeds on the assumption that on-site energies $\mathscr{E}_i$ in eq. (4.2) are gaussian-distributed (see section 4.4.1) and have no spatial correlation. For materials where the energies are spatially correlated Bouhassoune et al. presented in [Bou+09b] the Extended Correlated Disorder Model (ECDM).
Both approaches determine the mobility (eq. (4.3)) starting from a numerical solution of the Master equation (4.1). For the EGDM it has been shown a dependence of the mobility on:

1. the temperature T;
2. the charge carrier density;
3. the component of the electric field in the direction of the motion of charge carriers $E_\parallel$ (later simply denoted as E).

More specifically, it was found that only at high voltages and low temperatures the dependence on the field plays a role. This functional dependence leads to excellent agreement between calculated and measured *current-voltage* characteristics [Bou+09a].
By defining the following quantities:

$$\hat{\sigma} = \frac{\sigma}{k_B T},$$
$$\delta(\hat{\sigma}) = 2\frac{\log\left(\hat{\sigma}^2 - \hat{\sigma}\right) - \log(\log(4))}{\hat{\sigma}^2},$$
$$c_1(n) = \min\left\{\frac{n}{N_0}, 0.1\right\},$$
$$c_2(E) = \min\left\{\frac{qE}{N_0^{1/3}\sigma}, 2\right\},$$

the complete EGDM for the electron mobility coefficient reads [Coe+05; VMC08]:

$$\begin{cases} \mu_n(T,n,E) = \mu_{0,n}(T) \cdot g_1(n,T) \cdot g_2(E,T), \\ \quad \mu_{0,n}(T) = \bar{\mu}_{0,n} \exp\left(-c_0 \hat{\sigma}^2\right) \\ \quad g_1(n,T) = \exp\left[\frac{1}{2}\left(\hat{\sigma}^2 - \hat{\sigma}\right)(2c_1(n))^{\delta(\hat{\sigma})}\right], \\ \quad g_2(E,T) = \exp\left[0.44\left(\hat{\sigma}^{3/2} - 2.2\right)\right] \cdot \left[\sqrt{1 + 0.8 c_2(E)^2} - 1\right], \end{cases} \tag{5.1}$$

where:

c_0 a dimensionless parameter;

$\bar{\mu}_{0,n}$ the low-field and low-charge-density mobility $\left[\mathrm{m^2 V^{-1} s^{-1}}\right]$.

By a slight abuse of notation, we will later refer to the function $\mu_{0,n}(T)$ as the low-field and low-charge-density mobility. The functions $g_1(\cdot)$ and $g_2(\cdot)$ are called *enhancement factors*.

Remark 5.1. The DOS width σ parameter and $\mu_{0,n}$ play a leading role in the DD system because of the EGDM. Nevertheless, their experimental measurement is not possible but their value is desirable, which is why parameter estimation problems have to be solved in order to completely close the DD system.

Remark 5.2. The EGDM model introduces further non-linearities into the DD system (see [Kna+10]) because of the functional dependence of μ_n on the system variables n and φ, thus affecting the overall efficiency of non-linear iteration strategies. Therefore, standard discretization schemes has to be properly adapted and generalized for taking into account the peculiar physical model of organic semiconductor.

Part III of this thesis will concern about numerical techniques to address the identification of the σ and $\mu_{0,n}$ parameters and to solve the DD system in the unsteady regime.

6 One-dimensional modeling of OTFTs

OTFT are usually characterized by extreme aspect ratios L/W (see fig. 6.1), which warrant for separate modeling of:

- charge accumulation in the z-direction (segment AA), corresponding to the MIS capacitor;
- charge transport in the y-direction (segment BB), by assuming simmetry along the x-direction.

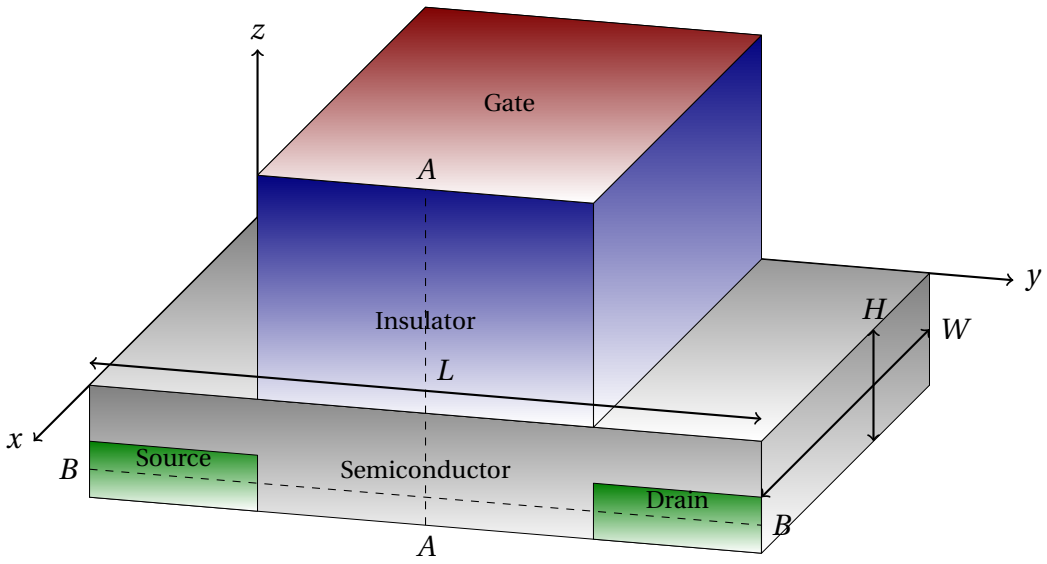

Figure 6.1: Geometrical setting of the OTFT.

6.1 Model simplifications

Under this geometrical setting, the continuum model presented in section 4.2, making use of the assumptions discussed in section 4.2.2, can be rewritten as:

$$\begin{cases} -\nabla\cdot\left(\varepsilon\nabla\varphi\right)+qn=0, & \text{in } \Omega\times[0,T], \quad (6.1a)\\ \dfrac{\partial n}{\partial t}-\dfrac{1}{q}\nabla\cdot J_n=0, & \text{in } \Omega_{sc}\times[0,T], \quad (6.1b)\\ J_n=-q\mu_n n\nabla\varphi_n, & \text{in } \Omega\times[0,T], \quad (6.1c)\\ n=n(\varphi,\varphi_n), & \text{in } \Omega_{sc}\times[0,T], \quad (6.1d)\\ n=0, & \text{in } \Omega_{ins}\times[0,T], \quad (6.1e) \end{cases}$$

where T is the final time-step. Equation (6.1d) represents the constitutive relation (4.10). The separate modeling of the OTFT in the z- and y-directions allows to simplify the system (6.1) in the two cases:

- **quasi-static** simulation in the z-direction; the continuity equation (6.1b) and eq. (6.1e) give $J_n=0$, i.e. the electrochemical potential φ_n is spatially constant and can be set equal to 0 [V] without loss of generality. Therefore from eq. (6.1d) we get that the electron density n is a function of the electric potential φ only. Thus the model can be simplified into the *non-linear Poisson's equation*:

$$\begin{cases} -\dfrac{\partial}{\partial z}\left(\varepsilon\dfrac{\partial\varphi}{\partial z}\right)+qn=0, & \text{in } \Omega, \quad (6.2a)\\ n=n(\varphi), & \text{in } \Omega_{sc}, \quad (6.2b)\\ n=0, & \text{in } \Omega_{ins}. \quad (6.2c) \end{cases}$$

  Here $\Omega=[-t_{sc},t_{ins}]$, $\Omega_{sc}=[-t_{sc},0]$ and $\Omega_{ins}=(0,t_{ins}]$ (segment AA), where t_{sc} and t_{ins} are the thicknesses of the semiconductor and the insulator layer respectively. The function $n=n(\varphi)$ is evaluated from eq. (4.10).

- **low drain-to-source voltage** (V_{DS}) application, i.e. simulation of current conduction in the y-direction in the linear regime (segment BB); in this case the current is proportional to V_{DS}. We then assume that that the electron density is spatially constant and the resultant force acting on a particle is proportional to V_{DS} too. Therefore we approximate:

$$\nabla\varphi\approx\nabla\varphi_n\approx-\frac{V_{DS}}{L}, \quad (6.3)$$

  so that no partial differential equation has to be solved in this case.

6.2 Boundary conditions

We need to specify appropriate boundary conditions for eq. (6.1) in order to guarantee the well-posedness of the problem.

6.2.1 Bulk contact: charge injection

The physical phenomenon considered at the **bulk** contact (corresponding to $z = -t_{sc}$) is the presence of a *Schottky barrier*, i.e. a potential energy barrier for electrons formed at a metal-semiconductor interface [Tun14].

Out of thermal equilibrium, the electrical current flowing across the interface between a metal and a semiconductor is influenced by a discontinuity on the energy scale of the electronic states responsible for conduction in the two materials. Delocalized electronic states around the Fermi level are responsible for the electrical conduction in the metal, but these states are not coupled to any delocalized electronic state in the semiconductor, depending on the doping type: in n-type semiconductors the electrons near the LUMO are primarily responsible for electrical conduction and they are at an energy $-q\Phi_B$ (where Φ_B is the potential barrier) above the Fermi level. This energy offset is known as the Schottky barrier height and is such that the flow of electrons from the semiconductor to the metal is easier than conduction in the opposite direction. We now define two important physical quantities used to model the potential barrier.

Definition 6.1. In solid-state electronics, the **work function** W_f [J] is the minimum thermodynamic work needed to remove an electron from the Fermi level to the vacuum immediately outside the solid surface. In a semiconductor, the work function depends on the doping level at the surface.

Definition 6.2. The **electron affinity** E_a [J] in semiconductor physics is the minimum thermodynamic work needed to remove an electron from the LUMO level to the vacuum level.

The potential barrier can thus be expressed as:

$$\Phi_B = -\frac{W_f - E_a}{q}, \tag{6.4}$$

W_f being the metal work function and E_a the semiconductor electron affinity.

Scott and Malliaras [SM99] also considered a mechanism of (thermionic) charge injection from metals into organic semiconductors, which plays an important role in devices such as OLEDs, where metal electrodes inject charge carriers into the opposite sides of the emissive organic layer, organic photoconductors (used in laser printers

and photocopiers), where the photogenerated charge must be extracted from the polymer film, and OTFTs too. Here the effect of the *image potential* (induced by charges in the metal) on injected carriers is modeled as a recombination activated from a Coulomb interaction through an hopping process. The physics of charge injection can be mathematically represented by making use of a corrected potential barrier [VDH+09]:

$$\Phi'_B = \Phi_B + \sqrt{\frac{qE_c}{4\pi\varepsilon_{sc}}}, \tag{6.5}$$

where E_c is the electric field at the contact surface.

The boundary condition for the electric potential φ must then take into account a shift equal to Φ_B (or Φ'_B, for the corrected model).

6.2.2 Gate contact: applied voltage

At the insulator contact a shift of the electric potential V_{shift} is considered, due to effects such as permanent dipoles, fixed charge in dielectrics or metal work function mismatch [Mad+15]. In section 8.4 we will discuss a way to extract this parameter by comparing numerical results with experimental data.

6.2.3 External control circuit

We suppose that the device contacts are connected to an external control circuit. The circuit's evolution can be described by the Modified Nodal Analysis (MNA) equation obtained from the Kirchhoff's circuit laws and the constitutive relations for the electronic components connected to the circuit. It can be written as:

$$A\dot{\mathbf{F}} + \mathbf{C}(\mathbf{F}) + r\mathbf{I} = 0, \tag{6.6}$$

where:

- $\mathbf{F}$ the state vector, containing the circuit variables (such as voltages, magnetic fluxes, currents, total charges, ...);
- $\mathbf{I}$ the vector of the inward currents on contacts;
- r an incidence matrix, which accounts for attaching each device contact to a circuit node.

Here $\mathbf{C}(\mathbf{F}) = B\mathbf{F} + \mathbf{s}$ and A, C are matrices; the dot denotes the time derivative.

Let V_b and V_g be the components of $\mathbf{F}$ corresponding to the voltages of the circuit nodes connected to the bulk and gate contact respectively; the boundary conditions

for the electric potential are of Dirichlet type:

$$\begin{cases} \varphi(-t_{sc}, t) = V_b(t) + \Phi_B, \\ \varphi(t_{ins}, t) = V_g(t) + V_{shift}, \end{cases} \tag{6.7}$$

$\forall\, t \in [0, T]$.

6.2.4 Continuity equation

The boundary conditions imposed for the continuity equation are:

$$\begin{cases} n(-t_{sc}, t) = n\left(\varphi(-t_{sc}, t), V_b(t)\right), \\ J_n(0, t) = 0, \end{cases} \tag{6.8}$$

$\forall\, t \in [0, T]$.

The bulk contact Dirichlet condition is evaluated through the constitutive relation chosen for the DOS according to eq. (4.10): for example, in the case of a gaussian DOS (eq. (4.19)), by substituting eq. (6.7) the boundary condition reads:

$$n(-t_{sc}, t) = \frac{N_0}{\sqrt{\pi}} \int_{-\infty}^{+\infty} e^{-\eta^2} \left(1 + \exp\left(\frac{\sqrt{2}\sigma\eta - q\Phi_B}{k_B T}\right)\right)^{-1} \mathrm{d}\eta.$$

At the semiconductor-insulator interface we imposed an homogeneous Neumann (natural) condition.

6.3 Computation of contact currents

The vector of currents **I** in eq. (6.6) is computed using the **residue method** [GS06], based on the property of local conservation [Hug+00] which holds for discretization schemes derived from the Galërkin method (such as finite elements and finite volumes).

The total current at the i-th contact is the sum of two contributions due to the displacement current and the conduction current:

$$I_i = S\left[\left(\frac{\partial D}{\partial t} + J_n\right)\nu\right]_i, \tag{6.9}$$

where S is the device area $\left[\mathrm{m}^2\right]$, $D = \varepsilon E = -\varepsilon\frac{\partial \varphi}{\partial z}$ is the electric displacement field $\left[\mathrm{C}\cdot\mathrm{m}^{-2}\right]$ and ν the inward unit normal.

Displacement current

We write the variational formulation of eq. (6.1a) by multiplying by a trial function $\psi \in H^1(\Omega)$ and integrating by parts:

$\forall t \in [0, T]$ find $\varphi(t) \in H^1(\Omega)$ subject to boundary conditions (6.7) such that:

$$\int_{-t_{sc}}^{t_{ins}} \varepsilon \frac{\partial \varphi}{\partial z} \frac{\partial \psi}{\partial z} \mathrm{d}z - \left[\varepsilon \frac{\partial \varphi}{\partial z} \psi \right]_{-t_{sc}}^{t_{ins}} + \int_{-t_{sc}}^{t_{ins}} qn\psi \mathrm{d}z = 0, \quad \forall \psi \in H^1(\Omega), \psi|_{\partial\Omega} = 0.$$

Since the Galërkin method is locally conservative [Hug+00], we can choose ψ among the basis functions omitted to satisfy the Dirichlet boundary conditions [GS06].

For:

$$\psi(z) = \psi_1(z) = \begin{cases} 1, & z = -t_{sc}, \\ 0, & z \neq -t_{sc}, \end{cases}$$

we get:

$$\int_{-t_{sc}}^{t_{ins}} \varepsilon \frac{\partial \varphi}{\partial z} \frac{\partial \psi_1}{\partial z} \mathrm{d}z + \varepsilon \frac{\partial \varphi}{\partial z} (-t_{sc}) + \int_{-t_{sc}}^{t_{ins}} qn\psi_1 \mathrm{d}z = 0,$$

and finally:

$$(D\nu)(-t_{sc}) = -\varepsilon \frac{\partial \varphi}{\partial z} (-t_{sc}) = \int_{-t_{sc}}^{t_{ins}} \varepsilon \frac{\partial \varphi}{\partial z} \frac{\partial \psi_1}{\partial z} \mathrm{d}z + \int_{-t_{sc}}^{t_{ins}} qn\psi_1 \mathrm{d}z, \tag{6.10}$$

where ψ_1 is the first basis function of the discretization scheme considered.

Similarly, for:

$$\psi(z) = \psi_K(z) = \begin{cases} 1, & z = t_{ins}, \\ 0, & z \neq t_{ins}, \end{cases}$$

where K is the total number of the discretization degrees of freedom, we get:

$$\int_{-t_{sc}}^{t_{ins}} \varepsilon \frac{\partial \varphi}{\partial z} \frac{\partial \psi_K}{\partial z} \mathrm{d}z - \varepsilon \frac{\partial \varphi}{\partial z} (t_{ins}) + \int_{-t_{sc}}^{t_{ins}} qn\psi_K \mathrm{d}z = 0,$$

and finally:

$$(D\nu)(t_{ins}) = +\varepsilon \frac{\partial \varphi}{\partial z} (t_{ins}) = \int_{-t_{sc}}^{t_{ins}} \varepsilon \frac{\partial \varphi}{\partial z} \frac{\partial \psi_K}{\partial z} \mathrm{d}z + \int_{-t_{sc}}^{t_{ins}} qn\psi_K \mathrm{d}z. \tag{6.11}$$

Then the total displacement current at the i-th contact is:

$$S \left(\frac{\partial D}{\partial t} \nu \right)_i.$$

Conduction current

We write the variational formulation of eq. (6.1b) by multiplying by a trial function $\gamma \in H^1(\Omega)$ and integrating by parts:

$\forall\, t \in [0,T]$ find $n(t) \in H^1(\Omega)$ subject to boundary conditions (6.8) such that:

$$\int_{-t_{sc}}^{0} \frac{\partial n}{\partial t}\gamma \mathrm{d}z + \frac{1}{q}\int_{-t_{sc}}^{0} J_n \frac{\partial \gamma}{\partial z}\mathrm{d}z + \frac{1}{q}\left(J_n\gamma\right)(-t_{sc}) = 0, \quad \forall \gamma \in H^1(\Omega), \gamma(-t_{sc}) = 0,$$

where we have exploited the boundary condition eq. (6.8).

For:

$$\gamma(z) = \gamma_1(z) = \begin{cases} 1, & z = -t_{sc}, \\ 0, & z \neq -t_{sc}, \end{cases}$$

we get:

$$\left(J_n \nu\right)(-t_{sc}) = J_n(-t_{sc}) = -q\int_{-t_{sc}}^{0} \frac{\partial n}{\partial t}\gamma_1 \mathrm{d}z - \int_{-t_{sc}}^{0} J_n \frac{\partial \gamma_1}{\partial z}\mathrm{d}z, \tag{6.12}$$

while $J_n(t_{ins}) = 0$ because of eqs. (6.1e) and (6.8).

The total conduction current at the i-th contact is then:

$$S\left(J_n \nu\right)_i.$$

Remark 6.1. The volume integrals in eqs. (6.10) to (6.12) can be easily computed starting from stiffness and mass matrices obtained by the discrete formulation.

7 Correlation between DOS and capacitance in a MIS capacitor

Capacitance-Voltage ($C-V$) curves allow a promising approach for probing the DOS parameter σ by fitting numerical and experimental results [Mad+15].

In the case of a gaussian DOS (section 4.4.1) (other cases are treated analogously) the system eq. (6.2), valid only in the quasi-static approximation, becomes:

$$\begin{cases} -\dfrac{\partial}{\partial z}\left(\varepsilon\dfrac{\partial\varphi}{\partial z}\right)+qn=0, & \text{in } \Omega, \qquad (7.1a)\\ n=\dfrac{N_0}{\sqrt{\pi}}\displaystyle\int_{-\infty}^{+\infty}\frac{e^{-\eta^2}}{\left(1+\exp\left(\frac{\sqrt{2}\sigma\eta-q\varphi}{k_BT}\right)\right)}\mathrm{d}\eta, & \text{in } \Omega_{sc}, \qquad (7.1b)\\ n=0, & \text{in } \Omega_{ins}. \qquad (7.1c) \end{cases}$$

This is a non-linear integro-differential equation for the electric potential φ, with boundary conditions given by eq. (6.7).

At moderately positive gate voltages, $\mathscr{E}_F$ is still located within the HOMO-LUMO gap and far from the DOS (fig. 7.1) [Mad+15], hence no carriers are present in the semiconductor. For larger gate voltages, $\mathscr{E}_F$ starts sweeping the semiconductor DOS, thus determining an accumulation of electrons in the semiconductor.

The spatial distribution of accumulated charges is largely influenced by the disorder parameter σ, as shown in fig. 7.2: the super-linearity of eq. (7.1) tends to produce steep boundary layers for $n(z)$ near the semiconductor-insulator interface, while more disorder implies that more states are close to or even below $\mathscr{E}_F$ and hence occupied, resulting in a smoothing of the peak in $n(z)$. This phenomenon can be exploited in order to extract the DOS width σ, considered that it is more convenient to probe a perturbation $\delta n(z)$ instead of directly $n(z)$; in fact, the additional accumulation charge induced by a small signal δV_g can be experimentally obtained by means of simple electrical measurements such as $C-V$ curves.

Therefore, once solved eq. (7.1) (for example, by means of a non-linear functional iteration technique), the differential capacitance C [F] can be the evaluated as $\frac{\delta Q}{\delta V_g}$,

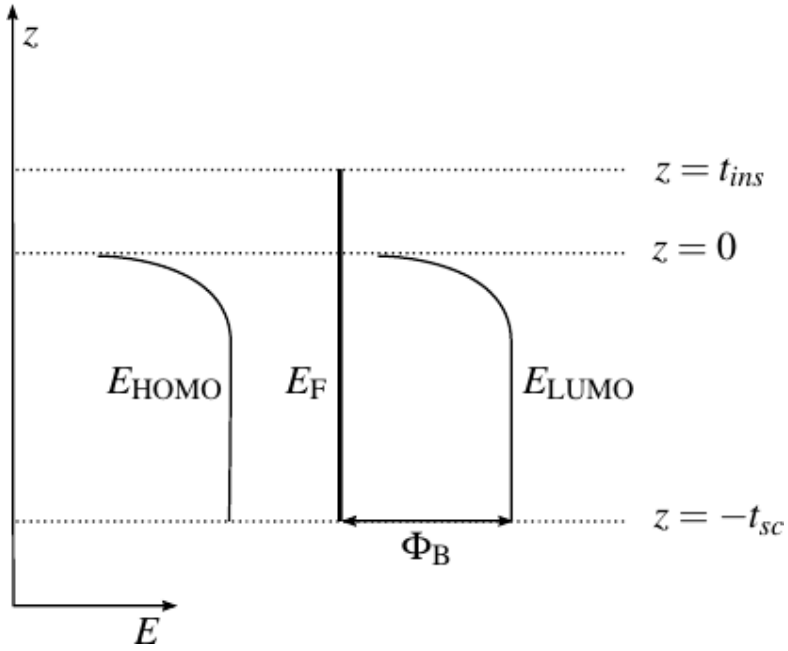

Figure 7.1: Energy levels in a MIS capacitor. Source: [Mad+15].

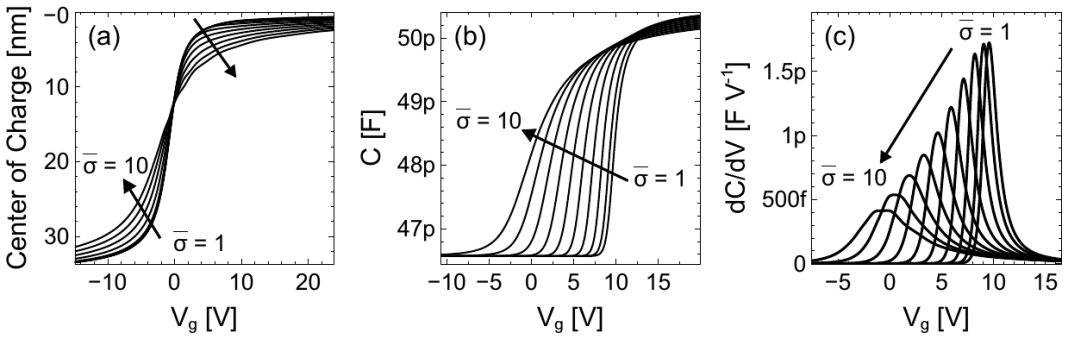

Figure 7.2: Influence of the disorder parameter σ on accumulated charge and capacitance. Source: [Mad+15].

where δQ is the variation of the total charge Q accumulated at the gate contact at the bias V_g and δV_g the gate voltage perturbation. In chapter 8 we will explain how to accurately compute C and its derivative $\frac{dC}{dV_g}$, used in the fitting algorithm, without resorting to differentiation techniques which lead to numerical instabilities.

Part III Numerical methods

8 σ extraction: fitting $C-V$ curves

The aim of this chapter is to describe an algorithm for extracting the disorder parameter σ by fitting $C-V$ curves. We consider a MIS capacitor in the quasi-static regime: the device is always at equilibrium and no transport phenomena are involved; the Fermi level $\mathscr{E}_F$ is spatially constant, thus it can be set equal to 0 [J] with no loss of generality.

8.1 Linearization: Newton's method

The non-linear Poisson's eq. (7.1) has been linearized through a Newton's method. The equation can be written as $\mathfrak{F}(\varphi) = 0$, where $\mathfrak{F} : H^1(\Omega) \to \mathbb{R}$ is an appropriate integro-differential functional.

The non-linear iteration proceeds as follows. Given $\varphi^{(0)}$, solve:

$$\begin{cases} \mathscr{D}\mathfrak{F}\left(\varphi^{(k)}\right)\left[\delta\varphi^{(k)}\right] = -\mathfrak{F}\left(\varphi^{(k)}\right), & \text{(8.1a)} \\ \varphi^{(k+1)} = \varphi^{(k)} + \delta\varphi^{(k)}, & \text{(8.1b)} \end{cases}$$

for each $k \in \mathbb{N}^+$ until convergence. Here the symbol $\mathscr{D}\mathfrak{F}(\varphi)[\chi]$ denotes the **Gâteaux** derivative of the functional $\mathfrak{F}$ at φ in the direction χ, defined as:

$$\mathscr{D}\mathfrak{F}(\varphi)[\chi] = \lim_{\kappa \to 0} \frac{\mathfrak{F}(\varphi + \kappa\chi) - \mathfrak{F}(\varphi)}{\kappa}.$$

The functional derivative can be expressed as:

$$\mathscr{D}\mathfrak{F}\left(\varphi^{(k)}\right)\left[\delta\varphi^{(k)}\right] = -\frac{\partial}{\partial z}\left(\varepsilon\frac{\partial\chi}{\partial z}\right)(z) + q\frac{\partial n}{\partial\varphi}(\varphi)\chi.$$

Therefore eq. (8.1a) becomes:

$$-\frac{\partial}{\partial z}\left(\varepsilon\frac{\partial\left(\delta\varphi^{(k)}\right)}{\partial z}\right)+\left[q\frac{\partial n}{\partial\varphi}\left(\varphi^{(k)}\right)\right]\delta\varphi^{(k)}=-\left[-\frac{\partial}{\partial z}\left(\varepsilon\frac{\partial\left(\varphi^{(k)}\right)}{\partial z}\right)+qn\left(\varphi^{(k)}\right)\right], \tag{8.2}$$

with $n=0$ in Ω_{sc}, which is a diffusion-reaction partial differential equation for $\delta\varphi^{(k)}$. The term $\frac{\partial n}{\partial\varphi}(\cdot)$ is evaluated through eq. (4.20).

Given an initial guess $\varphi^{(0)}$ satisfying eq. (6.7) in the stationary regime, the following boundary conditions are imposed for $\varphi^{(k)}$:

$$\begin{cases}\delta\varphi^{(k)}(-t_{semic})=0,\\ \delta\varphi^{(k)}(t_{ins})=0.\end{cases}$$

A convenient choice for the initial guess is a linear function consistent with eq. (6.7).

Equation (8.2) has been discretized as described in section 10.3.

The stopping criterion used to check the convergence of the Newton's method is based on the L^{∞}-error between two successive iterates.

8.2 Computation of charge density

The integral relations in eqs. (4.19) to (4.20) and (4.22) can be numerically approximated through gaussian, i.e. nodes and weights are unknown, quadrature rules.

The Gauss-Hermite rule allows approximating the integral of a function $f(z)$ multiplied by a gaussian weight $g(z)=e^{-z^2}$:

$$\int_{-\infty}^{+\infty}e^{-z^2}f(z)\mathrm{d}z.$$

The nodes of the Gauss-Hermite quadrature rule of order N are the roots of the N-th Hermite polynomial, defined through the recurrence relation:

$$H_{N+1}(z)=2zH_N(z)-2nH_{N-1}(z),$$

with $H_0(z)=1, H_{-1}(z)=0$.

The integral can thus be approximated as:

$$\int g(z)f(z)\mathrm{d}z\approx\sum_{i=1}^{N}w_i\cdot f(z_i),$$

where $\{z_i\}_{i=1}^{N}$ and $\{w_i\}_{i=1}^{N}$ are the quadrature nodes and weights respectively and can be obtained by means of two different algorithms:

- a direct method [KU98] based on the eigen decomposition of a Jacobi matrix $J \in \mathbb{R}^{N\times N}$ (tridiagonal and symmetric), which can be exploited for families of orthogonal polynomials defined through a recurrence relation; the nodes are the eigenvalues of J and the weights its (scaled) eigenvectors.
- an iterative method [Pre07] based on a Newton's iteration technique; compared to the direct method it is faster (no factorization of large matrices required) but less accurate.

8.3 Computation of the capacitance

Let $\overline{\varphi}(z)$ be the solution of eq. (7.1) for an applied voltage $\overline{V}_g$; the corresponding charge Q [C] (per unit area) on the gate plane can be computed as [Mad+15]:

$$\overline{Q} = \left(-\varepsilon \frac{\partial \overline{\varphi}}{\partial z}\right)(t_{ins}). \tag{8.3}$$

When superimposing a perturbation δV_g to the applied gate voltage, the electric potential will vary by an amount $\delta\varphi$ and the charge by an amount δQ in such a way that:

$$\overline{Q} + \delta Q = \left(-\varepsilon \frac{\partial\left(\overline{\varphi} + \delta\varphi\right)}{\partial z}\right)(t_{ins}),$$

which, using eq. (8.3), leads to:

$$\delta Q = \left(-\varepsilon \frac{\partial \delta\varphi}{\partial z}\right)(t_{ins}). \tag{8.4}$$

Neglecting terms of order 2, $\delta\varphi$ is the solution to the following differential problem:

$$\begin{cases} -\dfrac{\partial}{\partial z}\left(\varepsilon \dfrac{\partial \delta\varphi}{\partial z}\right) + q\left[\dfrac{\partial n}{\partial \varphi}(\overline{\varphi})\right]\delta\varphi = 0, & \text{in } \Omega, \\ n = 0, & \text{in } \Omega_{ins}, \\ \delta\varphi(-t_{sc}) = 0, \\ \delta\varphi(t_{ins}) = \delta V_g. \end{cases} \tag{8.5}$$

Once eq. (8.5) has been solved, the differential capacitance of the device can be computed as:

$$C(V_g) = S\frac{\delta Q}{\delta V_g}, \tag{8.6}$$

where S is the area of the device $\left[\mathrm{m}^2\right]$ and δQ is given by eq. (8.4).
Given the linearity of eq. (8.5), C will not depend on δV_g but only on V_g; therefore it is

convenient to set $\delta V_g = 1$ without loss of generality.

Remark 8.1. Computing first a finite set of samples of the curve $\overline{Q}(V_g)$ and then computing $C(V_g)$ through a difference formula would not have been a valid approach because the fitting procedure also requires computing the derivative $\frac{\mathrm{d}C}{\mathrm{d}V_g}(V_g)$, i.e. the second order derivative of $\overline{Q}(V_g)$, which would lead to numerical instabilities when using standard double-precision floating point numbers [Ant02].

8.4 Post-processing

The post-processing phase consists in comparing numerical results obtained by means of the techniques described in the previous sections and experimental data. $C-V$ curves are evaluated over a sample of applied biases $\mathcal{V}$, usually ranging from the depletion ($V_{g,dep}$) to the accumulation ($V_{g,acc}$) regime [SS98].

Issues related to non-ideal effects introduce additional uncertainties affecting the disorder parameter σ that need to be properly addressed.
A first issue to deal with concerns the gate voltage shift term V_{shift} [Mad+15]. From the experimental point of view, many phenomena can cause a shift of the $C-V$ curve along the horizontal axis, such as permanent dipoles, space charge layers, fixed charge in dielectrics or metal work function mismatch. All these effects are accounted for through the single fitting parameter V_{shift}, computed as the distance between abscissas of the maxima of the simulated and experimental $\frac{\mathrm{d}C}{\mathrm{d}V_g}(V_g)$ curves (see fig. 8.1):

$$V_{shift} = \arg\max_{V_g} \frac{\mathrm{d}C_{sim}}{\mathrm{d}V_g}(V_g) - \arg\max_{V_g} \frac{\mathrm{d}C_{exp}}{\mathrm{d}V_g}(V_g). \tag{8.7}$$

Finally, the $L^2(\Omega)$- and $H^1(\Omega)$- errors and the distance between the ordinates of the peaks in the two curves (*peak-distance*) are computed, together with the **center of charge** t_{CoC} [m] of the perturbed density δn (see chapter 7), dependent on the gate bias V_g and defined as:

$$t_{CoC}(V_g) = \frac{\int_{-t_{semic}}^{0} n(z) z \mathrm{d}z}{\int_{-t_{semic}}^{0} n(z) \mathrm{d}z}.$$

The center of charge allows to compute the equivalent capacitance of the semiconductor layer:

$$C_{sc} = S\frac{\varepsilon_{sc}}{t_{CoC}}.$$

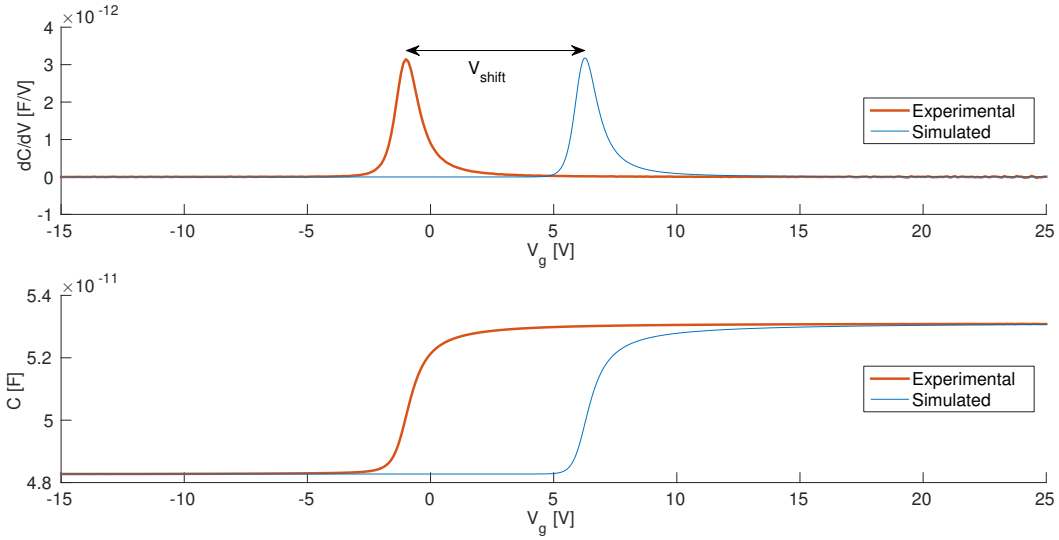

Figure 8.1: Shift of the electric potential caused by non-ideal effects.

8.5 Algorithm for automatic fitting

From now on, we will focus on the **single gaussian** model (section 4.4.1). In addition to the shift of the electric potential, a second non-ideal effect to be accounted for is a parasitic contribution given to the device capacitance [Mad+15], due to a coupling between the metal gate and the bulk contact. This contribution can be modeled as a V_g-independent *stray capacitance* C_{sb} connected in parallel to the MIS capacitor.

Finally, since the semiconductor layer is buried under the insulating film, the measurement of its thickness t_{sc} is subject to uncertainties.

We now describe an iterative algorithm, originally presented in [Mad+15], which allows to automatically find the optimal parameter vector $[\sigma, C_{sb}, t_{semic}]$. The $(k+1)$-th iteration consists of the following steps:

Step 1 Fixed $C_{sb}^{(k)}$ and $t_{semic}^{(k)}$, a finite set of samples for σ is initialized, belonging to the interval $[\sigma^{(k)} - \sigma_n, \sigma^{(k)} + \sigma_p]$, where σ_n and σ_p are parameters initially set by the user. Then the non-linear Poisson's equation is solved (by means of the Newton's method described in section 8.1) for each σ in this set, in order to identify the optimal value $\sigma^{(k+1)}$ minimizing the distance (in terms of $L^2(\Omega)$- or $H^1(\Omega)$- errors or the peak-distance) of the simulated $C-V$ curve from the experimental data.

Step 2 C_{sb} is updated:

$$C_{sb}^{(k+1)} = C_{sb}^{(k)} + C_{exp}(V_{g,acc}) - C_{sim}\left(V_{g,acc}; \left[C_{sb}^{(k)}, t_{semic}^{(k)}, \sigma^{(k+1)}\right]\right).$$

Step 3 t_{semic} is updated:

$$t_{semic}^{(k+1)} = \varepsilon_{semic}\left(\frac{1}{C_{exp}(V_{g,dep}) - C_{sb}^{(k+1)}} - \frac{t_{ins}}{\varepsilon_{ins}}\right).$$

A generalization of this algorithm with respect to [Mad+15] consists in an **adaptive identification** of the parameters σ_n and σ_p, in order to save computational costs and locate the optimal value for the disorder parameter σ with more accuracy:

if $\sigma^{(k+1)} < \sigma^{(k)}$ **then**
  $\sigma_p = \sigma^{(k)} - \sigma^{(k+1)}$
else if $\sigma^{(k+1)} > \sigma^{(k)}$ **then**
  $\sigma_n = \sigma^{(k+1)} - \sigma^{(k)}$
else
  convergence reached!
end

Algorithm 8.1: Adaptive identification of σ_n and σ_p.

While the robustness of this *divide et impera* procedure is well demonstrated by the results obtained, a rigorous study of its mathematical properties has not been carried out and warrants further investigation.

9 μ_0 extraction: fitting $I-V$ curves

Once the disorder parameter σ of the semiconductor has been computed (using the algorithms discussed in chapter 8), *Current-Voltage* ($I-V$) curves allow to probe the low-field and low-charge-density mobility $\mu_{0,n}$ of the EGDM model (chapter 5) by fitting numerical and experimental results, thus showing that the DOS width extraction is a meaningful procedure [Mad+15].

We focus on an OTFT restrained to work in the **linear regime**, i.e. $V_g - V_T \gg V_{DS}$, V_T being the threshold voltage and V_{DS} the drain-to-source voltage (see section 2.1). The DOS width σ is extracted by initially setting $V_{DS} = 0$, so that the mechanism of operation of the device is that of a MIS capacitor.

9.1 Computation of channel resistivity

The relationship between drain-to-source current and gate voltage for a fixed V_{DS} can be expressed as:

$$I_{DS}(V_g) = G_{ch}(V_g)V_{DS}, \tag{9.1}$$

where the channel conductance G_{ch} [℧], implicitly dependent on the applied gate voltage V_g, is given by:

$$G_{ch}(V_g) = \frac{W}{L}\int_{-t_{sc}}^{0} q\mu_n(z)n(z)\mathrm{d}z, \tag{9.2}$$

W being the channel width and L its length. Here the mobility coefficient $\mu_n(z)$, at a fixed temperature T, is expressed in terms of the EGDM model (eq. (5.1)) as:

$$\mu_n(z) = \mu_{0,n} \cdot g_1(n(z)) \cdot g_2(E).$$

The only fitting parameter in this model is the low-field and low-charge-density mobility $\mu_{0,n}$ $\left[\mathrm{m^2V^{-1}s^{-1}}\right]$, since the enhancement factors $g_1(\cdot)$ and $g_2(\cdot)$ can be easily

computed once the DOS width σ has been extracted; moreover, in the linear regime the electric field E can be approximated to be constant from source to drain (see eq. (6.3)):

$$\bar{E} = \frac{V_{DS}}{L}.$$

Finally, we note that eq. (9.2) can be rewritten as:

$$G_{ch}(V_g) = \frac{W}{L}\mu_{n,\text{eff}}(V_g)Q_{ch}(V_g), \tag{9.3}$$

where we have introduced the *total accumulated charge* (per unit area):

$$Q_{ch} = \int_{-t_{sc}}^{0} qn(z)\mathrm{d}z,$$

the *effective mobility*, easily comparable to data collected by experimental measurements:

$$\mu_{n,\text{eff}}(V_g) = \mu_{0,n}\hat{\mu}_{n,\text{eff}}(V_g)$$

and the dimensionless parameter:

$$\hat{\mu}_{n,\text{eff}} = \frac{q}{Q_{ch}}g_1\left(\bar{E}\right)\int_{-t_{sc}}^{0} g_2(n(z))n(z)\mathrm{d}z.$$

9.2 Computation of low-field and low-charge-density mobility

The parameter $\mu_{0,n}$ can be extracted by fitting experimental $I-V$ characteristics. By using a linear *Least Squares* procedure, the parameter identification problem reads:

$$\text{find } \mu_{0,n}^* = \underset{\mu_{0,n}\in\mathbb{R}^+}{\arg\min} \left\| I_{DS}(V_g) - G_{ch}(V_g) \right\|^2, \tag{9.4}$$

where $I_{DS}(V_g)$ is the experimental current-voltage curve and $G_{ch}(V_g)$ is computed by evaluating eq. (9.3) at the simulation results.

The least square estimate is given by the *normal equation*:

$$\mu_{0,n}^* = \frac{\mathbf{i}^T\mathbf{g}}{\mathbf{i}^T\mathbf{i}},$$

where $\mathbf{i}$ and $\mathbf{g}$ are the (column) vectors containing the curves $I_{DS}(\cdot)$ and $\frac{W}{L}\hat{\mu}_{n,\text{eff}}Q_{ch}(\cdot)$, respectively, evaluated at a finite set of samples of the gate voltage V_g.

Remark 9.1. In the linear region eq. (9.1) can be approximated as (see [Sin+08]):

$$I_{DS}(V_g) = \frac{W}{L} C_{ins} V_{DS} \mu_n \cdot (V_g - V_T),$$

where C_{ins} is the capacitance of the insulator layer (per unit area). This approximation gives:

$$\mu_n(V_g) = \frac{1}{\frac{W}{L} C_{ins} V_{DS}} \frac{\mathrm{d}I_{DS}}{\mathrm{d}V_g}(V_g), \tag{9.5}$$

which provides an alternative way to compute the mobility coefficient. A comparison between the complete EGDM model (9.4) and the *compact model* (9.5) will be drawn in chapter 12.

10 Unsteady simulation of OTFTs

In this chapter we consider the complete DD system, now totally closed as the unknown parameters of the EGDM model σ and $\mu_{0,n}$ have been extracted by fitting $C-V$ and $I-V$ experimental curves.

The DD system (6.1), coupled with the external control circuit (section 6.2.3) and with the equation for the contact currents (section 6.3), reads:

$$\begin{cases} -\left(\varepsilon\varphi'\right)' + qn = 0, & \text{in } \Omega \times [0,T], \quad (10.1a) \\ \dfrac{\partial n}{\partial t} - \left(\mu_n(n) V_{th}\left(\alpha(n)n' - \dfrac{n}{V_{th}}\varphi'\right)\right)' = 0, & \text{in } \Omega_{sc} \times [0,T], \quad (10.1b) \\ A\dot{\mathbf{F}} + \mathbf{C}(\mathbf{F}) + r\mathbf{I} = 0, & \quad (10.1c) \\ I_i - S\left[\left(\dfrac{\partial D}{\partial t} + J_n\right)\nu\right]_i = 0, & \forall i \in \partial\Omega \times [0,T], \quad (10.1d) \end{cases}$$

where $(\cdot)'$ denotes the partial derivative in the z-direction.

10.1 Time semi-discretization

The semi-discretization in time of eq. (10.1) has been carried out by means of the **Implicit Euler** method. Let $\{t_m\}_{m=0}^{M} \subset [0,T]$ be the discrete set of time-steps and $\Delta t_m = t_m - t_{m-1}$; thus the semi-discretized system reads:

given $(\varphi_0, n_0, F_0, \mathbf{I}_0)$, $\forall m = 1,\dots,M$ find $(\varphi_m, n_m, F_m, \mathbf{I}_m)$ such that:

$$\begin{cases} -\left(\varepsilon\varphi'_m\right)' + q n_m = 0, & \text{in } \Omega, \quad (10.2a) \\ \dfrac{n_m}{\Delta t_m} - \left(\mu_n(n_m) V_{th}\left(\alpha(n_m) n'_m - \dfrac{n_m}{V_{th}}\varphi'_m\right)\right)' - \dfrac{n_{m-1}}{\Delta t_m} = 0, & \text{in } \Omega_{sc}, \quad (10.2b) \\ A\dfrac{\mathbf{F}_m}{\Delta t_m} + \mathbf{C}(\mathbf{F}_m) + r\mathbf{I}_m - A\dfrac{\mathbf{F}_{m-1}}{\Delta t_m} = 0, & \quad (10.2c) \\ I_{m,i} - S\left[\left(\dfrac{D_m - D_{m-1}}{\Delta t_m} + J_{n,m}\right)\nu\right]_i = 0, & \forall i \in \partial\Omega. \quad (10.2d) \end{cases}$$

Given an initial condition (φ_0, n_0) satisfying eqs. (6.7) and (6.8) (for $t = 0$), the boundary conditions are:

$$\begin{cases} \varphi_m(-t_{sc}) - V_{b,m} = \varphi_0(-t_{sc}) - V_{b,0}, \\ \varphi_m(t_{ins}) - V_{g,m} = \varphi_0(t_{ins}) - V_{g,0}, \end{cases} \tag{10.3}$$

and:

$$\begin{cases} n_m(-t_{sc}) = n_0(-t_{sc}), \\ J_{n,m}(0) = J_{n,0}(0). \end{cases} \tag{10.4}$$

10.2 Linearization of the semi-discretized DD system

At each time-step t_m, eq. (10.2) is a system of four non-linear equations for the variables $(\varphi_m, n_m, F_m, \mathbf{I}_m)$, of the form:

$$\begin{bmatrix} G_\varphi(\varphi_m, n_m, F_m, \mathbf{I}_m) \\ G_n(\varphi_m, n_m, F_m, \mathbf{I}_m) \\ G_\mathbf{F}(\varphi_m, n_m, F_m, \mathbf{I}_m) \\ G_\mathbf{I}(\varphi_m, n_m, F_m, \mathbf{I}_m) \end{bmatrix} = \mathbf{0}. \tag{10.5}$$

Equation (10.5) has been linearized by means of a Newton's method, which can be written in compact form:

$$\begin{cases} \begin{bmatrix} G_{\varphi,\varphi} & G_{\varphi,n} & G_{\varphi,\mathbf{F}} & G_{\varphi,\mathbf{I}} \\ G_{n,\varphi} & G_{n,n} & G_{n,\mathbf{F}} & G_{n,\mathbf{I}} \\ G_{\mathbf{F},\varphi} & G_{\mathbf{F},n} & G_{\mathbf{F},\mathbf{F}} & G_{\mathbf{F},\mathbf{I}} \\ G_{\mathbf{I},\varphi} & G_{\mathbf{I},n} & G_{\mathbf{I},\mathbf{F}} & G_{\mathbf{I},\mathbf{I}} \end{bmatrix} \begin{bmatrix} \delta\varphi \\ \delta n \\ \delta\mathbf{F} \\ \delta\mathbf{I}. \end{bmatrix} = - \begin{bmatrix} G_\varphi^{(k)} \\ G_n^{(k)} \\ G_\mathbf{F}^{(k)} \\ G_\mathbf{I}^{(k)} \end{bmatrix}, & (10.6a) \\ \begin{bmatrix} \varphi_m^{(k+1)} \\ n_m^{(k+1)} \\ \mathbf{F}_m^{(k+1)} \\ \mathbf{I}_m^{(k+1)} \end{bmatrix} = \begin{bmatrix} \delta\varphi \\ \delta n \\ \delta\mathbf{F} \\ \delta\mathbf{I} \end{bmatrix} + \tau_k \begin{bmatrix} \varphi_m^{(k)} \\ n_m^{(k)} \\ \mathbf{F}_m^{(k)} \\ \mathbf{I}_m^{(k)} \end{bmatrix}, & (10.6b) \end{cases}$$

for each $k \in \mathbb{N}^+$ until convergence, where $G_{i,j}$ (with $i,j \in \{\varphi, n, \mathbf{F}, \mathbf{I}\}$) denotes the Gâteaux derivative of G_i with respect to the j-th variable at $(\varphi_m^{(k)}, n_m^{(k)}, \mathbf{F}_m^{(k)}, \mathbf{I}_m^{(k)})$ in the direction $[\delta\varphi, \delta n, \delta\mathbf{F}, \delta\mathbf{I}]$. The *damping* factor τ_k is chosen to preserve the positivity of the electron density at each iteration and to avoid too long steps.

Expanding eq. (10.6a) gives:

$$\begin{cases} -\left(\varepsilon\delta\varphi'\right)' + q\delta n = -G_\varphi^{(k)}, & \text{(10.7a)} \\ \dfrac{\delta n}{\Delta t_m} - \left(\mu_n(n_m^{(k)}) V_{th}\left(-\frac{n_m^{(k)\prime}}{V_{th}}\delta\varphi' + \alpha(n_m^{(k)})\delta n' - \beta\delta n\right)\right)' = -G_n^{(k)}, & \text{(10.7b)} \\ \left(\dfrac{A}{\Delta t_m} + B\right)\delta\mathbf{F} + r\delta\mathbf{I} = -G_\mathbf{F}^{(k)}, & \text{(10.7c)} \\ \delta I_{m,i} - S\left\{\left[\left(\frac{D_m - D_{m-1}}{\Delta t_m} + J_{n,m}\right)_{,\varphi}[\delta\varphi] + \right.\right. \\ \left.\left. + \left(\frac{D_m - D_{m-1}}{\Delta t_m} + J_{n,m}\right)_{,n}[\delta n]\right]\nu\right\}_i = -G_\mathbf{I}^{(k)}, & \text{(10.7d)} \end{cases}$$

where $\beta = -\left(\alpha'(n_m^{(k)}) n_m^{(k)\prime} - \frac{\varphi_m^{(k)\prime}}{V_{th}}\right)$ and

$$\alpha'(n(\phi)) = \frac{\mathrm{d}\alpha}{\mathrm{d}n}(n(\phi)) = \frac{1}{V_{th}\frac{\partial n}{\partial\phi}} - \frac{\frac{\partial^2 n}{\partial\phi^2}}{\left(\frac{\partial n}{\partial\phi}\right)^2}\alpha(n(\phi)),$$

ϕ being the chemical potential defined in section 4.3. We remark that the mobility coefficient, computed through the EGDM model as explained in chapter 9, has been handled explicitly; therefore the calculation of its functional derivative is not needed.

At every time-step t_m, a good initial guess $(\varphi_m^{(0)}, n_m^{(0)}, \mathbf{F}_m^{(0)}, \mathbf{I}_m^{(0)})$ for the Newton's method is crucial to guarantee a fast convergence of the linearized problem: it is computed by means of a linear extrapolation from the solutions computed at the two older time-steps.

Given an initial guess $(\varphi_m^{(0)}, n_m^{(0)})$ satisfying eqs. (10.3) and (10.4), the boundary conditions imposed for the linearized system are:

$$\begin{cases} \delta\varphi(-t_{sc}) - \delta V_b = \left(\varphi_m^{(k)}(-t_{sc}) - V_{b,m}^{(k)}\right) - \left(\varphi_0(-t_{sc}) - V_{b,0}\right), \\ \delta\varphi(t_{ins}) - \delta V_g = \left(\varphi_m^{(k)}(t_{ins}) - V_{g,m}^{(k)}\right) - \left(\varphi_0(t_{ins}) - V_{g,0}\right), \end{cases} \tag{10.8}$$

and:

$$\begin{cases} \delta n(-t_{sc}) = n_m^{(k)}(-t_{sc}) - n_0(-t_{sc}), \\ \left[\left(J_{n,m}\right)_{,\varphi}[\delta\varphi] + \left(J_{n,m}\right)_{,n}[\delta n]\right](0) = 0. \end{cases} \tag{10.9}$$

The calculation of the jacobian matrix in eq. (10.6) is a very time- and resource-consuming task. For each step of the Newton's method we choose to fix the same jacobian matrix and thus to perform a number of subsequent **Modified Newton**'s iterations. The coupled method has a worse convergence behavior but allows to reduce the global computational costs of the linearization procedure.

Algorithm 10.1 outlines the general resolution scheme used for the non-linear problem; in particular we remark the implementation of the **time-step adaptation**: the algorithm tries to reduce the time-step if the linearization procedure fails to converge, otherwise the time-step is relaxed in order to save computational costs.

10.2.1 Generalized Gummel method

The initial guess for the Newton's procedure can be refined through the Gummel fixed-point method (see [Gum64]), which may be seen as a globalization strategy for the Newton's method. We now present a generalized version of the classical Gummel decoupling method suitable for organic devices when the EGDM (chapter 5) is considered. We focus on the following system:

$$\begin{cases} -\left(\varepsilon\varphi'\right)' + q\,n(\phi) = 0, & \text{in } \Omega \times [0,T], \quad (10.10a) \\ n(\phi) - \dfrac{N_0}{\sqrt{\pi}} \displaystyle\int_{-\infty}^{+\infty} \dfrac{e^{-\eta^2}}{\left(1+\exp\left(\frac{\sqrt{2}\sigma\eta - q\phi}{k_B T}\right)\right)} \mathrm{d}\eta = 0, & \text{in } \Omega_{sc} \times [0,T], \quad (10.10b) \\ \dfrac{\partial n}{\partial t} - \left(\mu_n(n) V_{th} \left(\alpha(n) n' - \dfrac{n}{V_{th}} \varphi'\right)\right)' = 0, & \text{in } \Omega_{sc} \times [0,T], \quad (10.10c) \\ n = 0, & \text{in } \Omega_{ins} \times [0,T], \quad (10.10d) \end{cases}$$

where eq. (10.10a) is the non-linear Poisson's equation, eq. (10.10b) the equation defining the electrochemical potential $\varphi_n = \varphi - \phi$ (see section 4.3) and eq. (10.10c) the continuity equation. The generalized Gummel method to solve eq. (10.10) is described in alg. 10.2. If we write eq. (10.10b) in the form $\bar{n} - G(\varphi_n) = 0$, by supposing that φ and $\bar{n}$ are given, this equation can be linearized through a Newton's method in order to iteratively compute the electrochemical potential φ_n; the linearized problem requires to solve:

$$\begin{cases} G'(\varphi_n^k)\delta\varphi_n = -(\bar{n} - G(\varphi_n^k)), & (10.11a) \\ \varphi_n^{k+1} = \varphi_n^k + \delta\varphi_n, & (10.11b) \end{cases}$$

for each $k \in \mathbb{N}^+$ until convergence. In the EGDM model the quantity $G'(\varphi_n) = \frac{\partial G}{\partial \varphi_n}(\varphi_n) = -\frac{\partial G}{\partial \phi}(\varphi_n)$ is evaluated through eq. (4.21). Numerical properties of this algorithm has not been deeply studied yet and certainly warrant further research, as in the one-dimensional approximation there is no real advantage to use the Gummel decoupling.

Data: Initial condition $(\varphi_0, n_0, \mathbf{F}_0, \mathbf{I}_0)$
for $m = 1$ **to** M **do**
TIME LOOP
  compute initial guess $(\varphi_m^{(0)}, n_m^{(0)}, \mathbf{F}_m^{(0)}, \mathbf{I}_m^{(0)})$ by extrapolation;
  $k = 0$;
  while $k <= maxIter_N$ *and not converged* **do**
  NEWTON'S LOOP
    update jacobian and compute its *LU* factorization;
    update residual;
    solve and compute $(\varphi_m^{(k+1)}, n_m^{(k+1)}, \mathbf{F}_m^{(k+1)}, \mathbf{I}_m^{(k+1)})$;
    if $increment$ $(or \, \|residual\|) < tolerance$ **then** CONVERGED
      break;
    end
    if *step too long or* $iter_N == maxIter_N$ **then** REJECTED
      break and reduce time-step;
    end
    for $iter_{MN} = 0$ **to** $maxIter_{MN}$ **do**
    MODIFIED NEWTON'S LOOP
      update residual;
      solve and compute new state;
      if $increment$ $(or \, \|residual\|) < tolerance$ **then** CONVERGED
        break;
      end
      if *step too long* **then**
        break;
      end
      if $iter_{MN} == maxIter_{MN}$ **then** REJECTED
        break Newton and reduce time-step;
      end
    end
    if *Modified Newton converged* **then**
      break;
    else if *Modified Newton's step too long* **then**
      reject and revert to $(\varphi_m^{(k+1)}, n_m^{(k+1)}, \mathbf{F}_m^{(k+1)}, \mathbf{I}_m^{(k+1)})$;
    end
  end
  if *Newton or Modified Newton converged* **then**
    relax time-step;
  else REJECTED
    reduce time-step;
  end
end

Algorithm 10.1: General resolution algorithm.

Data: Initial guess $(\varphi_0, \phi_{n,0}, n_0)$
$k = 0$;
while $k <= maxIter$ *and not converged* **do**
  solve eq. (10.10a) for φ_{k+1} using the Newton's method described in section 8.1 started with $\phi^0_{n,k+1} = 0$;
  given φ_{k+1} solve the **linear** eq. (10.10c) for n_{k+1};
  given $\bar{n} = n_{k+1}$ solve eq. (10.10b) for $\phi_{n,k+1}$ using the Newton's method (10.11);
  if $increment < tolerance$ **then** CONVERGED
    break;
  end
end

Algorithm 10.2: Generalized Gummel method.

10.3 Spatial discretization

Accurate and stable numerical solution of the semiconductor equations requires spatial discretization methods that employ upwinding techniques to handle with possible dominant advective phenomena [Boc11; BP11]. In this work we follow an approach based on a finite volume method, particularly a **Scharfetter-Gummel** stabilized **box method** [MW94; BCJC98].

Given a spatial discretization grid $\{z_i\}_{i=1}^n$ with n the number of mesh nodes, the box method requires to construct a *dual mesh*, defined by the boxes $[z_{i-\frac{1}{2}}, z_{i+\frac{1}{2}}]$, where $z_{i+\frac{1}{2}}$ is the middle point of the interval $[z_i, z_{i+1}]$ as shown in fig. 10.1; in particular we assume that the nodes are equally spaced with distance $h = \frac{t_{sc}+t_{ins}}{n-1}$.

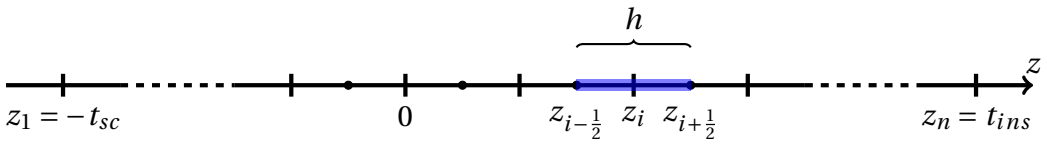

Figure 10.1: Mesh and dual mesh.

Since all the equations presented in the previous sections (such as eqs. (8.2) and (10.7)) belong to this category, we now focus on a general diffusion-advection-reaction problem:

$$J' + c(z)u = 0, \qquad \text{in } \Omega, \tag{10.12}$$

where $J = -a(z)u'(z) + b(z)u(z)$ is the diffusive-advective flux and $c(z)u$ is a reaction

term. Integrating eq. (10.12) over the box $[z_{i-\frac{1}{2}}, z_{i+\frac{1}{2}}]$ yields:

$$J_{i+\frac{1}{2}} - J_{i-\frac{1}{2}} + \int_{z_{i-\frac{1}{2}}}^{z_{i+\frac{1}{2}}} c(z)u(z)\mathrm{d}z = 0, \qquad \text{in } \Omega. \tag{10.13}$$

We now approximate the flux $J(z)$ and the coefficients $a(z), b(z)$ to be constant over each interval $[z_i, z_{i+1}]$ (see [Sha99]), so that:

$$J_{i+\frac{1}{2}} \approx -a_{i+\frac{1}{2}}u' + b_{i+\frac{1}{2}}u,$$

where u is the solution to the following linear ordinary differential equation with constant coefficients:

$$\begin{cases} -a_{i+\frac{1}{2}}u'' + b_{i+\frac{1}{2}}u' = 0, & z \in [z_i, z_{i+1}], \\ u(z_i) = u_i, \\ u(z_{i+1}) = u_{i+1}, \end{cases} \tag{10.14}$$

which gives:

$$u(z) = A + B\exp\left(\lambda_{i+\frac{1}{2}}z\right),$$

with:

$$A = \frac{u_i \exp\left(\lambda_{i+\frac{1}{2}}z_{i+1}\right) - u_{i+1}\exp\left(\lambda_{i+\frac{1}{2}}z_i\right)}{\exp\left(\lambda_{i+\frac{1}{2}}z_{i+1}\right) - \exp\left(\lambda_{i+\frac{1}{2}}z_i\right)} = \frac{u_i \exp\left(\lambda_{i+\frac{1}{2}}h\right) - u_{i+1}}{\exp\left(\lambda_{i+\frac{1}{2}}h\right) - 1},$$

$$B = \frac{u_{i+1} - u_i}{\exp\left(\lambda_{i+\frac{1}{2}}z_{i+1}\right) - \exp\left(\lambda_{i+\frac{1}{2}}z_i\right)},$$

$$\lambda_{i+\frac{1}{2}} = \frac{b_{i+\frac{1}{2}}}{a_{i+\frac{1}{2}}}.$$

The quantity $\lambda_{i+\frac{1}{2}}h$ represents the local Péclet number multiplied by 2. Finally we compute the approximate flux $J_{i+\frac{1}{2}}$:

$$\begin{aligned} J_{i+\frac{1}{2}} &= -a_{i+\frac{1}{2}}u' + b_{i+\frac{1}{2}}u = Ab_{i+\frac{1}{2}} = \\ &= b_{i+\frac{1}{2}}\frac{u_i \exp\left(\lambda_{i+\frac{1}{2}}h\right) - u_{i+1}}{\exp\left(\lambda_{i+\frac{1}{2}}h\right) - 1} = \\ &= \frac{a_{i+\frac{1}{2}}}{h}\lambda_{i+\frac{1}{2}}h\frac{u_i \exp\left(\lambda_{i+\frac{1}{2}}h\right) - u_{i+1}}{\exp\left(\lambda_{i+\frac{1}{2}}h\right) - 1}, \end{aligned}$$

which can be simplified as:

$$J_{i+\frac{1}{2}} = -\frac{a_{i+\frac{1}{2}}}{h}\left[u_{i+1}\mathfrak{B}(\lambda_{i+\frac{1}{2}}h) - u_i\mathfrak{B}(-\lambda_{i+\frac{1}{2}}h)\right], \tag{10.15}$$

where we denoted by $\mathfrak{B}(q) = \frac{q}{\exp(q)-1}$ the Bernoulli function and exploited its property $\mathfrak{B}(-q) = e^q\mathfrak{B}(q)$. The expression of $J_{i-\frac{1}{2}}$ can be analogously derived by exchanging $[z_i, z_{i+1}]$ with $[z_{i-1}, z_i]$:

$$J_{i-\frac{1}{2}} = -\frac{a_{i-\frac{1}{2}}}{h}\left[u_i\mathfrak{B}(\lambda_{i-\frac{1}{2}}h) - u_{i-1}\mathfrak{B}(-\lambda_{i-\frac{1}{2}}h)\right].$$

Remark 10.1. The expression (10.15) corresponds to the difference formula presented by Scharfetter and Gummel in [SG69]. An interesting property of this scheme is that it *automatically* adapts itself to all possible transport regimes: for example, if we assume $b(z) = 0$, i.e. no advective phenomenon is involved ($\lambda = 0$), the formula degenerates in:

$$J_{i+\frac{1}{2}} = -a_{i+\frac{1}{2}}\frac{u_{i+1} - u_i}{h},$$

which is a difference approximation of a **purely diffusive** flow. Conversely, if we assume $b(z) \to +\infty$, i.e. advective phenomena are dominant ($\lambda \to +\infty$), the formula degenerates in:

$$J_{i+\frac{1}{2}} = -\frac{a_{i+\frac{1}{2}}}{h}\left[-u_i \cdot (\lambda_{i+\frac{1}{2}}h)\right] = b_{i+\frac{1}{2}}u_i,$$

while, for $b(z) \to -\infty$:

$$J_{i+\frac{1}{2}} = -\frac{a_{i+\frac{1}{2}}}{h}\left[u_{i+1} \cdot (-\lambda_{i+\frac{1}{2}}h)\right] = b_{i+\frac{1}{2}}u_{i+1};$$

these two expressions correspond to an **upwind** discretization of a **purely advective** flow.

We are now able to approximate $J_{i-\frac{1}{2}}$ and $J_{i+\frac{1}{2}}$ in eq. (10.13); the reaction term $\int_{z_{i-\frac{1}{2}}}^{z_{i+\frac{1}{2}}} c(z)u(z)\mathrm{d}z$ is approximated using the midpoint quadrature rule:

$$\int_{z_{i-\frac{1}{2}}}^{z_{i+\frac{1}{2}}} c(z)u(z)\mathrm{d}z \approx hc_iu_i. \tag{10.16}$$

Expanding eq. (10.13) over all the boxes $[z_{i-\frac{1}{2}}, z_{i+\frac{1}{2}}]$ through the approximations (10.15) and (10.16) finally leads to a linear system in the nodal unknowns $\{u_i\}_{i=1}^n$.

Part IV Numerical results

11 σ extraction

In this chapter we apply the methods described in chapter 8 to extract the DOS width σ of a MIS capacitor. We discuss how the shape of the $C-V$ curve depends on each parameter by performing a sensitivity analysis, then the algorithm introduced in section 8.5 will be used to probe the parameter σ by fitting experimental $C-V$ curves over a discrete range of applied voltages $\mathcal{V} = [V_{g,dep}, V_{g,acc}]$.

11.1 Sensitivity analysis

The simulations are performed by letting a parameter vary and fixing the others; we group them into the following clusters:

1. single gaussian, as σ varies;
2. single gaussian, as N_0 varies;
3. single gaussian, as Φ_B varies;
4. double gaussian, as σ_2 varies (for different values of $N_{0,2}$ and $\varphi_{s,2}$);
5. single and double gaussian, as the temperature T varies.

The reference values for the main simulation parameters are shown in table 11.1; the semiconductor material is the Poly{[N,N'-bis(2-octyldodecyl)-naphthalene-1,4,5,8-bis(dicarboximide)-2,6-diyl]-alt-5,5'-(2,2'-bithiophene)} (P(NDI2OD-T2)), a high mobility electron-type polymer used for printed OTFTs that features a good electron injection from Au metals [Yan+09], while the insulator is made of a Poly(methyl methacrylate) (PMMA) layer.

Parameter	Range	Default value
t_{sc}	–	40.17756 [nm]
t_{ins}	–	534 [nm]
C_{sb}	–	$9.47284 \cdot 10^{-12}$ [F]
S	–	$10^{-7}\left[\mathrm{m}^2\right]$
ε_{sc}	–	2.9 [~]
ε_{ins}	–	2.82 [~]
N_0	$10^{24 \div 28}\left[\mathrm{m}^{-3}\right]$	$10^{27}\left[\mathrm{m}^{-3}\right]$
σ	$1 \div 10.5\,[\mathrm{k_B} \cdot 300\mathrm{K}]$	$3\,[\mathrm{k_B} \cdot 300\mathrm{K}]$
Φ_B	$0 \div -2$ [V]	-1 [V]
$N_{0,2}$	$10^{24 \div 25}\left[\mathrm{m}^{-3}\right]$	$10^{25}\left[\mathrm{m}^{-3}\right]$
σ_2	$4 \div 9.5\,[\mathrm{k_B} \cdot 300\mathrm{K}]$	$5\,[\mathrm{k_B} \cdot 300\mathrm{K}]$
$\varphi_{s,2}$	$-0.1 \div 0.3\,[\mathrm{k_B} \cdot 300\mathrm{K}]$	0.1 [V]
T	$100 \div 350$ [K]	295 [K]

Table 11.1: Values of the main simulation parameters (k is the Boltzmann's constant).

11.1.1 Dependence on σ, N_0 and Φ_B

The sensitivity analysis clearly shows that all the parameters strongly alter the final shape of the $C-V$ curve, whether they directly appear in the mathematical expression of the DOS function (N_0, σ, ...) or not (such as Φ_B); these effects seem to be amplified when looking at the first derivative $\frac{\mathrm{d}C}{\mathrm{d}V_g}$. In this section we analyze the dependence on three main parameters, which are the disorder parameter σ, the total density of states N_0 and the barrier Φ_B.

The most significant influence seems to be induced by the **disorder parameter** σ, as shown in fig. 11.1: the first noticeable effect is that the functional dependence of C on V_g becomes less steep as the disorder increases (the capacitance is less influenced by variations of the applied voltage); moreover the curve experiences a shift towards more negative values of V_g [Mad+15]. This effect may be understood by considering that, since the Fermi level is closer (as σ increases) to the energy regions where the DOS is sizable, a smaller gate voltage is needed to accumulate charges in the semiconductor, as discussed in chapter 7.

An opposite role is played by the total **density of** available **states** N_0 (see fig. 11.2), though it has a weaker influence on the final shape of the $C-V$ curve: a variation of 4 orders of magnitude is needed in order to produce a noticeable effect. We remark

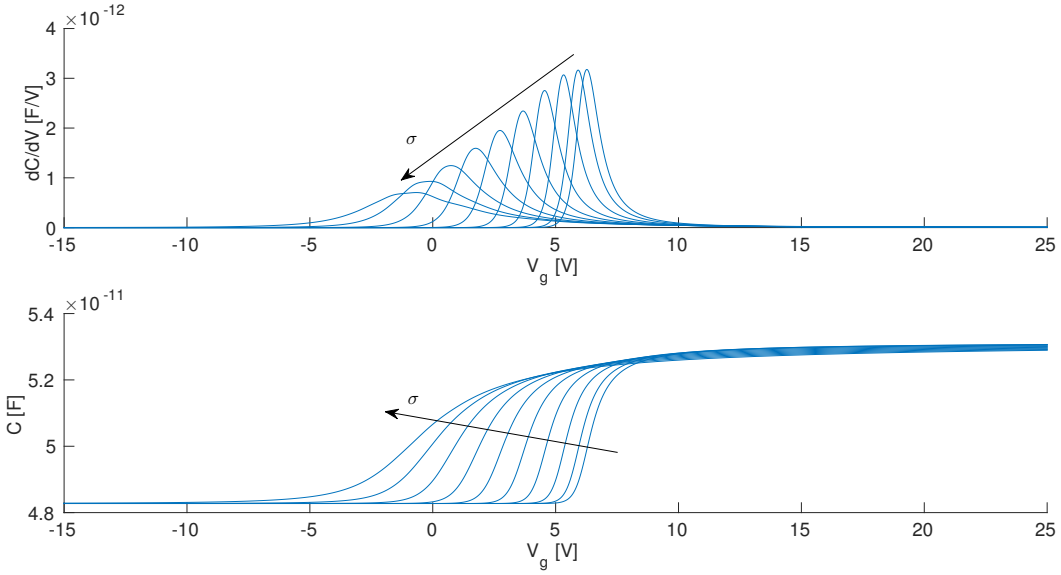

Figure 11.1: Simulation 1: $N_0 = 10^{27}\,[\mathrm{m}^{-3}]$, $\sigma = 1 \div 10.5\,[\mathrm{k_B} \cdot 300\mathrm{K}]$.

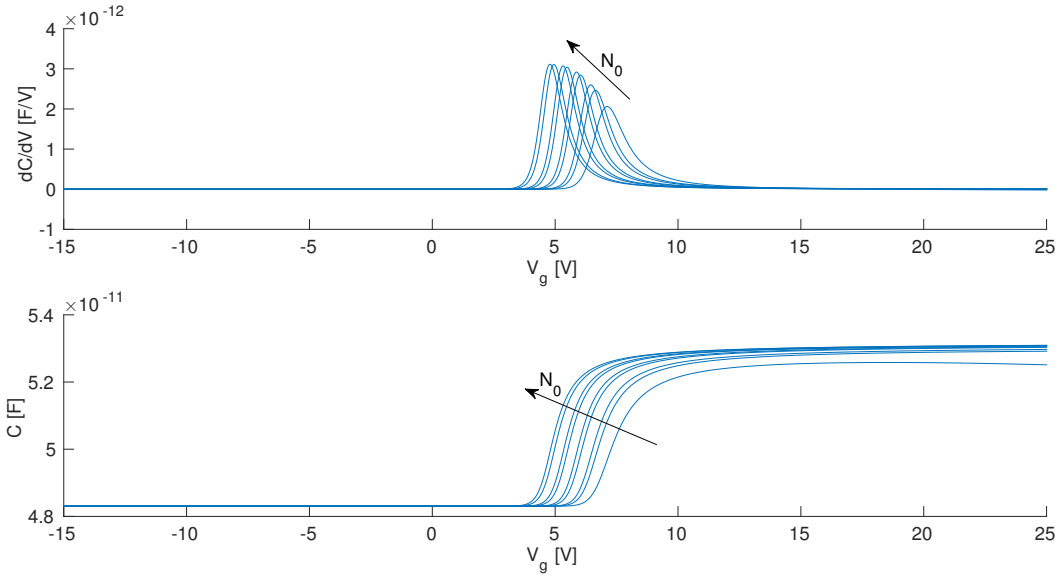

Figure 11.2: Simulation 2: $N_0 = 10^{24} \div 10^{28}$, $\sigma = 3$.

that for very low values of N_0 the $C-V$ curve decreases for high applied voltages. This behavior has never been noticed in experimental measurements, thus setting a lower limit to the value of N_0. We assume $N_0 = 10^{27}\,[\mathrm{m}^{-3}]$, a value commonly accepted in the literature as a valid estimation for organic semiconductors.

The **barrier** potential Φ_B has been assumed equal to $-1\,[\mathrm{V}]$ considering the Au work function $(5\,[\mathrm{eV}])$ and the electron affinity of P(NDI2OD-T2) $(4\,[\mathrm{eV}])$; the sensitivity analysis, shown in fig. 11.3, reveals that large barriers, in modulus, result in an

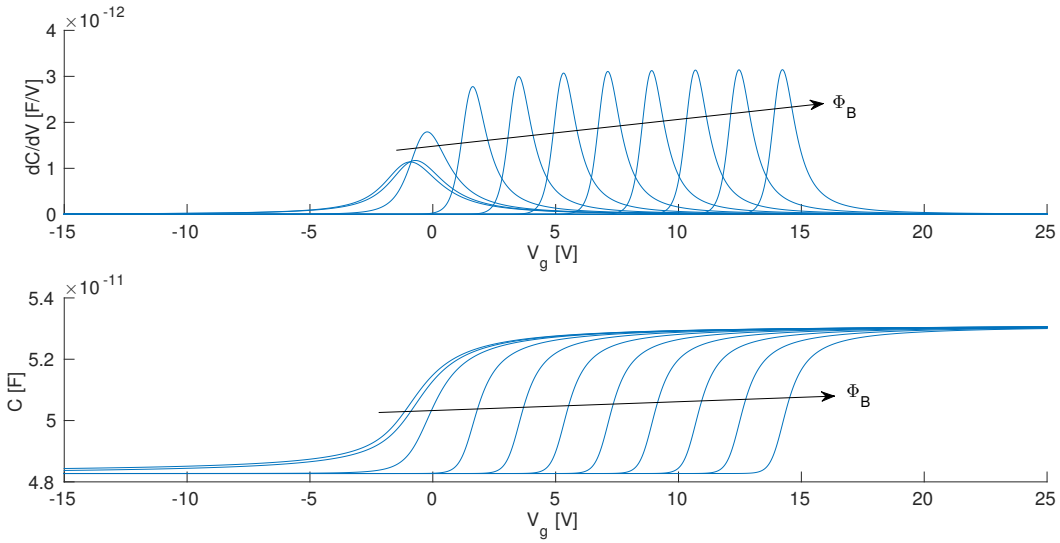

Figure 11.3: Simulation 3: $N_0 = 10^{27}$, $\sigma = 3$, $\Phi_B = 0 \div -2$ [V].

almost rigid shift of the $C-V$ curve, due to the fact that the smaller the barrier the closer the Fermi level is to the DOS (see fig. 7.1) and the easier is to drive the device into accumulation. Conversely, for smaller values of Φ_B the $C-V$ shape becomes smoother and the depletion capacitance starts growing; in fact, a lower barrier determines an higher carrier density at the metal-semiconductor interface which interferes with the gate attraction of the center of charge towards the semiconductor-insulator interface. These results clearly show that Φ_B can have a large influence on $C-V$ curves shape. Since its value is difficult to predict, an adequate fitting algorithm has to be developed in order to extract Φ_B. A promising approach comes from unsteady simulations, as discussed in chapter 13.

11.1.2 Dependence on σ_2

Also in the case of a **double gaussian** DOS shape we can draw similar conclusions, as the parameters σ_2 and $N_{0,2}$ play the same roles as σ and N_0 respectively.

Double gaussian for different values of $N_{0,2}$; $\varphi_{s,2}$ fixed

Figures 11.4 and 11.5 show how the $C-V$ curve is altered as σ_2 varies for two different values of the shift potential $N_{0,2}$. In particular we observe that larger values of σ_2 tend to produce a second peak in the $\frac{dC}{dV_g}$ curve.

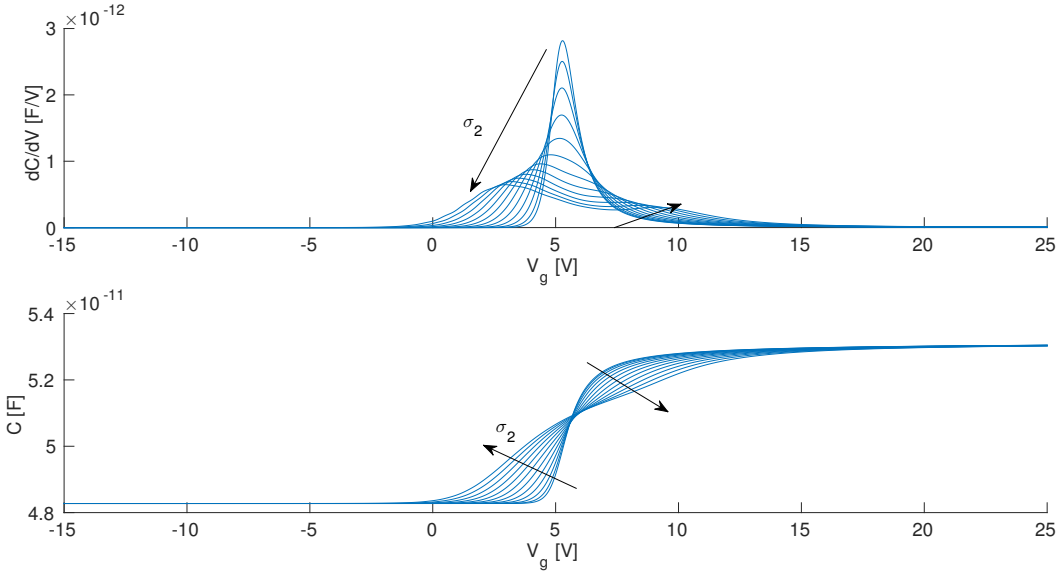

Figure 11.4: Simulation 4.1: $N_0 = 10^{27}$, $\sigma = 3$, $N_{0,2} = 10^{24}$, $\sigma_2 = 4 \div 9.5$, $\varphi_{s,2} = 0.1V$.

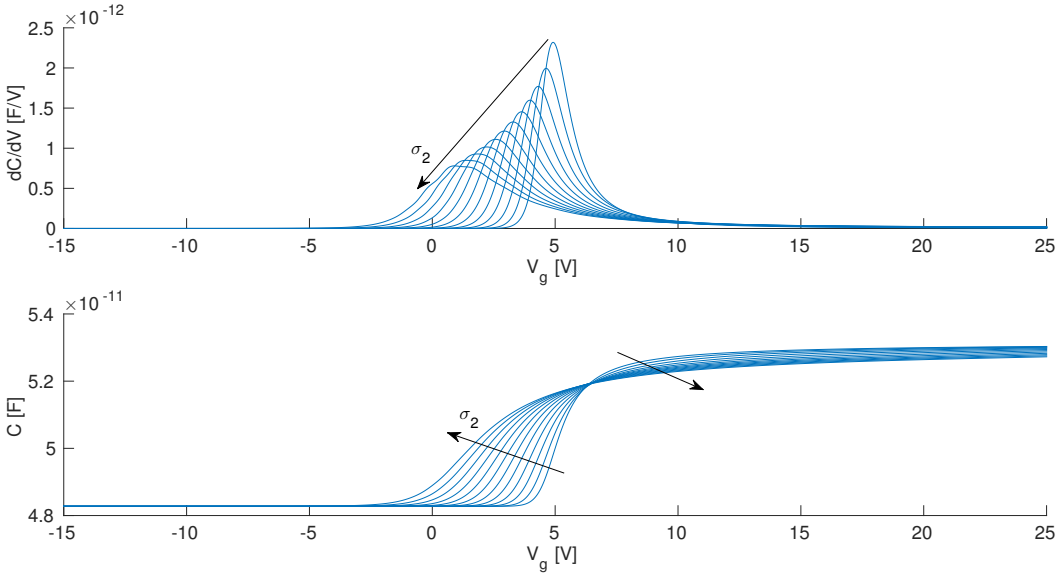

Figure 11.5: Simulation 4.2: $N_0 = 10^{27}$, $\sigma = 3$, $N_{0,2} = 10^{25}$, $\sigma_2 = 4 \div 9.5$, $\varphi_{s,2} = 0.1$.

Double gaussian for different values of $\varphi_{s,2}$; $N_{0,2}$ fixed

Figures 11.6 and 11.9 show the $C-V$ curve for a fixed $N_{0,2}$ and four different values of $\varphi_{s,2}$, which provide analogous results.

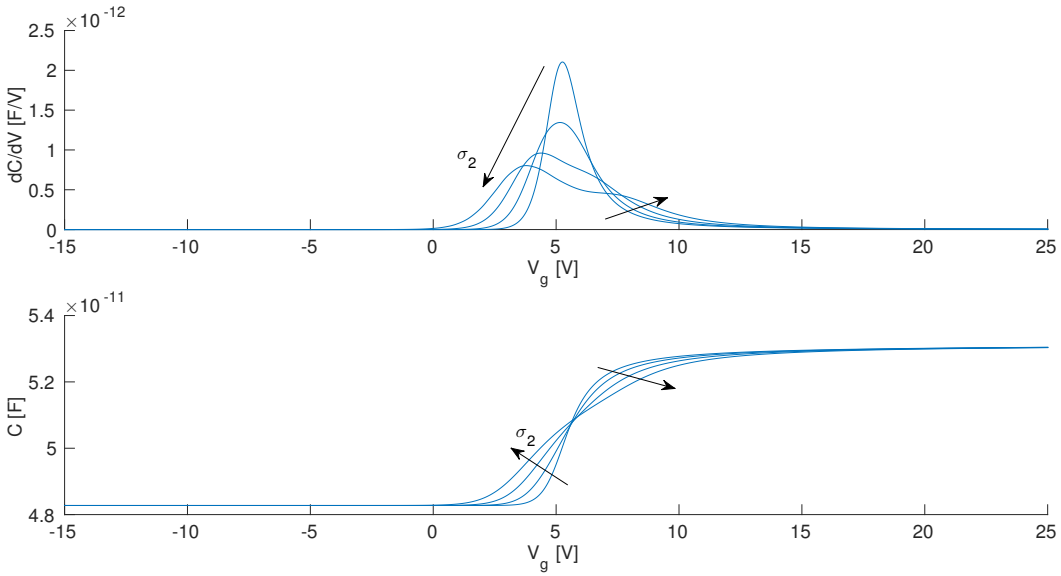

Figure 11.6: Simulation 4.3: $N_0 = 10^{27}$, $\sigma = 3$, $N_{0,2} = 10^{24}$, $\sigma_2 = 5 \div 8$, $\varphi_{s,2} = -0.1$.

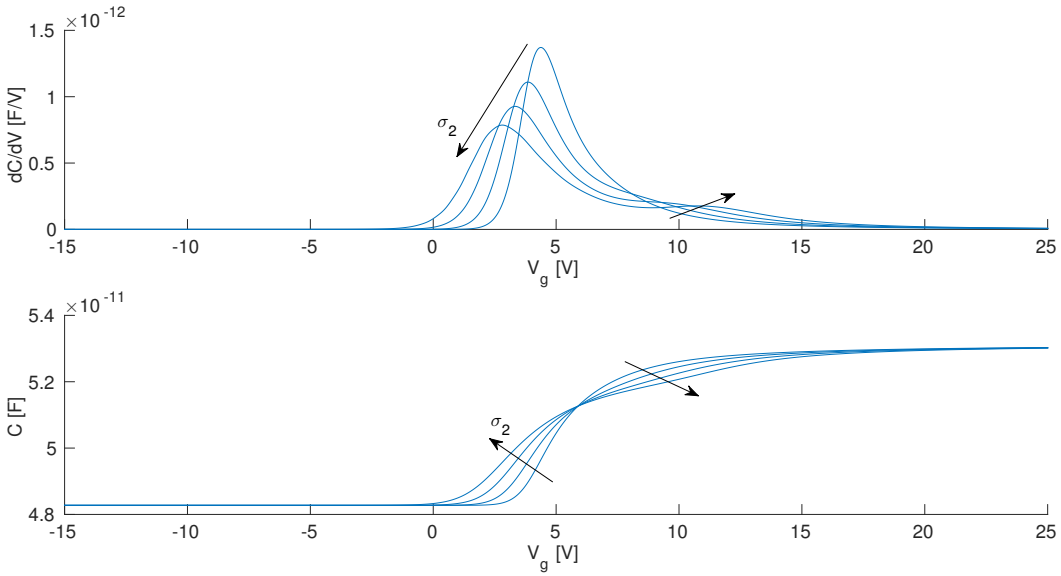

Figure 11.7: Simulation 4.4: $N_0 = 10^{27}$, $\sigma = 3$, $N_{0,2} = 10^{24}$, $\sigma_2 = 5 \div 8$, $\varphi_{s,2} = 0.1$.

We can conclude by remarking that experimental $C-V$ measurements sometimes corresponded to these typical double gaussian shapes, but they always showed an

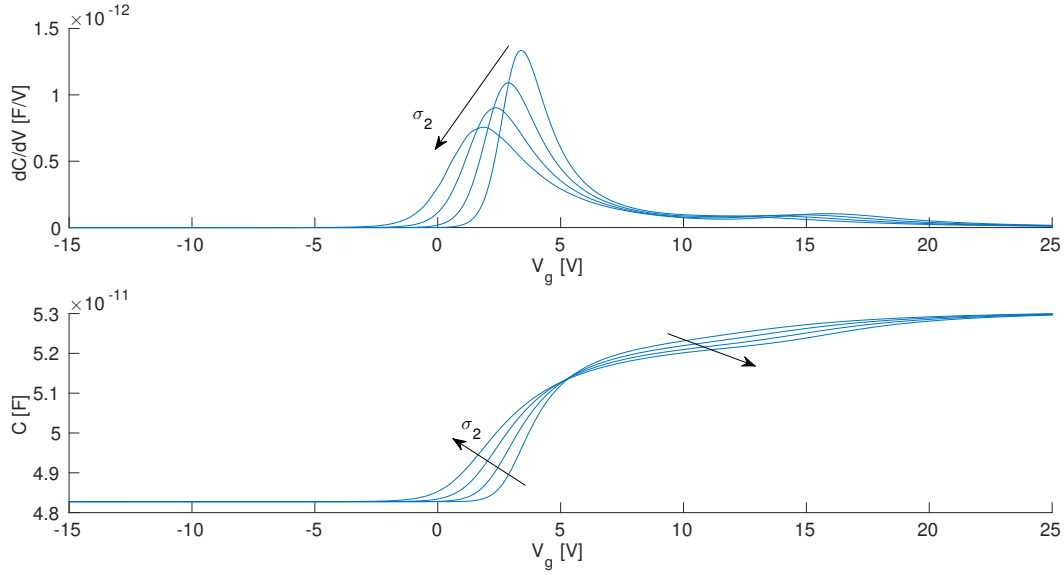

Figure 11.8: Simulation 4.5: $N_0 = 10^{27}$, $\sigma = 3$, $N_{0,2} = 10^{24}$, $\sigma_2 = 5 \div 8$, $\varphi_{s,2} = 0.2$.

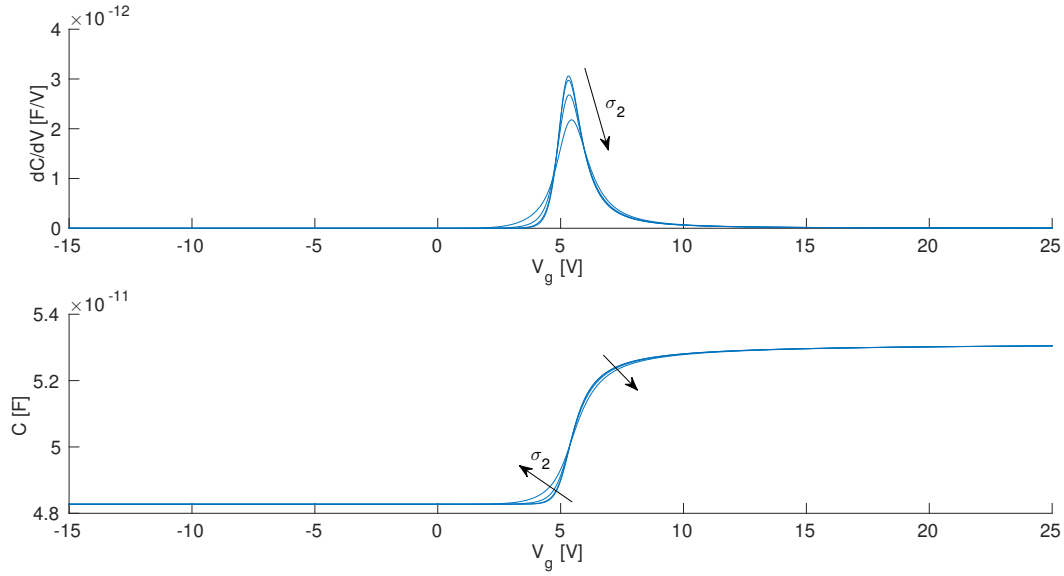

Figure 11.9: Simulation 4.6: $N_0 = 10^{27}$, $\sigma = 3$, $N_{0,2} = 10^{24}$, $\sigma_2 = 5 \div 8$, $\varphi_{s,2} = 0.3$.

instability with time leading to crucial difficulties in studying the behavior of the device.

11.1.3 Dependence on the temperature

In this section we analyze the sensitivity of the $C-V$ curve on the system temperature T. The dependence on the **temperature** T, shown for a single gaussian DOS in fig. 11.10 and for a double gaussian DOS in figs. 11.11 and 11.12) reflects the Fermi-Dirac statistics (see section 4.2.3): as T becomes larger the charge density and the capacitance grow with a slope dependent on the particular DOS shape considered.

Single Gaussian

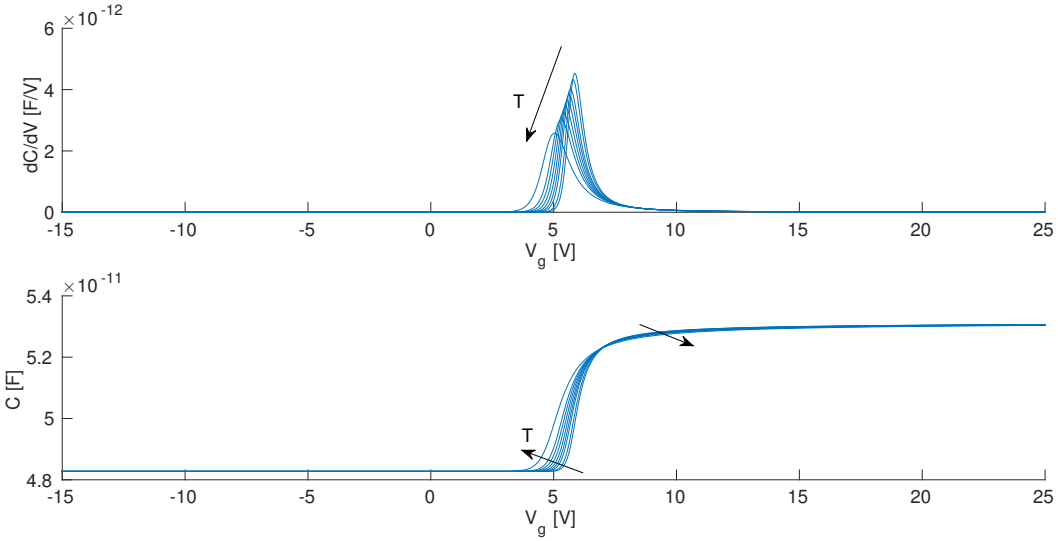

Figure 11.10: Simulation 5.1: $N_0 = 10^{27}$, $\sigma = 3$, $T = 100 \div 350$ [K].

Double gaussian for different values of $N_{0,2}$; $\varphi_{s,2}$ fixed

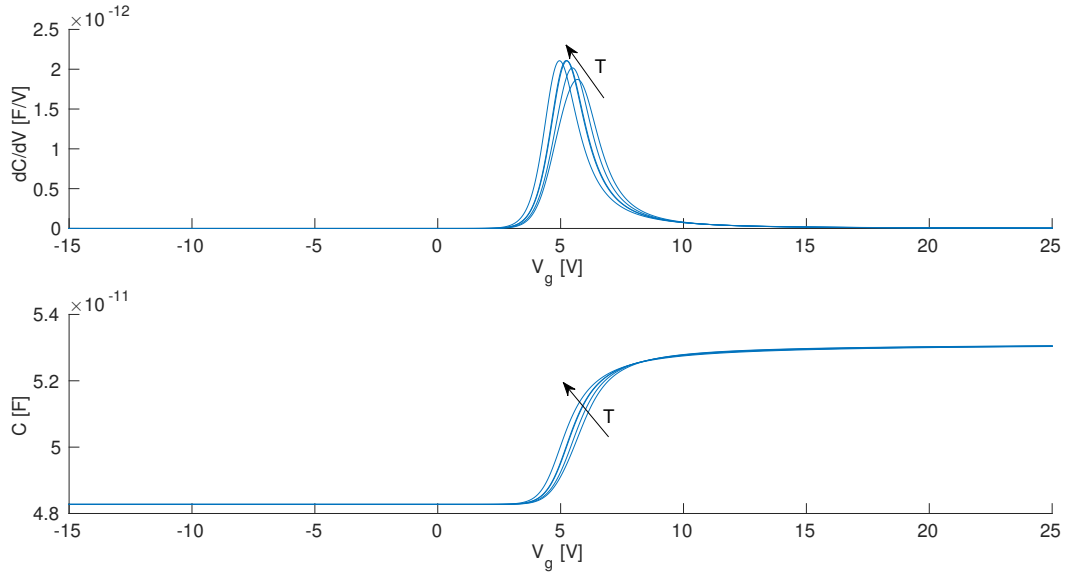

Figure 11.11: Simulation 5.2: $N_{0,2} = 10^{25}$, $\sigma_2 = 5$, $\varphi_{s,2} = 0.1$, $T = 200 \div 350$.

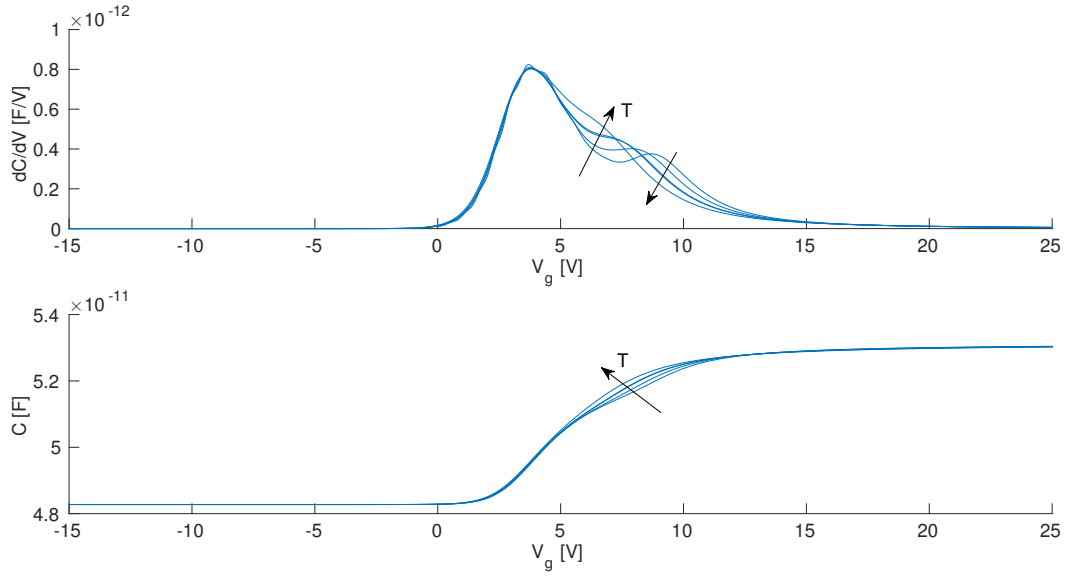

Figure 11.12: Simulation 5.3: $N_{0,2} = 10^{25}$, $\sigma_2 = 8$, $\varphi_{s,2} = 0.1$, $T = 200 \div 350$.

11.2 Automatic fitting

The algorithm described in section 8.5 has been applied to extract the DOS width σ. We now list the results obtained throughout the fitting procedure by minimiz-

ing the distance between experimental and simulated $C-V$ curves in terms of L^2-error, H^1-error and peak-error. The algorithm is initialized from the following guess: $\sigma^{(0)} = 3\,[\mathrm{k_B}\cdot 300\mathrm{K}]$, $t_{sc}^{(0)} = 4.017756\cdot 10^{-8}\,[\mathrm{m}]$, $C_{sb}^{(0)} = 9.47284\cdot 10^{-12}\,[\mathrm{F}]$, motivated by experimental measurements, though subject to uncertainties. We found that the minimization of the peak-distance provided the best results, thus we omit the results obtained by the minimization of L^2- and H^1-errors.

11.2.1 Peak-error

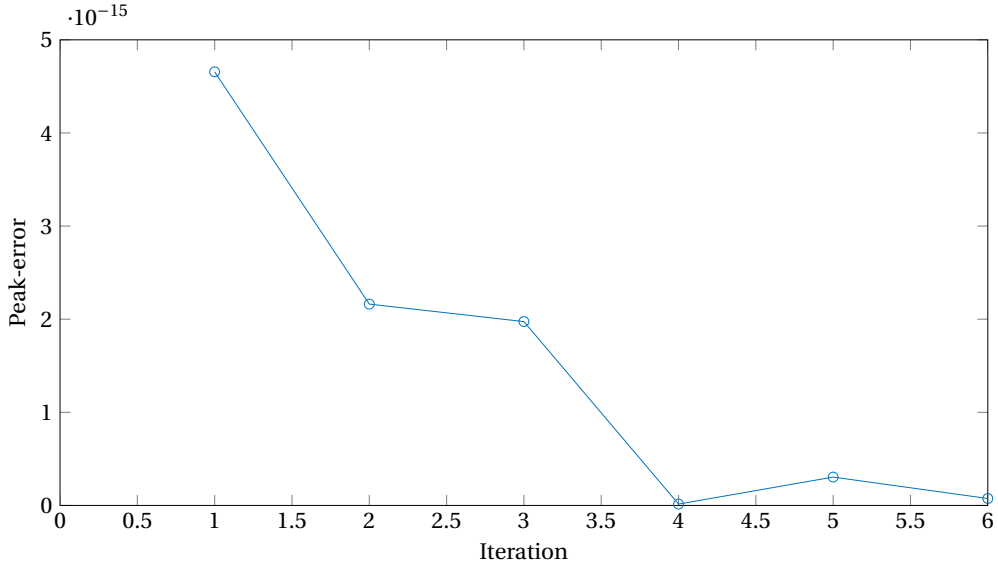

Figure 11.13: Peak-error throughout the fitting procedure.

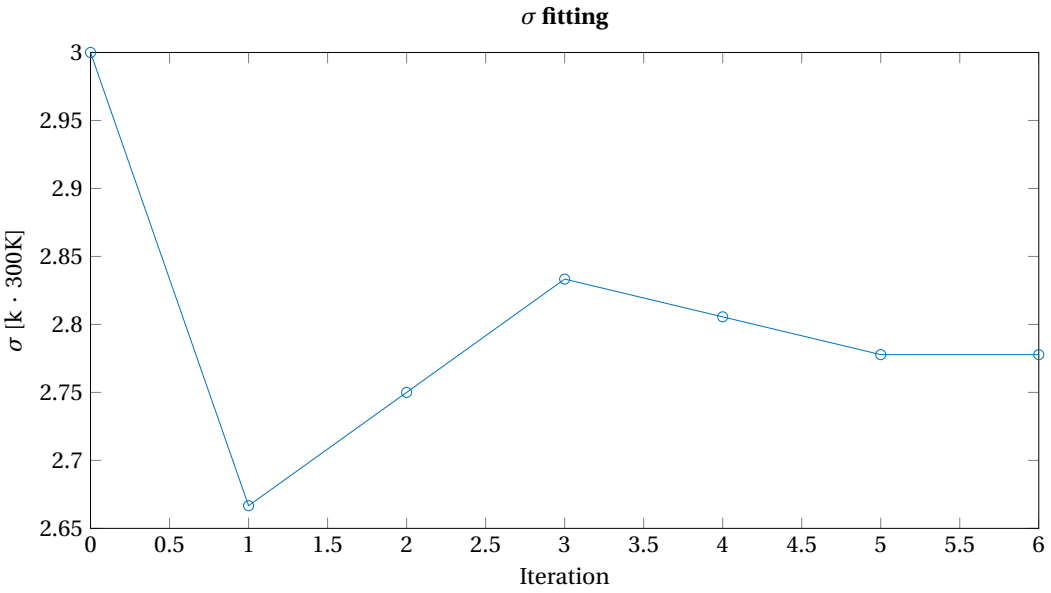

Figure 11.14: Peak-error minimization: values of σ throughout the fitting procedure.

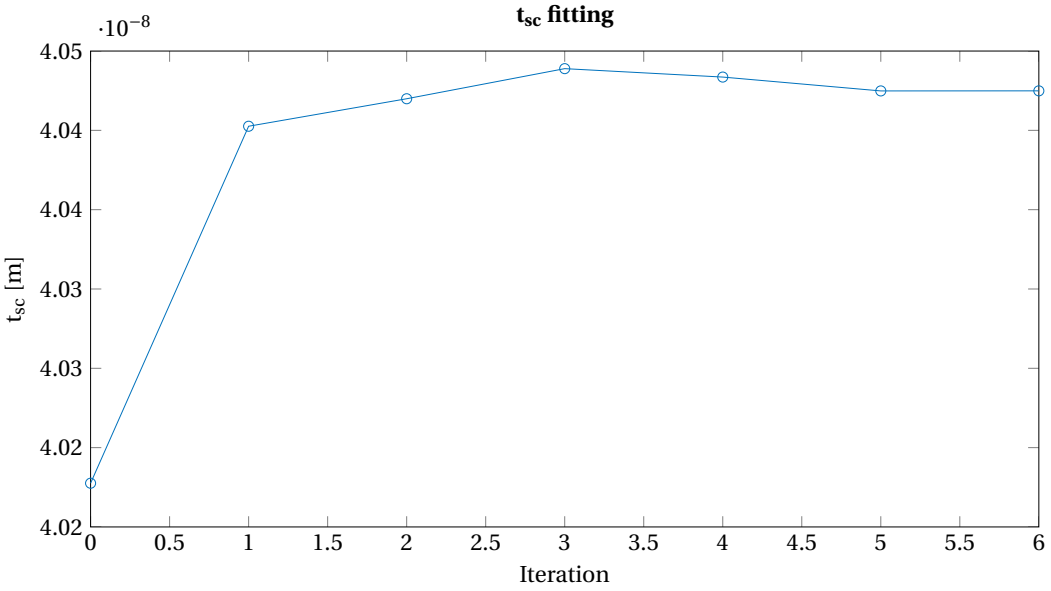

Figure 11.15: Peak-error minimization: values of t_{sc} throughout the fitting procedure.

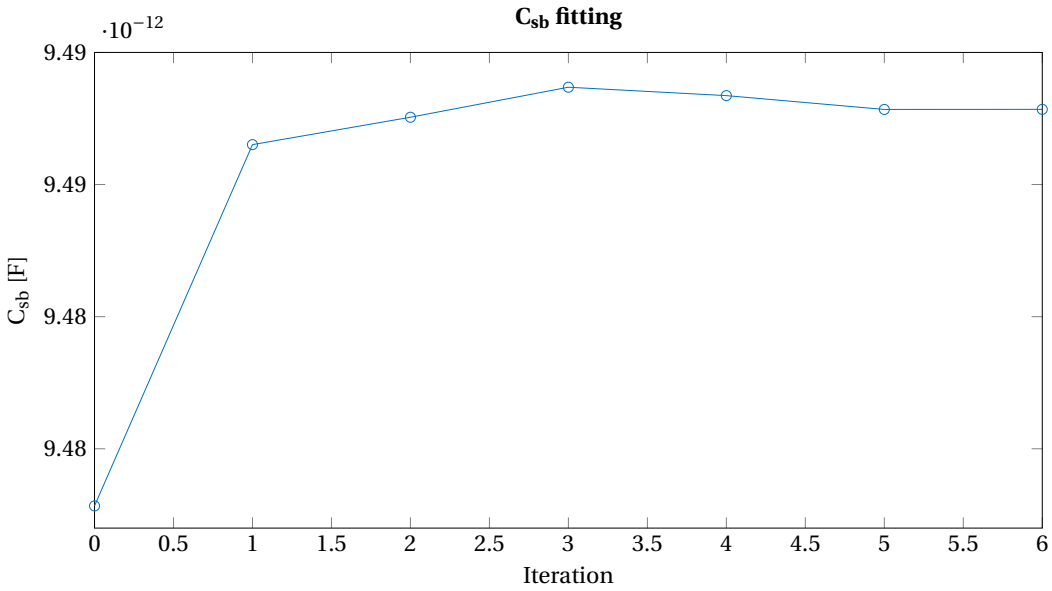

Figure 11.16: Peak-error minimization: values of C_{sb} throughout the fitting procedure.

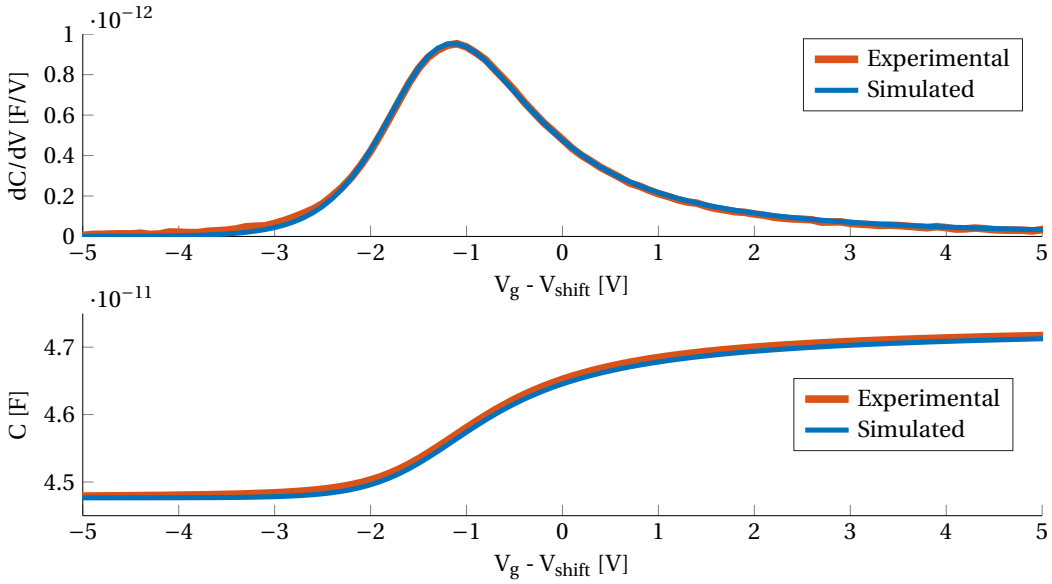

Figure 11.17: Peak-error minimization: comparison between experimental and optimal simulated curves.

11.2.2 Conclusions

We appreciate that the approach based on a single gaussian DOS provides very accurate results, as fig. 11.17 show a very satisfactory match between experimental and simulated data.

Table 11.2 shows the summary of the results obtained for the error (see fig. 11.13), σ (fig. 11.14), t_{sc} (fig. 11.15) and C_{sb} (fig. 11.16) throughout the fitting algorithm.

Iteration	Peak-error	σ	t_{sc}	C_{sb}
1	$4.656 \cdot 10^{-15}$	$2.\bar{6}$	$4.040 \cdot 10^{-08}$	$9.486 \cdot 10^{-12}$
2	$2.162 \cdot 10^{-15}$	2.75	$4.042 \cdot 10^{-08}$	$9.488 \cdot 10^{-12}$
3	$1.974 \cdot 10^{-15}$	$2.8\bar{3}$	$4.044 \cdot 10^{-08}$	$9.489 \cdot 10^{-12}$
4	$1.446 \cdot 10^{-17}$	$2.80\bar{5}$	$4.043 \cdot 10^{-08}$	$9.488 \cdot 10^{-12}$
5	$3.046 \cdot 10^{-16}$	$2.\bar{7}$	$4.042 \cdot 10^{-08}$	$9.488 \cdot 10^{-12}$
6	$7.456 \cdot 10^{-17}$	$\mathbf{2.\bar{7}}$	$\mathbf{4.042 \cdot 10^{-08}}$	$\mathbf{9.488 \cdot 10^{-12}}$

Table 11.2: Peak-error minimization: summary of the results.

The DOS width $\sigma = 2.\bar{7}\,[k_B \cdot 300K]$ extracted by the peak-error minimization is acceptable and is very similar to the value extracted by manually comparing the $C-V$ curves, equal to $2.8\,[k_B \cdot 300K]$. This value will be used in chapter 12 for probing the low-field and low-charge-density $\mu_{0,n}$, thus showing that $\sigma = 2.\bar{7}\,[k_B \cdot 300K]$ is a meaningful measurement. The simulated $C-V$ curve has been shifted by $V_{shift} = 10.6\overline{495}$ [V] with respect to the experimental one.

12 μ_0 extraction

Knowing the disorder parameter $\sigma = 2.\bar{7}\,[k_B \cdot 300K]$ of the semiconductor (see section 11.2.2), we can now fit experimental and simulated $I-V$ curves in order to extract the low-field and low-charge-density mobility $\mu_{0,n}$ of the EGDM model (5.1), as explained in chapter 9. We focus on an OTFT device with an aspect ratio:

$$\frac{W}{L} = \frac{10^{-2}\,[\mathrm{m}]}{10^{-5}\,[\mathrm{m}]} = 1000,$$

with an applied drain-to-source voltage $V_{DS} = 5\,[\mathrm{V}]$. The least squares solution of eq. (9.4) provides the followings electron mobility multiplicative coefficient:

$$\mu_{0,n} \approx 0.0834\left[\mathrm{cm^2V^{-1}s^{-1}}\right]. \tag{12.1}$$

The fitting procedure result in a very good match between experimental and simulated $I-V$ curves, as shown in fig. 12.1, and the fit becomes more accurate upon the channel formation (as V_g grows).

The effective mobility $\mu_{n,\mathrm{eff}}$ computed from the compact model (9.5) and the EGDM model (5.1) is compared in fig. 12.2, showing that the former is quite inaccurate and provides a too simplified way to compute the mobility in correspondence of negative V_g values. In particular the effective mobility computed from the EGDM model tends, as V_g becomes more negative, to the low-field mobility (12.1), while $\mu_{n,\mathrm{eff}}$ from the compact model tends to vanish.

Finally, figs. 12.3 and 12.4 show that the enhancement factor g_1 of the EGDM model (5.1) starts growing for $V_g \sim 0\,[\mathrm{V}]$ and, since the carrier density increases from $z = -t_{sc}$ to $z = 0$ as V_g grows, it becomes more relevant upon the channel formation and near the semiconductor-insulator interface. Thus we conclude by remarking that, for high applied voltages, the mobility varies by a factor ≈ 2.5 from the bulk contact to the semiconductor-insulator interface, which is why the complete EGDM model is needed in order to accurately estimate a space- and voltage-dependent mobility

coefficient.

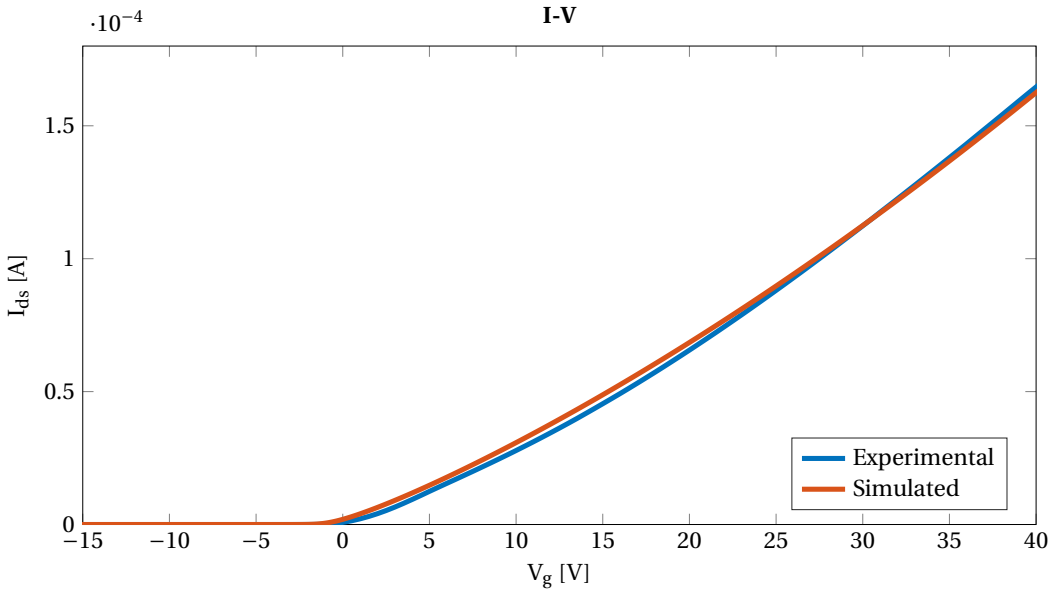

(a) Linear scale.

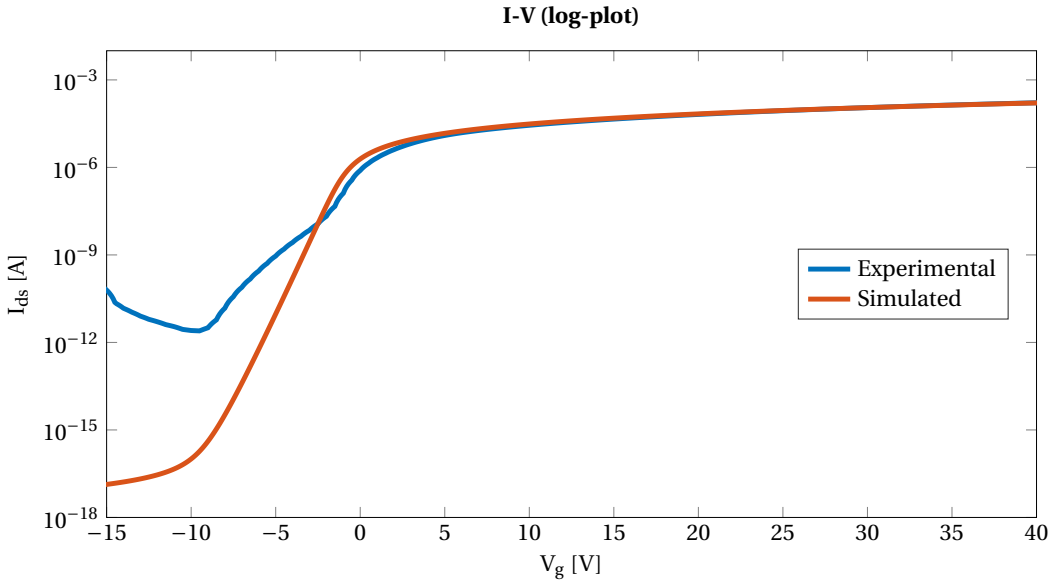

(b) Logarithmic scale.

Figure 12.1: Comparison between experimental and simulated $I-V$ characteristics.

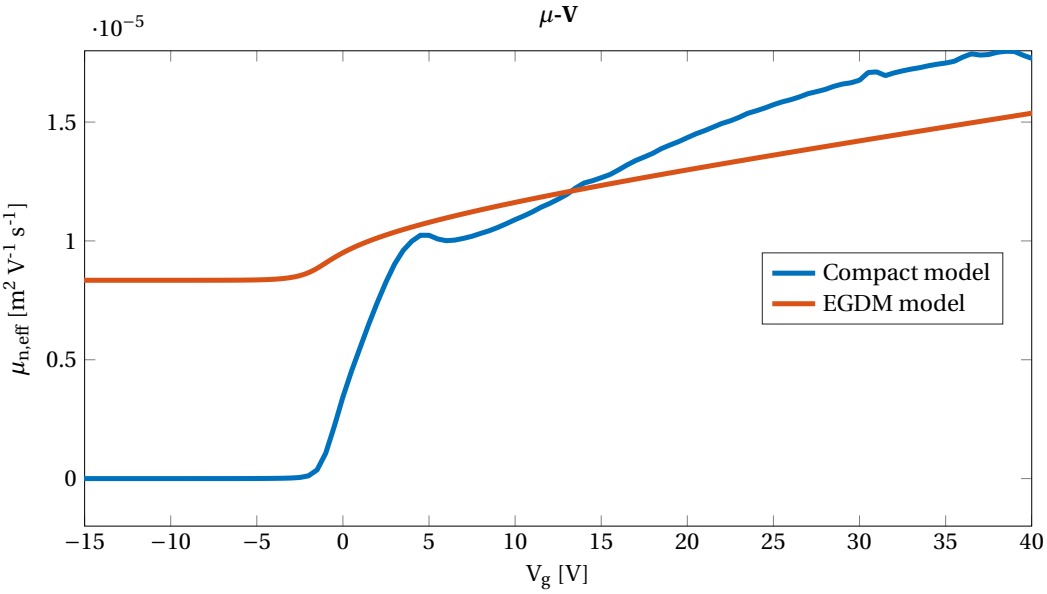

(a) Linear scale.

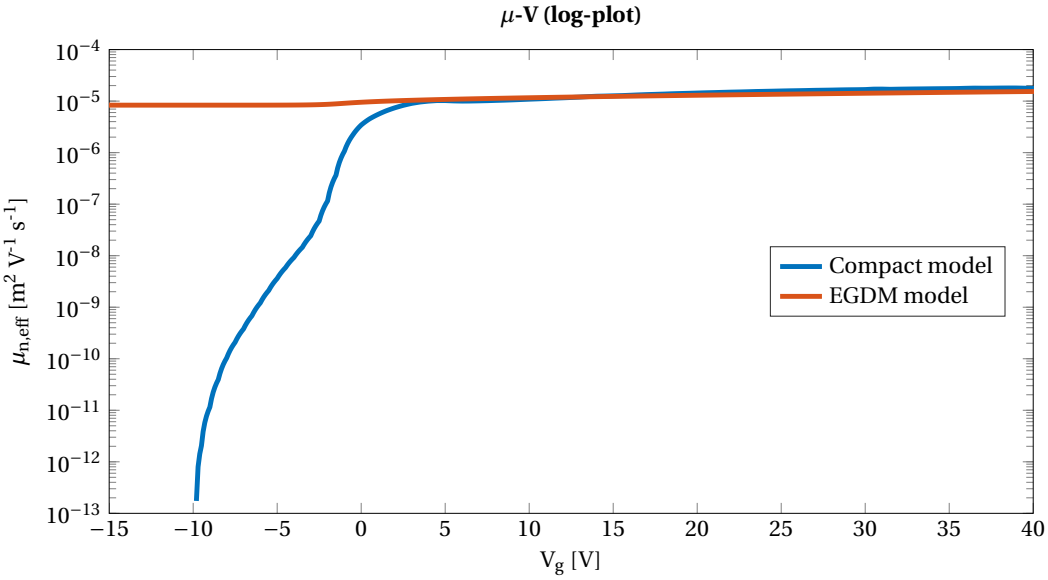

(b) Logarithmic scale.

Figure 12.2: Comparison between $\mu - V$ curves computed from the compact model (9.5) and from the EGDM model (5.1).

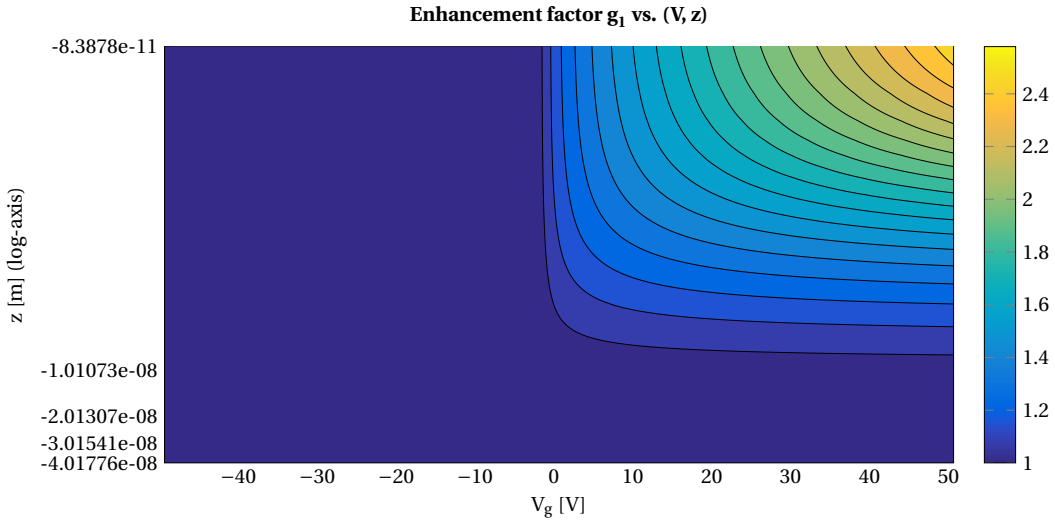

Figure 12.3: Space- and voltage-dependence of the EGDM enhancement factor g_1 in the semiconductor region.

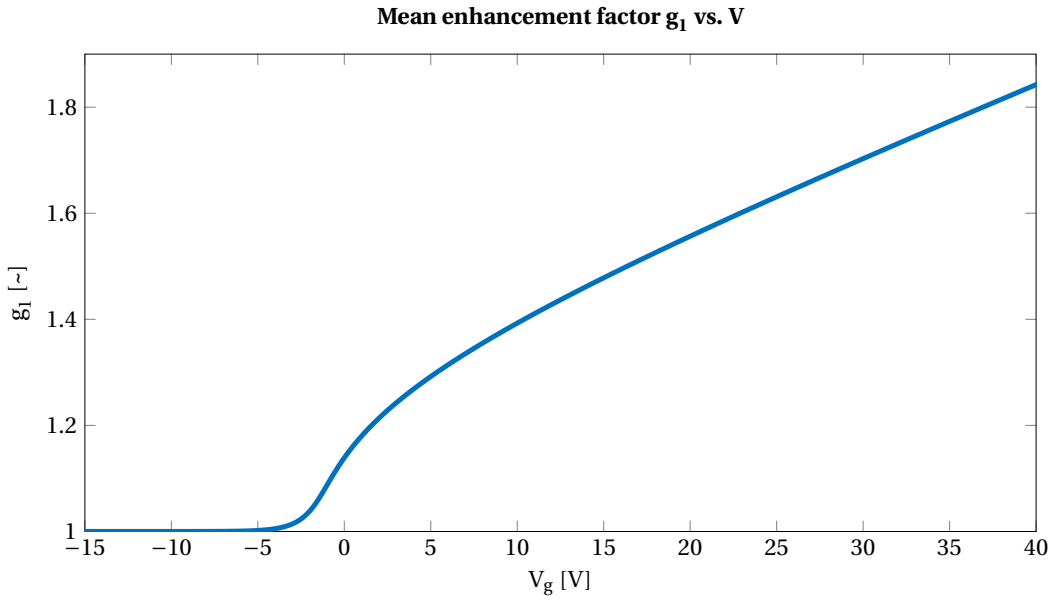

Figure 12.4: Mean of the EGDM enhancement factor g_1, weighted on the electron density n, vs. the applied voltage V_g.

13 Unsteady simulations

Numerical methods discussed in chapter 10 have been used to simulate the behavior of the circuit represented in fig. 13.1 when applying a step input and a sinusoidal signal. From the results computed we are able to:

- estimate the time constant of the step response (section 13.1);
- compute the $C-V$ curve (section 13.2) by emulating the operation of typical measuring instruments, i.e. by fitting the equivalent capacitance C of the series RC circuit represented in fig. 13.2, where $V_G(t)$ and $I(t)$ are the solution of circuit 13.1.

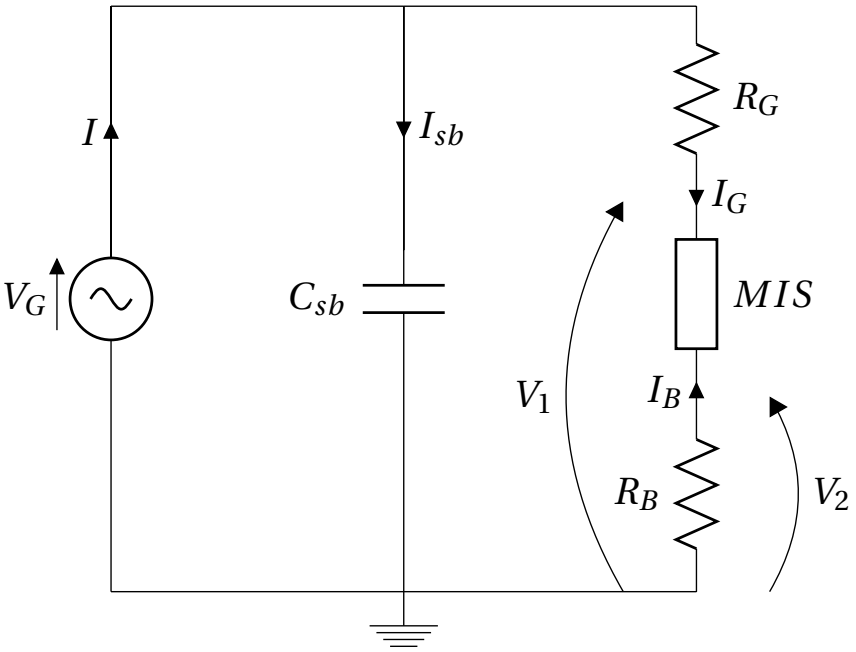

Figure 13.1: External control circuit

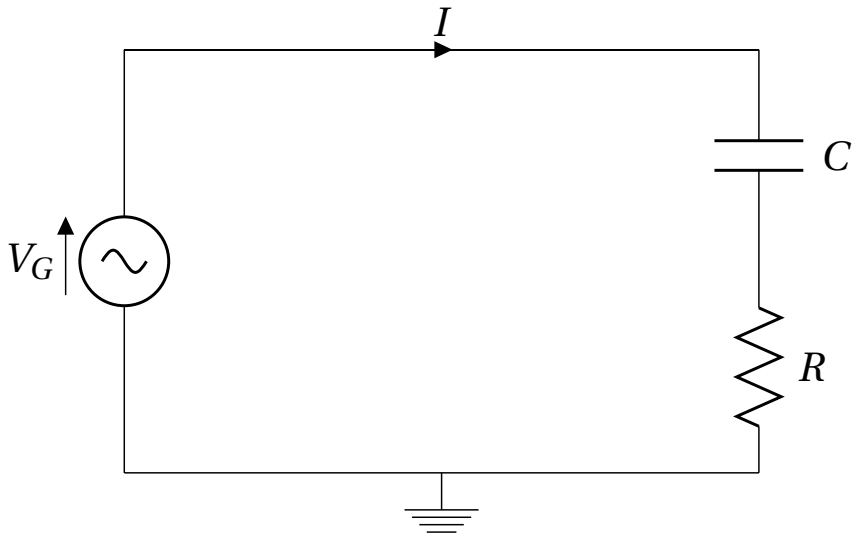

Figure 13.2: Equivalent circuit

The results obtained, shown in sections 13.3 and 13.4, warn that the constant-barrier model given by eq. (6.4) is no longer valid in the unsteady regime and needs to be corrected by considering a field-dependent injection barrier.

Let $\mathbf{F} = [V_1, V_2, Q_{sb}, I]^T$ be the state vector of the circuit 13.1, where Q_{sb} is the accumulated charge in the capacitor C_{sb}. The MNA corresponds to the following system of equations:

$$\begin{cases} I_{sb} - I + I_G = 0, \\ V_1 - V_G + R_G I_G = 0, \\ V_2 + R_B I_B = 0, \\ Q_{sb} - C_{sb} V_G = 0, \end{cases} \tag{13.1}$$

where $I_{sb} = \dot{Q}_{sb}$. Then eq. (6.6) is represented by the following variables:

$$A = \begin{bmatrix} 0 & 0 & 1 & 0 \\ 0 & 0 & 0 & 0 \\ 0 & 0 & 0 & 0 \\ 0 & 0 & 0 & 0 \end{bmatrix},$$

$$B = \begin{bmatrix} 0 & 0 & 0 & -1 \\ 1 & 0 & 0 & 0 \\ 0 & 1 & 0 & 0 \\ 0 & 0 & 1 & 0 \end{bmatrix}$$

$$s = -V_G \begin{bmatrix} 0 \\ 1 \\ 0 \\ C_{sb} \end{bmatrix},$$

$$\mathbf{I} = \begin{bmatrix} I_G \\ I_B \end{bmatrix}.$$

13.1 Step response

We simulate the step response when the device is brought from the depletion to the accumulation regime, i.e. through the step input:

$$V_G(t) = \begin{cases} -10\,[\mathrm{V}], & t < 0, \\ +20\,[\mathrm{V}], & t \geq 0. \end{cases}$$

We suppose that the step response of circuit 13.1 (where, for the sake of simplicity, we set $C_{sb} = R_B = 0$, while $R_G = 10\,[\Omega]$ is the resistance of the generator) is an exponential decay:

$$I(t) = I_0 \exp\left(-\frac{t}{\tau}\right). \tag{13.2}$$

The time constant τ of such a circuit can be qualitatively computed through a simplified theoretical model by dividing the distance traveled by electrons through the MIS semiconductor layer by their mean velocity:

$$\tau_{tr} = \frac{t_{sc}}{\bar{\mu}\frac{\bar{V}_{sc}}{t_{sc}}}, \tag{13.3}$$

where t_{sc} is the thickness of the semiconductor layer; here $\bar{\mu}$ (the mean mobility coefficient) and $\bar{V}_{sc}$ (the mean voltage dropping across the semiconductor region) are computed starting from the numerical solution. The value of τ_{sc} is compared to the time constant τ_n implicitly defined by eq. (13.2):

$$\tau_n = \tau = \arg\min_{t \geq 0} \left(I(t) - I_0 \exp(-1) \right), \tag{13.4}$$

where $I(t)$ and I_0 are computed starting from the numerical solution.

The order of magnitude of the time constant is about 0.1 [ns]; the circuit is simulated for a much longer time ($t \leq 0.1$ [ms]), thus making sure that the system dynamics is fully detected.

13.2 Alternating regime

In order to compute the $C-V$ curve, we simulate circuit 13.1 by applying sinusoidal voltages of the form:

$$V_G(t) = \begin{cases} \widehat{V}, & t \in [-5, 0), \\ \widehat{V} + V_0 \sin(\omega t), & t \geq 0, \end{cases} \tag{13.5}$$

as shown in fig. 13.3, where $\widehat{V}$ varies over a discrete range between -5 [V] (depletion) and $+15$ [V] (accumulation), $\omega = 2\pi\mathfrak{f}$ is the pulsatance and $\mathfrak{f} \approx 9283.18$ [Hz] is the signal frequency. The amplitude V_0 is set equal to 0.1 [V].

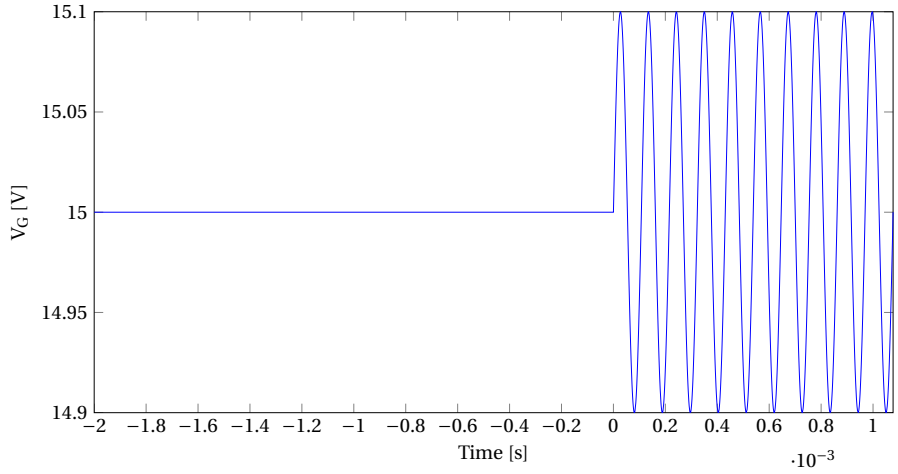

Figure 13.3: Alternating regime: example of applied voltage ($\widehat{V} = 15$ [V]).

We emulate the operation of typical capacitance meters by approximating the non-linear circuit 13.1 with a linear one; then we compute the equivalent capacitance C of the circuit shown in fig. 13.2, whose evolution for $t \geq 0$ is described by:

$$\dot{I}(t) = -\frac{I(t)}{RC} + \frac{\dot{V}_G(t)}{R}, \quad I(0) = \bar{I},$$

where $V_G(t) = \widehat{V} + V_0 \sin(\omega t)$. The general solution to the Cauchy problem is:

$$I(t) = \bar{I} \exp\left(-\frac{t}{RC}\right) + \frac{V_0 C\omega}{1 + (RC\omega)^2} \left(\cos(\omega t) + RC\omega \sin(\omega t)\right). \tag{13.6}$$

The term $\bar{I} \exp\left(-\frac{t}{RC}\right)$ is neglected by supposing that the unsteady regime is over. We use a non-linear regression algorithm in order to estimate the equivalent resistance R and capacitance C by fitting the numerically computed $I(t)$ curve to eq. (13.6).

13.3 Constant barrier model

Numerical results have shown a strong dependence on the injection barrier considered at the metal-semiconductor interface.

In the following we will consider a general corrected model of the form:

$$\Phi'_B = \Phi_B + \vartheta\sqrt{\frac{qE_c}{4\pi\varepsilon_{sc}}}, \tag{13.7}$$

which implies $\Phi'_B \geq \Phi_B$, where ϑ is a constant multiplicative factor and $E_c = -\varphi'(-t_{sc})$ is the electric field at the bulk contact; for $\vartheta = 0$ the formula corresponds to the constant barrier model.

In this section we will show the results obtained by the constant barrier model (eq. (6.4)), which suggest that this model is no longer valid in the unsteady regime. In particular we analyze the results from the step response and the alternating regime simulations, by assessing in particular the trend of the accumulated charge (defined as $\int_{-t_{sc}}^{0} n(z,t)\mathrm{d}z$) as a function of time.

13.3.1 Step response

Figure 13.4 shows the simulated current when applying a step input signal. In particular the log-plot 13.5 shows a perfectly straight line, meaning that the exponential decay is a good approximation of the circuit behavior.

The first relevant result observed in fig. 13.6 is that the total accumulated charge is still too smaller than the value computed in the steady state simulation, whose order of magnitude is $10^{15}\left[\mathrm{m}^{-2}\right]$. Moreover, it does not reach a steady state even over the wide time interval considered, as well shown in fig. 13.7.

The numerical solution gives $\tau_{tr} = 0.159$ [ns], $\tau_n = 0.357$ [ns], $\bar{V}_{sc} = 1.2318$ [V] and $\bar{\mu} = 8.3464\cdot 10^{-06}\left[\mathrm{m}^2\mathrm{V}^{-1}\mathrm{s}^{-1}\right]$. We remark that in this case the theoretical time constant τ_{tr} is too small compared to τ_n; this is due to the fact that the value of $\bar{V}_{sc}$ is relatively large, thus hampering the flow of electrons. This behavior suggests that the model for the constant injection barrier at the bulk contact given by eq. (6.4) is too simplified and can not be adopted in unsteady simulations; in fact, a high barrier potential hampers the flow of electrons across the MIS channel so that the total conduction current is almost zero and the system acts as if a large resistance was connected in series to the device.

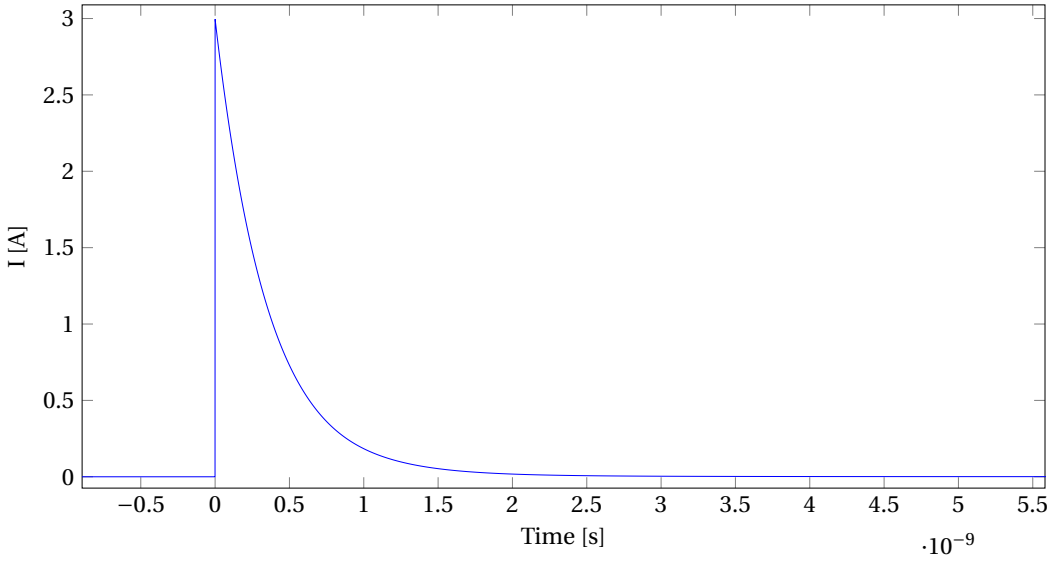

Figure 13.4: $\vartheta = 0$, step response: simulated current.

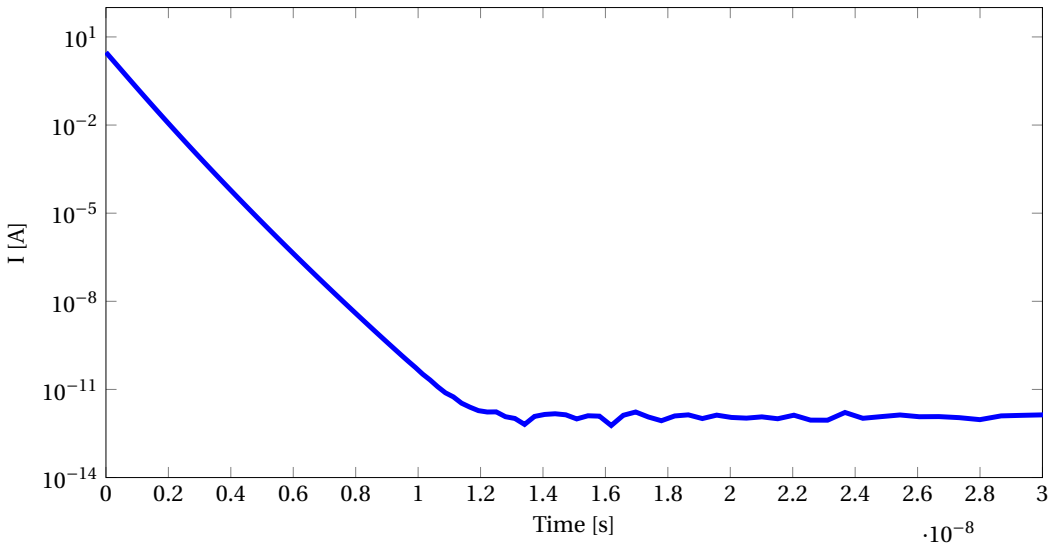

Figure 13.5: $\vartheta = 0$, step response: simulated current (log-plot).

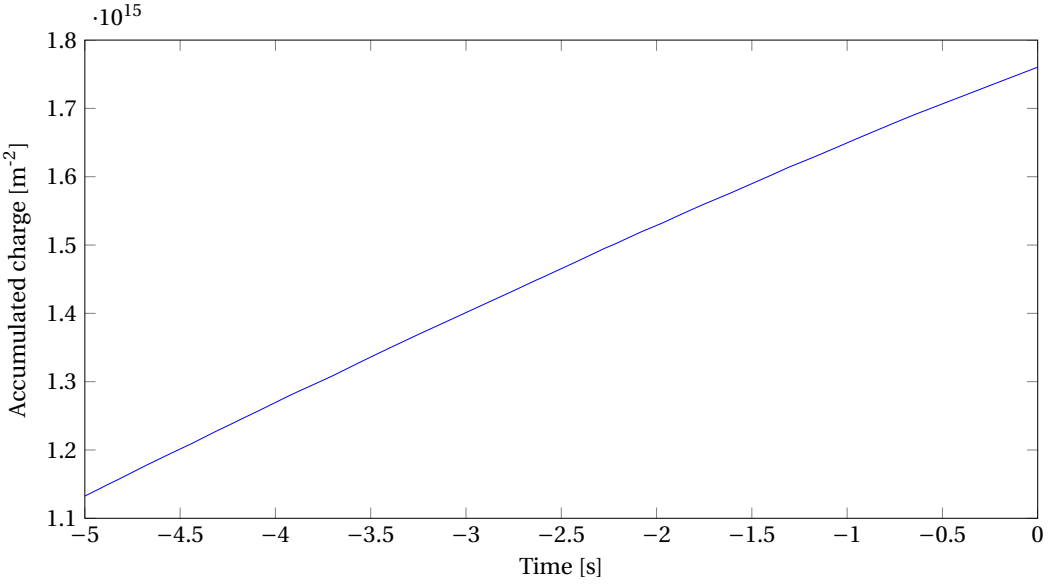

Figure 13.6: $\vartheta = 0$, step response: accumulated charge.

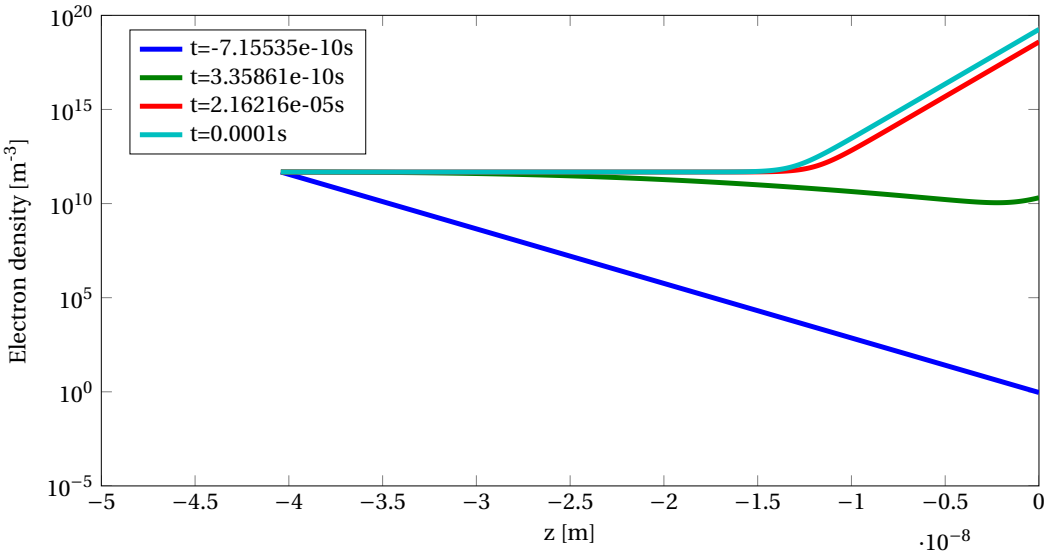

Figure 13.7: $\vartheta = 0$, step response: electron density at different time steps.

13.3.2 Alternating regime

Analogous conclusions can be drawn when simulating the $C-V$ curve in the accumulation regime: as the total accumulated charge does not reach a steady state within the 5 seconds preceding the application of the sinusoidal bias, the conduction current is still negligible with respect to the displacement one and the simulated $C-V$ curve (fig. 13.8) is completely flat (the device acts like a perfect insulator).

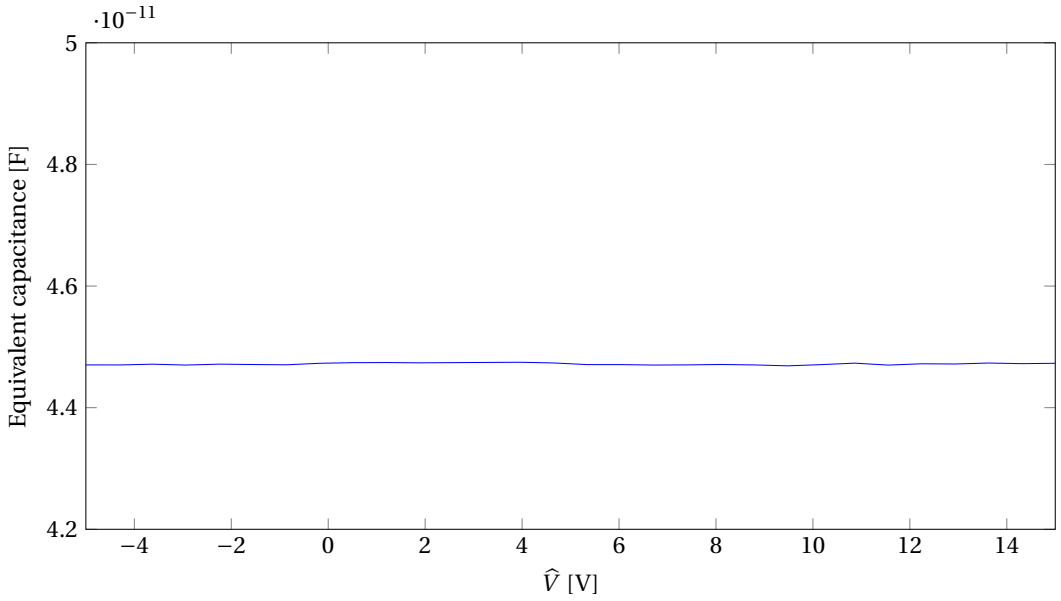

Figure 13.8: $\vartheta = 0$, alternating regime: equivalent capacitance.

13.4 Field-dependent barrier

This section is devoted to study in details how the results are influenced by the barrier model chosen; in particular we will compare the results obtained in both test cases (step response and alternating regime) by considering different correction factors ϑ.

13.4.1 Step response

Figure 13.9 shows the sensitivity of the step response simulated currents for $\vartheta = 0,\dots,5$. While the exponential decay constant τ_n does not seem to depend on the barrier correction, a more accurate log-plot (fig. 13.10) shows that the exponential decay does not depend on ϑ in a small interval around $t = 0$, while asymptotically equilibrium values are very different.

In fact, the larger is the correction (i.e. the lower is the barrier height in modulus) and the higher is the amount of conduction current allowed, which allows to gain several orders of magnitude as for the total current I but increasing difficulties in reaching an equilibrium value. In other words, a lower barrier allows electrons to flow across the semiconductor but this is not enough to ensure the reachability of an equilibrium state ($I = 0$) over a reasonable time. But we observe a reversed trend for $\vartheta = 5$, which corresponds to a sufficiently small barrier allowing a significant conduction current to be transported, though reaching an equilibrium state after less than 0.05 [ms]. This explains why choosing $\vartheta = 5$ as the amplification factor seems to be a reasonable heuristic model.

These results are confirmed by fig. 13.11, which shows that the theoretical transit time τ_{tr} increases with ϑ. More specifically, the numerical transit time τ_n does not depend on ϑ as it is equal to the classical RC circuit time constant, as shown by the following formula:

$$\tau = R_G C = 10 \frac{S}{\frac{t_{ins}}{\varepsilon_{ins}} + \frac{t_{sc}}{\varepsilon_{sc}}} \approx 0.356\,[\text{ns}]\,.$$

Therefore, when $\tau_{tr} < \tau_n$ the effects of the conduction current produced by electrons are negligible with respect to the displacement current, which is an unphysical behavior. In fact, the larger is the barrier height (in modulus) and the higher is $\bar{V}_{sc}$, thus hampering the flow of electrons across the semiconductor.

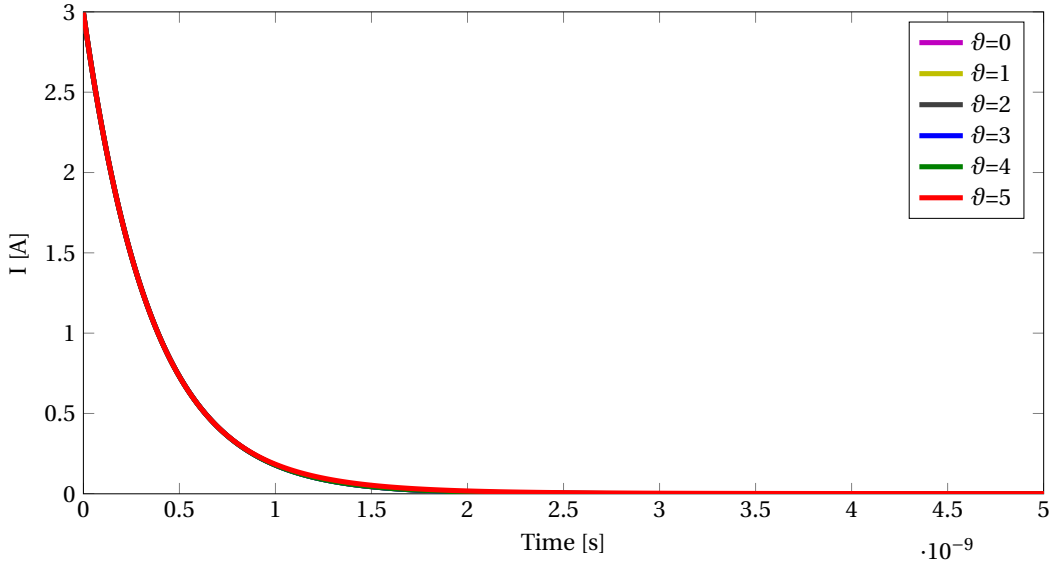

Figure 13.9: Step response: sensitivity of the current.

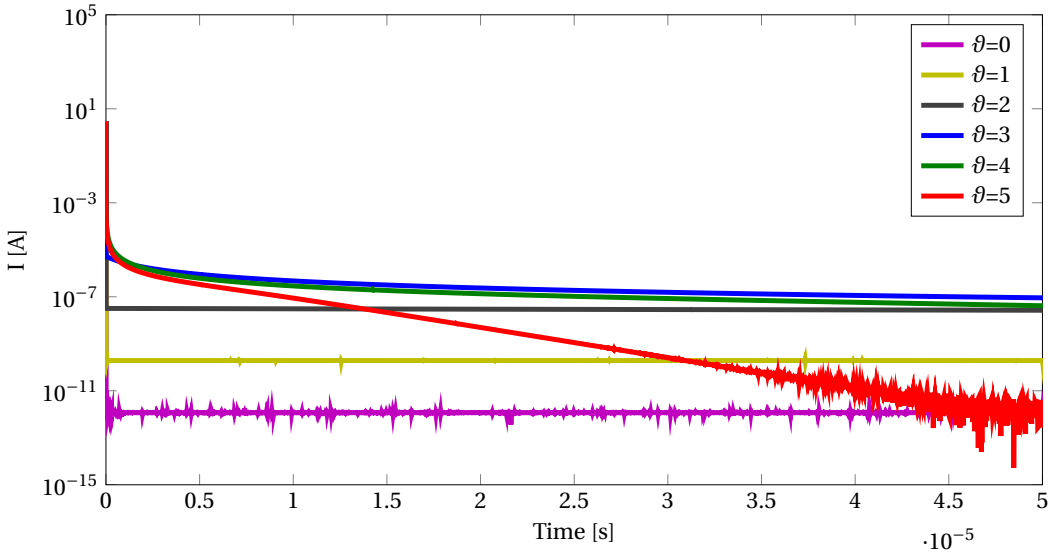

Figure 13.10: Step response: sensitivity of the current (log-plot).

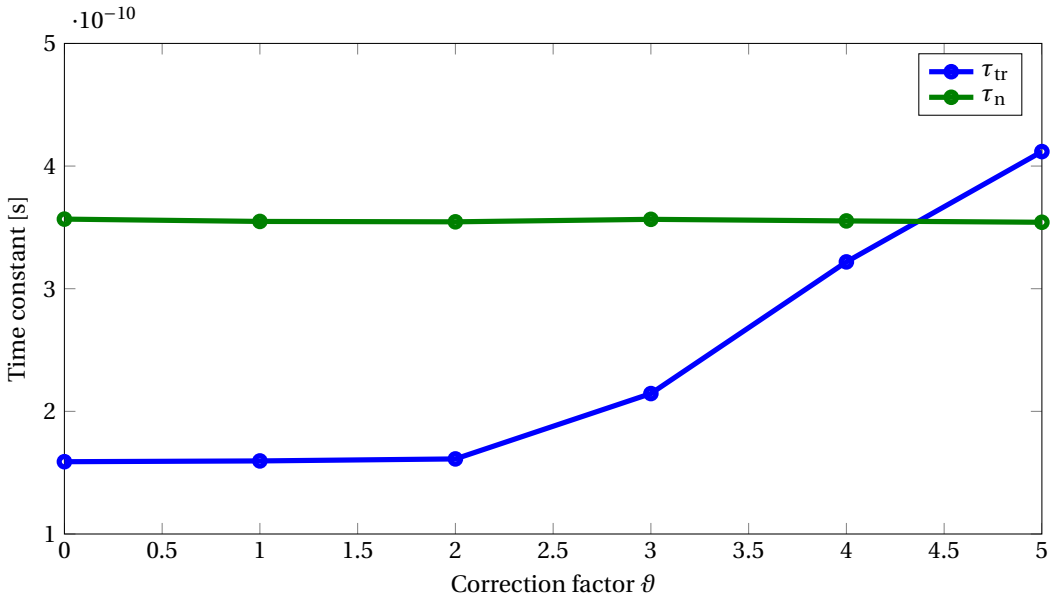

Figure 13.11: Sensitivity of time constants.

Figures 13.12 and 13.13 bring us to the same conclusions, which show that a lower barrier allows for a much larger electron density to be accumulated at the semiconductor-insulator interface $z = 0$ with respect to the constant barrier model (fig. 13.7); however the density for $\vartheta = 2$ does not reach an equilibrium value over the time interval considered, while $\vartheta = 5$ allows to reach an equilibrium value after ≈ 0.02 [ms].

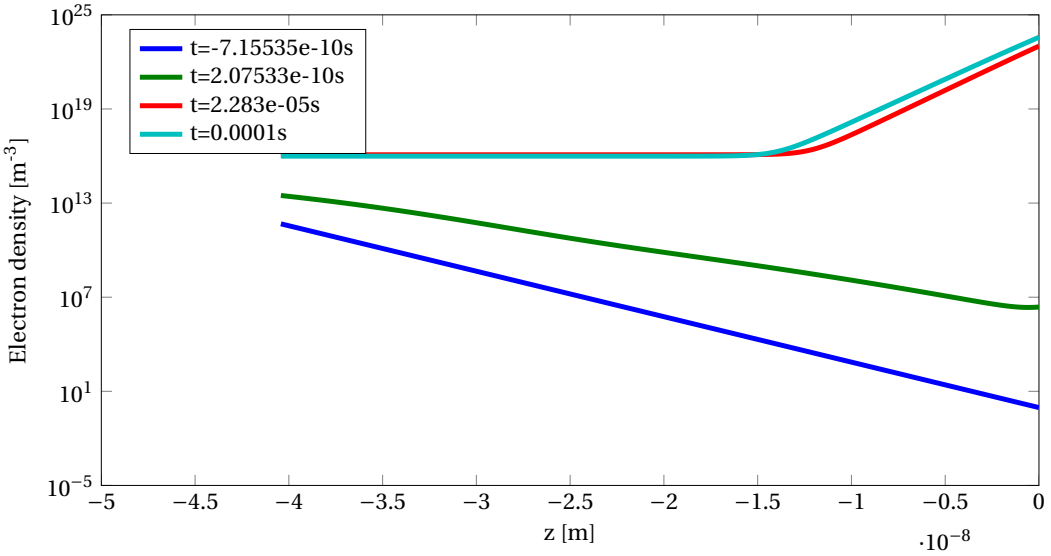

Figure 13.12: $\vartheta = 2$, step response: electron density at different time steps.

Finally, we evaluate how the total accumulated charge varies with the barrier correction ϑ: fig. 13.14 shows the same results discussed before, the lower the barrier and the higher is the total accumulated charge inside the device, thus allowing for the conduction current to flow; however, this is not enough to reach an equilibrium value over a reasonable time, which seems to be achieved only for $\vartheta = 5$.

The time-derivative of the accumulated charge, which is proportional to the total conduction current, is shown in fig. 13.15. This figure confirms that $\vartheta = 5$ is the best value we can choose to correct the barrier model, as it is sufficient to both let a significant conduction current flow and to bring the system at equilibrium over a physically meaningful time.

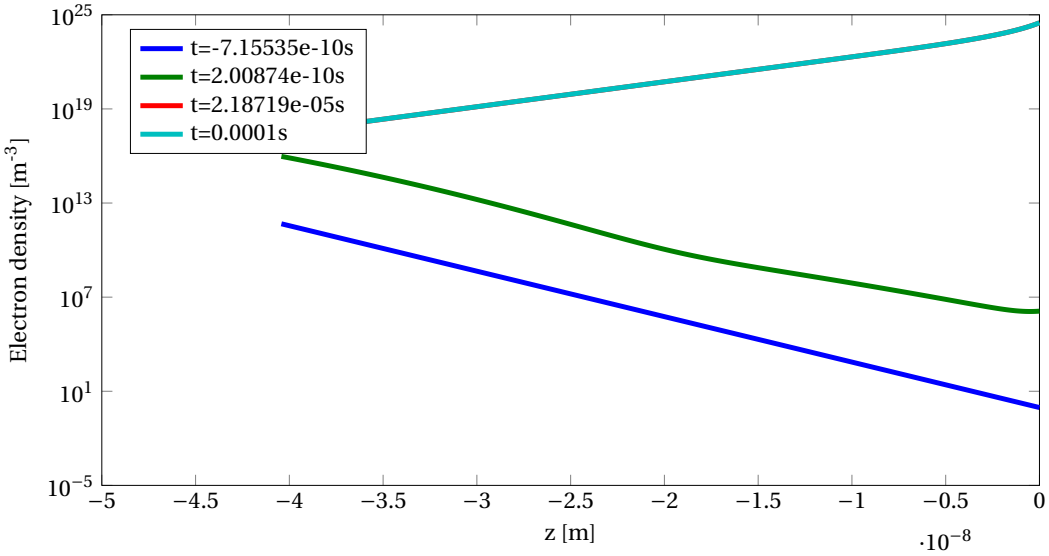

Figure 13.13: $\vartheta = 5$, step response: electron density at different time steps.

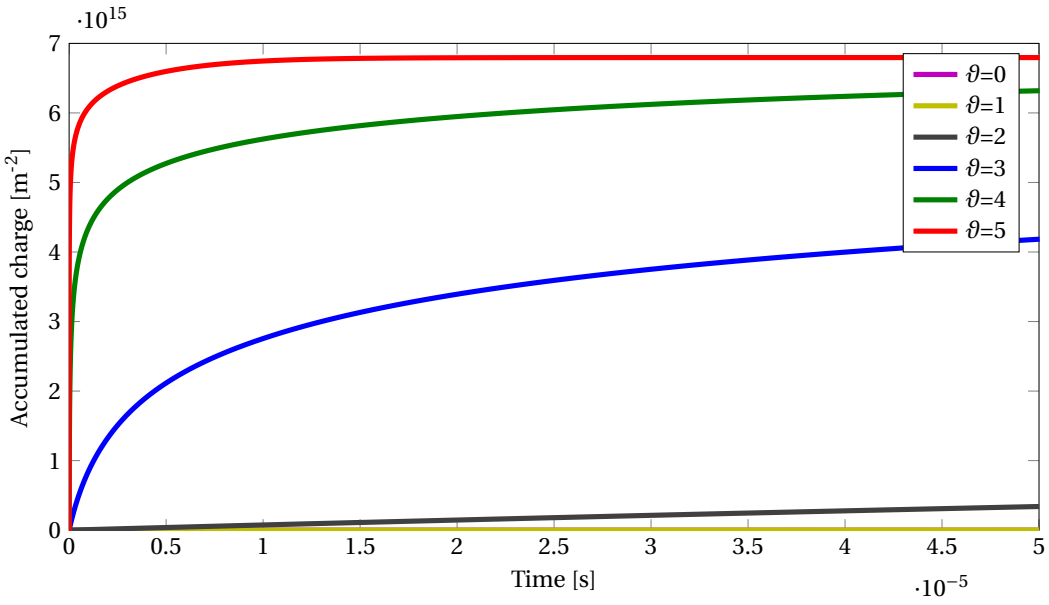

Figure 13.14: Step response: sensitivity of the accumulated charge.

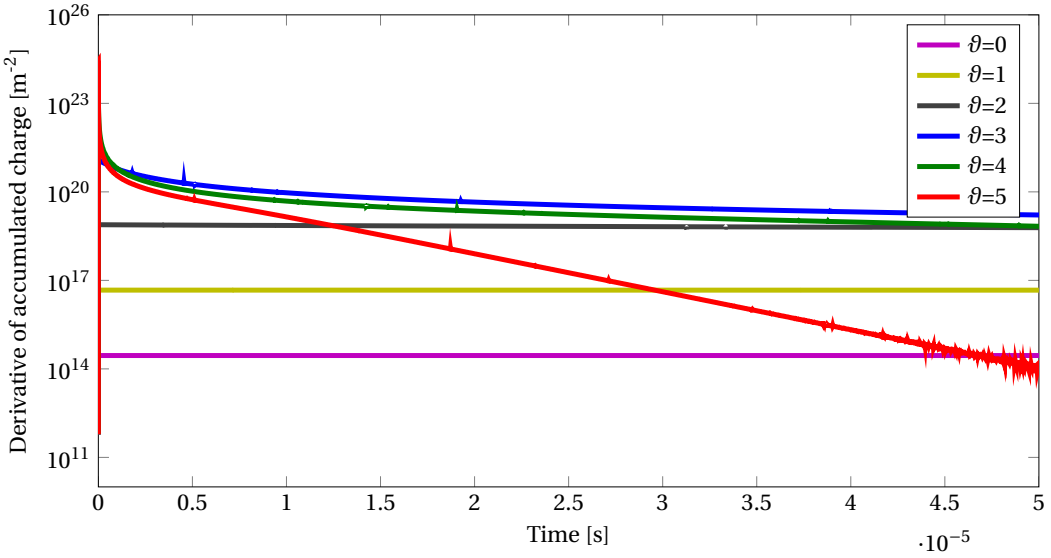

Figure 13.15: Step response: sensitivity of the derivative of the accumulated charge.

13.4.2 Alternating regime

Also in the alternating regime, as shown in fig. 13.16, we observe that for small correction factors, i.e. large barriers, the equivalent capacitance is completely flat as V_G varies, thus meaning that the device acts as an insulator in both depletion and accumulation regimes. Again, $\vartheta = 5$ is a very reasonable value, as it allows the $C-V$ curve to recover, thanks to the significant conduction current flowing, the same shape as the results computed in the quasi-static approximation and previously shown in sections 11.1 and 11.2.

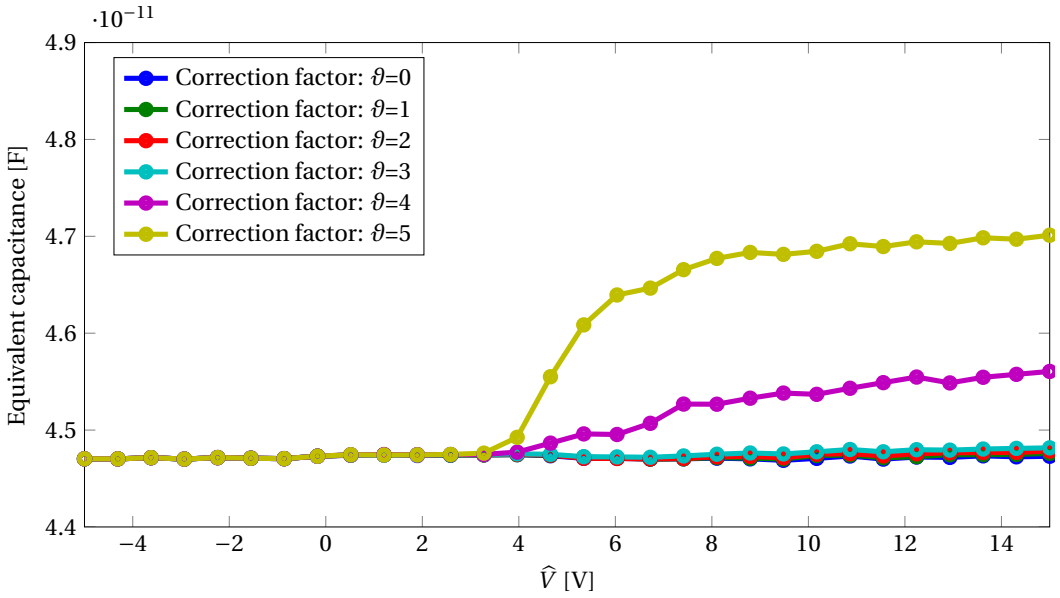

Figure 13.16: Step response: sensitivity of the equivalent capacitance.

13.5 Computing $C-F$ curve

The corrected model for the injection barrier described in section 13.3 has been exploited in order to simulate the *Capacitance-Frequency* ($C-F$) characteristic in the alternating regime. The applied voltage is the same as given by eq. (13.5), where $\widehat{V}$ = 20 [V] (accumulation) and the frequency ƒ varies from 0.2 [kHz] to 200 [kHz]; we remark that the electrical permittivity ε_{ins} of PMMA is a decreasing function of frequency [Mad+15]. Finally, the equivalent capacitance has been computed as described in section 13.2.

The results are shown in fig. 13.17. The comparison between the simulated $C-F$ curve and experimental measurements shows a very satisfactory match which slightly gets worse for very large frequencies, as the injection barrier would require a much more precise correction model and the non-linear fitting algorithm used provides less accurate results as the frequency grows.

In conclusion, the results shown in this chapter show how relevant is the role played by the the parameter Φ_B in unsteady simulations, as opposed to the quasi-static approximation (chapter 11) where the barrier, within a certain range, resulted in an almost rigid shift of the $C-V$ curve. Therefore an accurate modeling of the injection barrier certainly warrants further investigation, as the $C-V$ in the quasi-static regime is not sufficient to determine σ, t_{sc}, C_{sb} and Φ_B at the same time. Possibly, fitting the step response time constant to experimental measurements, which are currently not available, could be the way leading to assess the most accurate barrier model correction.

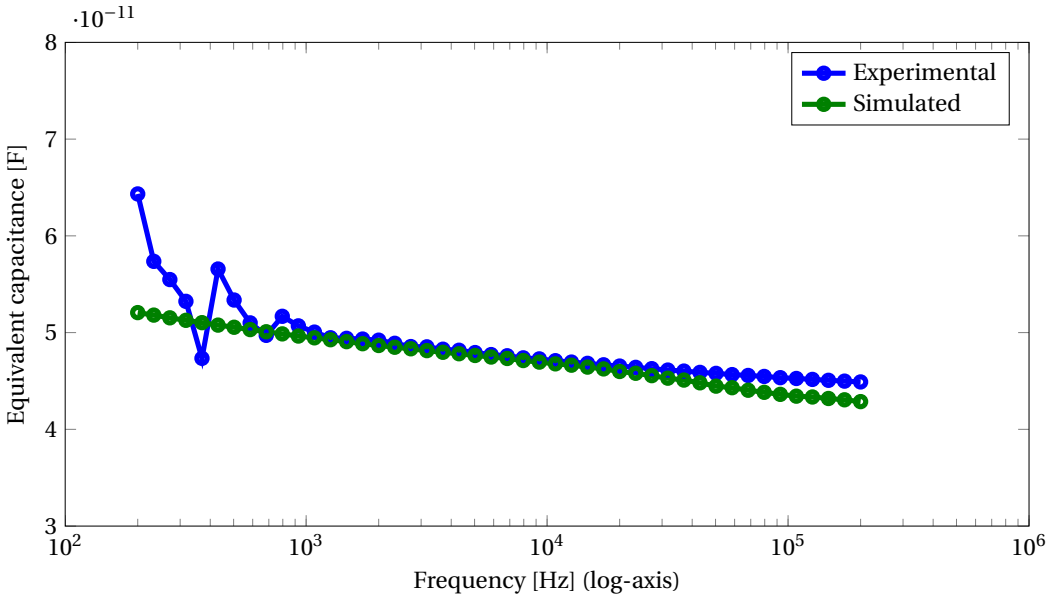

Figure 13.17: Capacitance-Frequency curve ($\widehat{V} = 20$).

14 Conclusions

This thesis project was carried out in collaboration with the Center for Nanoscience and Technology of the **Italian Institute of Technology (IIT)**, which provided experimental data used in this work.

The thesis addressed the main difficulties met in the mathematical modeling and simulation of organic semiconductor devices, which have motivated a continuous research because of their peculiarities such as easy and low cost fabrication of large area circuits, mechanical flexibility, high transparency and bio-compatibility.

We focused on mathematical models describing charge transport mechanisms in disordered organic materials, which are inherently different from those in well known crystalline inorganic systems. The classical DD equations have been adapted in order to provide an accurate mathematical description of the relevant phenomena involved, such as a strongly non-linear dependence of the mobility coefficient on the system variables, i.e. the electric field and the electron density, as provided by the state of the art model EGDM.

Our work was mainly based on [Mad+15], where the authors described an algorithm to assess the disorder parameter σ, which can not be directly measured but is crucial for the closure of the system, by fitting simulated results on experimental data. In particular we proposed significant modifications and generalizations to these algorithms in order to take into account unsteady regimes too. More specifically, we presented a generalized version of the classical resolution schemes used in the semiconductor devices simulation, i.e. the Newton's method and the Gummel fixed-point solution map, that include relevant physical models involved in organic semiconductors.

Chapter 13 is the most significant and original scientific contribution of this work: numerical results showed an unphysical behavior when simulating unsteady regimes; we ascertained that this was due to an incorrect modeling of a boundary condition representing charge injection phenomena which occur at metal-semiconductor interfaces and are strictly field-dependent.

Bibliography

[AM88] N. W. Ashcroft and N. D. Mermin. *Solid State Physics*. Holt, Rinehart and Winston, New York, 1988 (cit. on p. 25).

[And78] Philip W Anderson. "Local moments and localized states". In: *Reviews of Modern Physics* 50.2 (1978), p. 191 (cit. on p. 15).

[Ant02] HM Antia. *Numerical methods for scientists and engineers*. Vol. 1. Springer Science & Business Media, 2002 (cit. on p. 48).

[BCJC98] Randolph E Bank, WM Coughran Jr, and Lawrence C Cowsar. "The finite volume Scharfetter-Gummel method for steady convection diffusion equations". In: *Computing and Visualization in Science* 1.3 (1998), pp. 123–136 (cit. on p. 60).

[BP11] Pavel Bochev and Kara Peterson. *Control Volume Finite Element Method with Multidimensional Edge Element Scharfetter-Gummel upwinding. Part 2. Computational Study*. Tech. rep. Sandia National Laboratories, 2011 (cit. on p. 60).

[BS+14] Ariel J Ben-Sasson, Michael Greenman, Yohai Roichman, and Nir Tessler. "The Mechanism of Operation of Lateral and Vertical Organic Field Effect Transistors". In: *Israel Journal of Chemistry* 54.5-6 (2014), pp. 568–585 (cit. on pp. 3, 7).

[Boc11] Pavel Bochev. *Control Volume Finite Element Method with Multidimensional Edge Element Scharfetter-Gummel upwinding. Part 1. Formulation*. Tech. rep. Sandia National Laboratories, 2011 (cit. on p. 60).

[Bou+09a] M Bouhassoune, SLM Van Mensfoort, PA Bobbert, and Reinder Coehoorn. "Carrier-density and field-dependent charge-carrier mobility in organic semiconductors with correlated Gaussian disorder". In: *Organic Electronics* 10.3 (2009), pp. 437–445 (cit. on pp. 20, 31).

[Bou+09b] M Bouhassoune, SLM Van Mensfoort, PA Bobbert, and Reinder Coehoorn. "Carrier-density and field-dependent charge-carrier mobility in organic semiconductors with correlated Gaussian disorder". In: *Organic Electronics* 10.3 (2009), pp. 437–445 (cit. on p. 31).

[Bäs93] H Bässler. "Charge Transport in Disordered Organic Photoconductors, a Monte Carlo Simulation Study". In: *Physica status solidi* 175 (1993) (cit. on p. 20).

[CB12] Reinder Coehoorn and Peter A Bobbert. "Effects of Gaussian disorder on charge carrier transport and recombination in organic semiconductors". In: *Physica Status Solidi (a)* 209.12 (2012), pp. 2354–2377 (cit. on p. 14).

[Cho+14] W. Choi, T. Miyakai, T. Sakurai, A. Saeki, M. Yokoyama, and S. Seki. "Noncontact, non-destructive, quantitative probing of interfacial trap sites for charge carrier transport at semiconductor-insulator boundary". In: *Applied Physics Letters* 105.3, 033302 (July 22, 2014) (cit. on p. 27).

[Coe+05] Reinder Coehoorn, WF Pasveer, PA Bobbert, and MAJ Michels. "Charge-carrier concentration dependence of the hopping mobility in organic materials with Gaussian disorder". In: *Physical Review B* 72.15 (2005), p. 155206 (cit. on pp. 31, 32).

[ES99] A Einstein and M von Smoluchowski. "Untersuchungen über die Theorie der Brownschen Bewegung/Abhandlungen über die Brownsche Bewegung und verwandte Erscheinungen". In: *Harri Deutsch, Frankfurt* 3 (1999) (cit. on p. 26).

[FT09] J. A. Freire and C. Tonezer. "Density of states and energetic correlation in disordered molecular systems due to induced dipoles". In: *The Journal of Chemical Physics* 130.13, 134901 (Apr. 1, 2009) (cit. on p. 27).

[GS06] Riccardo Gusmeroli and Alessandro S Spinelli. "Accurate boundary integral calculation in semiconductor device simulation". In: *IEEE transactions on electron devices* 53.7 (2006), pp. 1730–1733 (cit. on pp. 37, 38).

[Gri05] David Jeffery Griffiths. *Introduction to quantum mechanics*. Pearson Education India, 2005 (cit. on p. 15).

[Gum64] HK Gummel. "A self-consistent iterative scheme for one-dimensional steady state transistor calculations'". In: *11* (1964), pp. 455–465 (cit. on p. 58).

[HMS00] Alan J Heeger, Alan G MacDiarmid, and Hideki Shirakawa. "The Nobel Prize in chemistry, 2000: conductive polymers". In: *Stockholm, Sweden: Royal Swedish Academy of Sciences* (2000) (cit. on pp. vii, ix).

[Hec11] Jeff Hecht. *Understanding lasers: an entry-level guide*. Vol. 21. John Wiley & Sons, 2011 (cit. on p. 14).

[Hug+00] Thomas JR Hughes, Gerald Engel, Luca Mazzei, and Mats G Larson. "The continuous Galerkin method is locally conservative". In: *Journal of Computational Physics* 163.2 (2000), pp. 467–488 (cit. on pp. 37, 38).

[Hul+04] I. N. Hulea, H. B. Brom, A. J. Houtepen, D. Vanmaekelbergh, J. J. Kelly, and E. A. Meulenkamp. "Wide Energy-Window View on the Density of States and Hole Mobility in Poly(*p*-Phenylene Vinylene)". In: *Physical Review Letters* 93.16, 166601 (Oct. 15, 2004) (cit. on p. 27).

[Jac99] John D Jackson. *Classical Electrodynamics*. 3rd ed. John Wiley & Sons, 1999 (cit. on p. 21).

[Jer96] JW Jerome. *Analysis of charge transport: a mathematical study of semiconductor devices*. 1996 (cit. on p. 14).

[KB15] Anna Köhler and Heinz Bässler. *Electronic Processes in Organic Semiconductors: An Introduction*. John Wiley & Sons, 2015 (cit. on p. 23).

[KKN14] Brijesh Kumar, Brajesh Kumar Kaushik, and YS Negi. "Perspectives and challenges for organic thin film transistors: materials, devices, processes and applications". In: *Journal of Materials Science: Materials in Electronics* 25.1 (2014), pp. 1–30 (cit. on p. 8).

[KU98] Arnold R Krommer and Christoph W Ueberhuber. *Computational integration*. Siam, 1998 (cit. on p. 47).

[Kax03] Efthimios Kaxiras. *Atomic and electronic structure of solids*. Cambridge University Press, 2003 (cit. on p. 14).

[Kit08] Charles Kittel. *Introduction to Solid State Physics*. Wiley, 2008 (cit. on p. 24).

[Kna+10] E Knapp, R Häusermann, HU Schwarzenbach, and B Ruhstaller. "Numerical simulation of charge transport in disordered organic semiconductor devices". In: *Journal of applied physics* 108.5 (2010), p. 054504 (cit. on p. 32).

[Kwo+12] S. Kwon, K.-R. Wee, J. W. Kim, C. Pac, and S. O. Kang. "Effects of intermolecular interaction on the energy distribution of valance electronic states of a carbazole-based material in amorphous thin films". In: *The Journal of Chemical Physics* 136.20, 204706 (2012-05-29) (cit. on p. 27).

[MA60] Allen Miller and Elihu Abrahams. "Impurity conduction at low concentrations". In: *Physical Review* 120.3 (1960), p. 745 (cit. on p. 19).

[MN15] Saumen Mandal and Yong-Young Noh. “Printed organic thin-film transistor-based integrated circuits”. In: *Semiconductor Science and Technology* 30.6 (2015), p. 064003 (cit. on p. 7).

[MR90] PA Markowich and CA Ringhofer. *C. Schmeiser, Semiconductor Equations*. 1990 (cit. on p. 14).

[MW94] JJH Miller and Song Wang. “An analysis of the Scharfetter-Gummel box method for the stationary semiconductor device equations”. In: *RAIRO-Modélisation mathématique et analyse numérique* 28.2 (1994), pp. 123–140 (cit. on p. 60).

[Mad+15] Francesco Maddalena, Carlo de Falco, Mario Caironi, and Dario Natali. “Assessing the width of Gaussian density of states in organic semiconductors”. In: *Organic Electronics* 17 (2015), pp. 304–318 (cit. on pp. vii, ix, 8, 22, 27, 36, 41, 42, 47–51, 66, 96, 99).

[Mad95] Otfried Madelung. *Introduction to solid-state theory*. Vol. 2. Springer Science & Business Media, 1995 (cit. on p. 25).

[Mar+09] N. G. Martinelli, M. Savini, L. Muccioli, Y. Olivier, F. Castet, C. Zannoni, D. Beljonne, and J. Cornil. “Modeling Polymer Dielectric/Pentacene Interfaces: On the Role of Electrostatic Energy Disorder on Charge Carrier Mobility”. In: *Advanced Functional Materials* 19.20 (2009), pp. 3254–3261 (cit. on p. 27).

[Mar86] Peter A Markowich. *The stationary semiconductor device equations*. Vol. 1. Springer Science & Business Media, 1986 (cit. on p. 22).

[Mei+06] KD Meisel, WF Pasveer, J Cottaar, C Tanase, R Coehoorn, PA Bobbert, PWM Blom, DM de Leeuw, and MAJ Michels. “Charge-carrier mobilities in disordered semiconducting polymers: effects of carrier density and electric field”. In: *Physica Status Solidi (c)* 3.2 (2006), pp. 267–270 (cit. on p. 19).

[OEA] *OE-A Roadmap for organic and printed electronics, 6th edition*. White Paper. Organic and Printed Electronics Association, 2015. URL: http://www.oe-a.org (cit. on p. 3).

[OHB12] J. O. Oelerich, D. Huemmer, and S. D. Baranovskii. “How to Find Out the Density of States in Disordered Organic Semiconductors”. In: *Physical Review Letters* 108.22, 226403 (May 29, 2012).

[PS99] Martin Pope and Charles E Swenberg. *Electronic processes in organic crystals and polymers*. Oxford University Press on Demand, 1999 (cit. on p. 16).

[Poe+13] C. Poelking, E. Cho, A. Malafeev, V. Ivanov, K. Kremer, C. Risko, J. Brédas, and D. Andrienko. "Characterization of Charge-Carrier Transport in Semicrystalline Polymers: Electronic Couplings, Site Energies, and Charge-Carrier Dynamics in PBTTT". In: *The Journal of Physical Chemistry C* 117.4 (2013), pp. 1633–1640 (cit. on p. 27).

[Pre07] William H Press. *Numerical recipes 3rd edition: The art of scientific computing*. Cambridge university press, 2007 (cit. on p. 47).

[RE11] M. Raja and B. Eccleston. "The significance of Debye length in disordered doped organic devices". In: *Journal of Applied Physics* 110.11, 114524 (Dec. 13, 2011) (cit. on p. 27).

[Riv+11] J. Rivnay, R. Noriega, J. E. Northrup, R. J. Kline, M. F. Toney, and A. Salleo. "Structural origin of gap states in semicrystalline polymers and the implications for charge transport". In: *Physical Review B* 83.12, 121306 (Mar. 16, 2011) (cit. on p. 27).

[SBS81] G Schönherr, H Bässler, and M Silver. "Dispersive hopping transport via sites having a Gaussian distribution of energies". In: *Philosophical Magazine B* 44.1 (1981), pp. 47–61 (cit. on p. 20).

[SG69] DL Scharfetter and H_K Gummel. "Large-signal analysis of a silicon read diode oscillator". In: *Electron Devices, IEEE Transactions on* 16.1 (1969), pp. 64–77 (cit. on p. 62).

[SM99] J Campbell Scott and George G Malliaras. "Charge injection and recombination at the metal–organic interface". In: *Chemical Physics Letters* 299.2 (1999), pp. 115–119 (cit. on p. 35).

[SS98] AS Sedra and KC Smith. *Microelectronic circuits*. Vol. 1. Oxford university press, 1998 (cit. on p. 48).

[Sel12] Siegfried Selberherr. *Analysis and simulation of semiconductor devices*. Springer Science & Business Media, 2012 (cit. on p. 23).

[Sha99] Hai Shao. "Numerical analysis of meshing and discretization for anisotropic convection-diffusion equations with applications". PhD thesis. Duke University, 1999 (cit. on p. 61).

[Sin+08] Th B Singh, NS Sariciftci, M Jaiswal, and R Menon. *Handbook of Organic Electronics and Photonics: Electronic materials and devices*. Ed. by HS Nalwa. Vol. 3. American Scientific Publishers, 2008. Chap. 4 (cit. on p. 53).

[Sir14] Henning Sirringhaus. "25th Anniversary Article: Organic Field-Effect Transistors: The Path Beyond Amorphous Silicon". In: *Advanced materials* 26.9 (2014), pp. 1319–1335 (cit. on pp. 7, 9).

[TM11] A. K. Tripathi and Y. N. Mohapatra. “Correlation of photocurrent and electroabsorption spectra and their temperature dependence for conjugated light emitting polymers: The origin of the corresponding density of states”. In: *Physical Review B* 84.20, 205213 (Nov. 18, 2011) (cit. on p. 27).

[Tun14] Raymond T Tung. “The physics and chemistry of the Schottky barrier height”. In: *Applied Physics Reviews* 1.1 (2014), p. 011304 (cit. on p. 35).

[VDH+09] JJM Van Der Holst, MA Uijttewaal, B Ramachandhran, Reinder Coehoorn, PA Bobbert, GA De Wijs, and RA De Groot. “Modeling and analysis of the three-dimensional current density in sandwich-type single-carrier devices of disordered organic semiconductors”. In: *Physical Review B* 79.8 (2009), p. 085203 (cit. on p. 36).

[VMC08] SLM Van Mensfoort and Reinder Coehoorn. “Effect of Gaussian disorder on the voltage dependence of the current density in sandwich-type devices based on organic semiconductors”. In: *Physical Review B* 78.8 (2008), p. 085207 (cit. on pp. 31, 32).

[VW09] N. Vukmirović and L.-W. Wang. “Charge Carrier Motion in Disordered Conjugated Polymers: A Multiscale Ab Initio Study”. In: *Nano Letters* 9.12 (Nov. 13, 2009), pp. 3996–4000 (cit. on p. 27).

[VW11] N. Vukmirović and L.-W. Wang. “Density of States and Wave Function Localization in Disordered Conjugated Polymers: A Large Scale Computational Study”. In: *The Journal of Physical Chemistry B* 115.8 (Feb. 3, 2011), pp. 1792–1797 (cit. on p. 27).

[Vri+13] R. J. de Vries, A. Badinski, R. A. J. Janssen, and R. Coehoorn. “Extraction of the materials parameters that determine the mobility in disordered organic semiconductors from the current-voltage characteristics: Accuracy and limitations”. In: *Journal of Applied Physics* 113.11, 114505 (Mar. 19, 2013) (cit. on p. 27).

[Wei+06] DS Weiss, M Abkowitz, S Kasap, and P Capper. *Handbook of Electronic and Photonic Materials*. Springer, 2006. Chap. 9 (cit. on pp. 15, 16, 27).

[Yan+09] He Yan, Zhihua Chen, Yan Zheng, Christopher Newman, Jordan R Quinn, Florian Dötz, Marcel Kastler, and Antonio Facchetti. “A high-mobility electron-transporting polymer for printed transistors”. In: *Nature* 457.7230 (2009), pp. 679–686 (cit. on p. 65).

[Zho+14] Ke Zhou, Huanli Dong, Hao-li Zhang, and Wenping Hu. “High performance n-type and ambipolar small organic semiconductors for organic thin film transistors”. In: *Physical Chemistry Chemical Physics* 16.41 (2014), pp. 22448–22457 (cit. on p. 4).